

**STABILITY, CONTROL AND ACOUSTIC MANIPULATION OF
MAGNETICALLY ACTUATED HELICAL SWIMMERS**

by
HAKAN OSMAN ÇALDAĞ

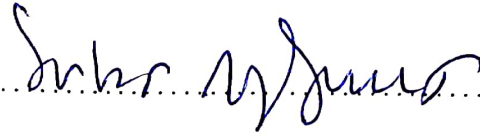
Submitted to the Graduate School of Engineering and Natural Sciences
in partial fulfilment of
the requirements for the degree of Doctor of Philosophy

Sabanci University
August 2020

STABILITY, CONTROL AND ACOUSTIC MANIPULATION OF
MAGNETICALLY ACTUATED HELICAL SWIMMERS

Approved by:

Prof. Serhat Yeşilyurt
(Dissertation Supervisor)



Assoc. Prof. Ayhan Bozkurt



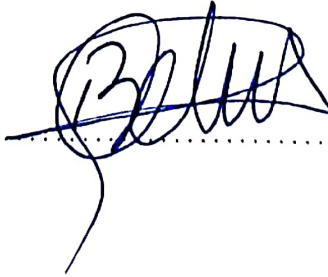
Assoc. Prof. Meltem Elitaş



Asst. Prof. Ahmet Fatih Tabak



Assoc. Prof. Barbaros Çetin



Date of Approval: August 19, 2020

HAKAN OSMAN ALDAĐ 2020  

All Rights Reserved

ABSTRACT

STABILITY, CONTROL AND ACOUSTIC MANIPULATION OF MAGNETICALLY ACTUATED HELICAL SWIMMERS

HAKAN OSMAN ÇALDAĞ

MECHATRONICS ENGINEERING Ph.D DISSERTATION, AUGUST 2020

Dissertation Supervisor: Prof. Serhat Yeşilyurt

Keywords: microrobotics, low Reynolds number swimming, acoustics, helical swimmers

Microswimmers are prospective agents for manipulation in fluid environments at low scales. Potential use cases include targeted drug delivery and microsurgery. Magnetized helical microswimmers are used extensively in the literature as they can be actuated externally with a rotating magnetic field. This dissertation reports on the modes of instability of magnetized helical swimmers and proposes several solutions to enable controlled navigation, which is crucial considering the potential biomedical applications. The modes of instability are characterized with a kinematic model that relies on snap-shot solutions of Stokes equations. Pusher-mode instability occurs in confined environments, resulting in helical trajectories. A novel, magnetic steering control algorithm is proposed to suppress the oscillatory trajectories. Contrary to the state-of-the-art, this method doesn't require any orientation feedback and performs equally well. On top of magnetic steering, acoustic fields are demonstrated to be beneficial in reducing wobbling. The bio-compatible nature of acoustic fields makes it an ideal complement to the magnetic field. A novel and efficient computational model for the calculation of the acoustic radiation force on helices (which is costly otherwise) is presented where the helix is approximated as a chain of spheres for which simple analytical formulae exist. The sum of forces on spheres is very close to the force acting on the helix. The approach is utilized in simulating the trajectories of helical swimmers under acoustic and magnetic fields with promising results. In experiments, magnetic swimmers made from thin wires are placed under magnetic and acoustic fields. Viscosity reduces acoustic propulsion significantly.

ÖZET

MANYETİK ALANLA YÜZÜDÜRÜLEN SARMAL YÜZÜCÜLERİN KARARLILIĞI, KONTROLÜ VE AKUSTİK MANİPÜLASYONU

HAKAN OSMAN ÇALDAĞ

MEKATRONİK MÜHENDİSLİĞİ DOKTORA TEZİ, AĞUSTOS 2020

Tez Danışmanı: Prof. Dr. Serhat Yeşilyurt

Anahtar Kelimeler: mikrorobotik, düşük Reynolds numarasında yüzme, akustik, sarmal yüzücüler

Mikroyüzücüler küçük ölçeklerde ve sıvı ortamlarda manipülasyon için kullanılacak elemanlardır. Hedef dokuya ilaç teslimi ve mikroşirüji gibi potansiyel kullanım alanları mevcuttur. Manyetik sarmal mikroyüzücüler dönen manyetik alanla dışarıdan yözdürülebildiği için sıklıkla kullanılmaktadır. Bu tezde manyetik sarmal yüzücülerin dengesizlik halleri raporlanmış ve kontrollü yözdürme için (biyomedikal uygulamalar bağlamında önemlidir) çeşitli çözüm önerileri sunulmuştur. Dengesizlik halleri anlık Stokes çözümlerinin kullanıldığı kinematik bir modelle incelenmiştir. Kanal içinde sarmal yörüngeye sebep olan itici-modu kararsızlığı olmaktadır. Bu salınımları önlemek için yeni bir manyetik yönlendirmeli kontrol algoritması sunulmuştur. Literatürdeki çalışmaların aksine, bu yöntemde eğitim bilgisine ihtiyaç duyulmamakta ve buna rağmen kıyaslanabilir sonuçlar elde edilmektedir. Manyetik yönlendirmenin üzerine, akustik alanın da yalpalamayı azaltmakta faydalı olduğu gözlemlenmiştir. Akustik dalgaların biyoyumumluluğu bu yöntemi manyetik alan üzerine ideal bir tamamlayıcı kılmaktadır. Helisler üzerine etkiyen akustik radyasyon kuvvetinin hesaplanmasında helisin bir küre zinciri olarak temsil edildiği (küreler için basit formüller mevcuttur) yeni ve verimli bir hesaplama yöntemi (diğer yöntemlerle verimsizdir) sunulmaktadır. Kürelere etkiyen toplam kuvvet, helise etkiyen kuvvete çok yakındır. Bu yaklaşım sarmal yüzücülerin akustik ve manyetik alan altındaki yörüngelerini hesaplamada kullanılmış ve umut vaat eden sonuçlar elde edilmiştir. Deneylerde ince telden yapılmış manyetik yüzücüler akustik ve manyetik alan altına yerleştirilmiştir. Viskozite akustik itkiyi büyük ölçüde azaltmaktadır.

ACKNOWLEDGEMENTS

I thank deeply my thesis advisor, Prof. Serhat Yeşilyurt for all his help during the whole 6 years, including not only my PhD education but also my MSc. studies. He has always made himself available to help and discuss all aspects of my research. He made me feel that we are working together, which gave me a different and better sense of responsibility than the usual professor-student relationship one may assume. His motivation, even during the tough times due to Covid-19 pandemic, is what helped me complete this dissertation.

I would also like to thank Assoc. Prof. Ayhan Bozkurt and Assoc. Prof. Meltem Elitaş, my thesis monitoring committee members, for their help, suggestions and time they spent during my research period. I am thankful to external members of my jury, Assoc. Prof. Barbaros Çetin and Asst. Prof. Ahmet Fatih Tabak for their help and efforts. I am also thankful to previous members of our research group, Dr. Ebru Demir, Dr. Alperen Acemoğlu, Asst. Prof. Fatma Zeynep Temel and Asst. Prof. Ahmet Fatih Tabak for their suggestions during my research. I also want to thank our current team members Milad Shojaeian and Fatemeh Malekabadi. I also thank İlker Sevgen, Yavuz Toksöz, Barış Tümer, Onur Serbest, Semih Pehlivan, Bülent Köroğlu and Dr. Cenk Yanık for their support on technical issues. I wish everyone the best for their future.

I would not be able to continue my research without firm support from my family. I am grateful to my parents, sisters and brothers-in-law. I specifically want to thank my nephew Kivanç and my niece Defne for putting a smile on my face each time I see them. I hope to show this page to them when they grow up so they can read it themselves.

I am also thankful to my fiancée Zeynep, with whom I met at the most challenging times during my PhD. I thank her for listening to my hurdles patiently and brightening up my days which helped me a lot in completing this dissertation. I am also thankful to my friends Dr. Ali Keçebaş, Osman Saygıner, Dr. Murat Eskin, Dr. Abdullah Kamadan and also many others that helped me pass through and enjoy it while doing so.

I acknowledge TUBITAK support under their BİDEB-2211 program during my whole PhD period. TUBITAK also supported several parts of the work under the grant no 116E186.

TABLE OF CONTENTS

LIST OF TABLES	ix
LIST OF FIGURES	x
LIST OF ABBREVIATIONS	xiv
1. INTRODUCTION	1
1.1. Background	2
1.1.1. Swimming with a Helical Tail	2
1.1.2. Modes of Instability	4
1.1.3. Controlled Navigation of Helical Microswimmers	6
1.1.4. Acoustic Radiation Force.....	7
1.1.5. Acoustically Actuated Swimmers	9
1.2. Novelties of the Thesis	12
2. Stability of Magnetically Actuated Helical Swimmers	15
2.1. The Kinematic Model.....	15
2.2. Verification of the CFD Model.....	21
2.3. Pusher-mode Instability	23
3. Magnetic Manipulation of Magnetized Helical Swimmers	30
3.1. Swimmer Kinematics and Control Law	30
3.2. Resistive Force Theory-Based Modelling of Helical Swimming	36
3.3. Experiment Setup.....	40
3.4. Verification of Steering Control Algorithm	41
4. Modelling Acoustic Radiation Force on Helices	46
4.1. Acoustic Radiation Force	46
4.2. Analytical Modeling and Chain-of-Spheres Approach	50
4.3. Finite Element Modelling	53
4.4. Chain-of-Spheres Simulations: Verification	56

5. Acoustic Manipulation of Magnetically Actuated Helices	63
5.1. Modelling	63
5.2. Acousto-Magnetic Propulsion	64
5.3. Trajectories of Magnetized Helical Swimmers Under Acoustic Fields..	67
5.4. Acousto-magnetic Experiment Setup	68
5.4.1. Visual Interface and Image Processing	73
5.5. Acoustic Radiation Experiments.....	76
5.5.1. Experiments With the Unfocused Transducer	76
5.5.2. Experiments with the Focused Transducer.....	80
6. Conclusion	82
6.1. Future Work	84
BIBLIOGRAPHY.....	88
APPENDIX A	93

LIST OF TABLES

Table 2.1. Convergence test for the CFD model. The line in bold represents the meshing density used for the simulations.	20
Table 2.2. Values of the geometric parameters tested. The values in bold typeface refer to base values, which are also used for the validation studies.....	21
Table 2.3. The sensitivity of the results to variations in D_{head} and d for swimmer L4 with $D_{ch} = 1.6$ (pusher-mode). Values in bold correspond to the simulation whose results are shown at Fig. 2.2 (a)-(d)...	23
Table 2.4. θ_{ax} values for several different swimmers and swimming conditions.	26
Table 3.1. Geometric parameters of the 3D-printed swimmer used in the experiments.	41
Table 4.1. Comparison of 3-dimensional FEM model results with those from the literature for spheres made of several different materials.	55
Table 4.2. Properties of the materials used in the simulations.....	55
Table 4.3. Geometric parameters of the helix used for the convergence studies of the 3D FEM model for simulating the acoustic radiation force on helices.	56
Table 4.4. Geometric parameters of the helix used in the validation studies.	57
Table 4.5. Base geometric dimensions of the swimmer used for the trajectory simulations.	60
Table 4.6. Rotation-averaged torques acting on the tilted helical swimmer.	62
Table 5.1. The geometric parameters of the swimmers in Fig. 5.5	70
Table 5.2. Operation parameters of the transducers.	72

LIST OF FIGURES

<p>Figure 2.1. Geometric parameters of the swimmer and the channel, representations of rotating magnetic field \mathbf{B}, gravity vector \mathbf{g} and channel inlet flow with a parabolic profile and average velocity, v_f. Forward (head direction, pusher-mode) and backward (tail direction, puller-mode) motion of the swimmer.</p>	16
<p>Figure 2.2. Comparison of simulation and experimental results for the pusher-mode ((a)-(d)) and the puller-mode ((e)-(h)) trajectories. (a) and (e) show the trajectories on the radial plane, (b) and (f) show average β with their variations, (c) and (g) show average θ_{ax} with their variations and (d) and (h) show average \hat{U}_{sw} with their variations. (i) shows the swimmer used in experiments and (j) is the idealization of this swimmer used in the simulations.</p>	23
<p>Figure 2.3. Comparisons of the trajectories for the pusher and puller-mode swimming with the same initial conditions. (a) and (b) show the linear velocities in \mathbf{y}- and \mathbf{z}- directions, respectively and (c) and (d) show the angular velocities in these directions. (e) shows the change of β in both modes. The insets in (a)-(e) show the initial part of the simulations to demonstrate the breakdown of the symmetry. (f) shows the radial trajectories of the pusher and puller-mode swimmers where the pusher-mode trajectory is mirrored in the \mathbf{y}- direction to better show the separation of the trajectories. (g) shows a zoomed-in version of the first few instances of (f).</p>	25
<p>Figure 2.4. The effects of the Ma_c on the stable time-averaged trajectory parameters for (a)-(d) the pusher-mode and (e)-(g) the puller mode. .</p>	27

Figure 2.5. Wobbling of a puller at high Ma_c inside a channel with $D_{head}/D_{ch} = 0.26$. a) Positions of the head and tail tip in the experiment from Caldag et al. (2017), b) positions of the head and tail tip in simulations for $Ma_c = 0.74$ and c) for $Ma_c = 1.77$. θ_{ax} values at (a)-(c) are the averages for given parts of the trajectories. d) Change of β in extended simulations for $Ma_c = 0.74$ and $Ma_c = 1.77$, showing that the swimmer converges towards a stable trajectory but at a longer time compared to the experiments. Note that the trajectories at b) and c) are representative of a few rotations of the swimmer and do not show the complete trajectories at (d).....	28
Figure 3.1. (a) The geometric setup, showing the channel, the swimmer, rotating magnetic field, field normal and propulsion direction. (b) Steering of the swimmer through tilting the normal of the magnetic field. (c) Representation of angles θ_{xy} and θ_{xz}	31
Figure 3.2. Block diagram of the swimmer kinematics and control.....	35
Figure 3.3. Experimental setup showing the Helmholtz coils, digital camera and computer. An image captured from experiment recordings; coordinate axes and angles θ_{xy} and θ_{xz} are shown at the right-hand side.....	40
Figure 3.4. Swimmer trajectories in the numerical model with and without control. (a) shows the 3D trajectories while (b) shows y vs. x and (c) shows z vs. x	42
Figure 3.5. (a) 3D swimmer trajectories in the pusher-mode from the kinematic model with and without control. (b) \mathbf{y} - coordinates and (c) \mathbf{z} - coordinates of the swimmer for $\mathbf{p}_{ref} = [x \ 0 \ 0.2\sin(1.5t)]'$	43
Figure 3.6. Non-dimensional trajectory radii with and without control in the channels where (a) $D_{ch} = 3$ mm, (b) $D_{ch} = 5.6$ mm. (c) shows the performance of different control strategies under $D_{ch} = 3$ mm. Note that $K_{i,\{y,z\}}$ for PID control are the same as in PI control.	44
Figure 4.1. (a) Placement of a single turn helix with respect to global coordinates. (b) Close-up view of the helix and its geometric parameters. (c) Representation of the helix as a chain of spheres. The spheres are placed along the centerline of the helix, shown with blue dashes.	50
Figure 4.2. Geometric setup of the model in Glynne-Jones et al. (2013). ..	54
Figure 4.3. Mesh convergence plot of the FEM model.....	56

Figure 4.4. Validation of the chain-of-spheres approach with respect to different geometric parameters. (a) to (h) show the results for nickel, (i) to (p) show the results for nylon. (a) and (b) ((i) and (j) for nylon) show the radiation forces and relative error with respect to N_h , (c) and (d) ((k) and (l) for nylon) show the forces and relative errors with respect to d , (e) and (f) ((m) and (n) for nylon) show the forces and relative errors with respect to D and (g) and (h) ((o) and (p)) show the forces and relative errors with respect to λ_h	58
Figure 4.5. The distribution of scattered pressure field for helices with (a) $\lambda_h = 50 \mu\text{m}$ and $N_h = 3$ and (b) $\lambda_h = 150 \mu\text{m}$ and $N_h = 1$. Other parameters are as given in Table 4.4.	59
Figure 4.6. (a) Convergence of F_{st}^{rad} with respect to N_{sph} . (b) Convergence of radiation torques with respect to N_{sph} . Dashed lines indicate the values obtained from the FEM simulation.	61
Figure 4.7. (a) Components of τ_x in FEM simulations and τ_x evaluated from the chain-of-spheres approach during a complete rotation of the swimmer. (b) Components of τ_y in FEM simulations and τ_y evaluated from the chain-of-spheres approach during a complete rotation of the swimmer.	62
Figure 5.1. Change of the velocity gain, $W_{ac}/W_{no,ac}$, due to the acoustic field with respect to (a) p_a , (b) f_a , (c) λ_h/λ_a and (d) d	65
Figure 5.2. Change in W_{sw} with respect to μ	66
Figure 5.3. Trajectory parameters of magnetized helical swimmers under travelling acoustic field. (a)-(b) show the parameters for different Ma , (c)-(d) show for different λ_h , (e)-(f) show for different d and (g)-(h) show for different D . (a), (c), (e) and (g) show trajectory radii r_t . (b), (d), (f) and (h) show the wobbling angle θ_{ax} . The acoustic field is turned on at $t = 6$ s and magnetic swimming is initiated at $t = 0$ s.	68
Figure 5.4. (a) Initial ($\mathbf{p} = [0 \ 0 \ 0]'$) and the final positions of helices with different wavelengths in 3-dimensional space under standing acoustic field. (b) Initial ($t = 0$ s) and final ($t = 0.1$ s) \mathbf{z} -coordinates of the same conditions. (c) Initial (0,0) and final radial coordinates of the same swimmers on x-y plane.	69
Figure 5.5. Two of the swimmers used in the experiments. Refer to Table 5.1 for geometric dimensions.	70
Figure 5.6. (a) A capture from the experiment setup. (b) Schematic of the setup.	71

Figure 5.7. A capture from the experiment recordings. Camera directly captures (a) x-y plane image while a mirror placed with a 45-degree inclination captures (b) x-z plane image. Gravity is acting in -x direction.	72
Figure 5.8. Graphical user interface developed in Matlab. The coils, the camera and the signal generator are all controlled from this interface. The caption was taken during INITIALIZE mode in which the swimmer is moved to reference position automatically. Refer to Fig. 5.7 for an example image from experiment recordings.	74
Figure 5.9. A caption from image processing. (a) The original image. (b) Image after edge detection and smoothing operations are applied. (c) Detected swimmer region (red rectangle) and its centroid (red circle).	75
Figure 5.10. Swimmer trajectory without acoustic field and at a fixed $f_m = 10$ Hz at different times. (a) shows the axial position, (b) shows the velocity.	77
Figure 5.11. The change in u with respect to μ without acoustic field. Results are obtained from the FEM model in Chapter 2 with the gravity acting against the propulsion direction as in experiment setup (Corresponding to +x direction in Fig. 2.1 and -x direction in Fig. 5.7). .	78
Figure 5.12. Swimmer (a) position and (b) velocity at $f_m = 18$ Hz under different modes of acoustic actuation.	79
Figure 5.13. Comparison of experiment results in Fig. 5.12 with the simulation results obtained with the model in Section 5.1. The error bars represent the variation in the results in Fig. 5.12.	80
Figure 5.14. u of the swimmer with respect to axial position at (a) 50 V and (b) 200 V.	81
Figure 5.15. Swimmer velocity during falldown at $f_m = 3$ Hz with and without acoustic excitation. The transducer is the focused one and operates at its maximum response frequency, $f_a = 10$ MHz.	81

LIST OF ABBREVIATIONS

CFD Computational fluid dynamics	ix, 12, 19, 20, 21
FEM Finite element method ..	ix, xi, xii, xiii, 8, 46, 51, 55, 56, 57, 58, 59, 60, 61, 62, 64, 77, 78, 82, 83
FVM Finite volume method	8
PML Perfectly matched layer	8, 54

LIST OF SYMBOLS

A	Complex amplitude of the incident velocity potential
A_h	Helix amplitude
B_0	Magnetic field strength
D_{ch}	Channel diameter
D_c	Duty cycle
D_{head}	Diameter of the swimmer head
E	Acoustic energy density
$F_{st,y}^{rad}$	Radiation force in \mathbf{y} - direction, standing acoustic wave
I	Current passing through the magnetic coils
K_y	Gain for e_y in error dynamics equation
K_z	Gain for e_z in error dynamics equation
$K_{d,y}$	Derivative gain, \mathbf{y} - component
$K_{d,z}$	Derivative gain, \mathbf{z} - component
$K_{i,y}$	Integral gain, \mathbf{y} - component
$K_{i,z}$	Integral gain, \mathbf{z} - component
L	Helix length
L_{head}	Length of the swimmer head
N	Number of cycles in burst mode actuation of transducers
N_c	Number of windings of the Helmholtz coils
N_h	Number of rotations of the helix

N_{sph}	Number of spheres placed in the chain of spheres approach
P_n	Legendre polynomial
P_{tot}	Total electrical power consumption
R_{ch}	Radius of the channel
R_{head}	Radius of the swimmer head
R_{he}	Radius of the Helmholtz coil pair
S	Swimmer surface
$U_{f,y}$	Swirling flow velocity field, \mathbf{y} - component
$U_{f,z}$	Swirling flow velocity field, \mathbf{z} - component
U_{sw}	\mathbf{x} - component of the swimmer's linear velocity vector
V	Lyapunov function
V_{pp}	Peak-to-peak voltage
V_{rms}	Root-mean square voltage
V_{sw}	\mathbf{y} - component of the swimmer's linear velocity vector
W_{ac}	\mathbf{z} - component of the swimmer's linear velocity vector under magnetic and acoustic fields
$W_{no,ac}$	\mathbf{z} - component of the swimmer's linear velocity vector under magnetic actuation without acoustic fields
W_{sw}	\mathbf{z} - component of the swimmer's linear velocity vector
Y_p	Radiation force function, travelling waves
Y_{st}	Radiation force function, standing waves
Z	Electrical impedance
Δt	Time step
Δt_a	Time step in standing wave simulations
Γ	Swirling flow field strength
Λ	Helix wavelength along the helix centerline
Φ	Acoustophoretic contrast factor

α_n	Scattering coefficient, real component
α_t	Attenuation coefficient
β	Non-dimensional radial position of the swimmer
β_n	Scattering coefficient, imaginary component
χ_i	Arbitrary swimmer orientation vector
ω	Swimmer's angular velocity vector
τ^c	Contact torque acting on the swimmer
τ^m	Magnetic torque acting on the swimmer
τ_{loc}^m	Magnetic torque acting on the swimmer expressed in the local coordinate frame
τ^v	Viscous torque acting on the swimmer
τ^w	Gravitational torque acting on the swimmer
τ^{rad}	Acoustic radiation torque on the swimmer
τ_{loc}^{rad}	Acoustic radiation torque acting on the swimmer expressed in the local coordinate frame
ξ	Arbitrary swimmer position vector
\mathbf{r}	Radial position vector
\mathbf{v}_1	First order velocity field under acoustic wave
δ_w	Threshold distance of swimmer to channel boundaries
\hat{U}_{sw}	Heading velocity in \mathbf{x} - direction
\hat{e}_r	Unit vector in the radial direction
\hat{e}_B	Unit normal of the rotating magnetic field
$\hat{\mathbf{t}}$	Unit vector in the tangential direction of the helical tail
κ	Mason number scaling factor for confined swimming
κ_0	Compressibility of the working fluid
κ_s	Compressibility of the solid particle
λ_a	Acoustic wavelength

λ_h	Helix wavelength
$\mathbf{B}_{\text{control}}$	Control magnetic field vector
$\mathbf{B}_{\text{drive}}$	Driving magnetic field vector
\mathbf{B}	Magnetic field vector
\mathbf{F}^c	Contact force acting on the swimmer
\mathbf{F}^r	Net radial force acting on the swimmer
\mathbf{F}^v	Viscous force acting on the swimmer
\mathbf{F}^w	Gravity force acting on the swimmer
\mathbf{F}^{rad}	Total radiation force on chain of spheres, vector form
\mathbf{F}_{loc}^{rad}	Radiation force expressed in the local coordinate frame
\mathbf{F}_{st}^{rad}	Total radiation force on chain of spheres, standing wave
\mathbf{F}_{tr}^{rad}	Total radiation force on chain of spheres, travelling wave
\mathbf{F}_{st}^r	Radiation force, standing wave
$\mathbf{F}_{sw,t}$	Normal component of the force exerted on the swimmer due to swirling flow
$\mathbf{F}_{sw,t}$	Tangential component of the force exerted on the swimmer due to swirling flow
\mathbf{I}	Identity matrix
\mathbf{K}_d	Derivative control gain matrix
\mathbf{K}_i	Integral control gain matrix
\mathbf{K}_p	Proportional control gain matrix
\mathbf{M}	Mobility matrix of the helix
\mathbf{Q}_l	Rotation matrix from the lab coordinate frame to the local coordinate frame attached to the swimmer
\mathbf{R}_C	Coupling matrix inside the resistance matrix of the swimmer
\mathbf{R}_L	Translation matrix inside the resistance matrix of the swimmer
\mathbf{R}_R	Rotation matrix inside the resistance matrix of the swimmer
\mathbf{U}	Swimmer's linear velocity vector

\mathbf{U}_f^b	Swirling flow velocity field in local coordinate frame
\mathbf{U}_s	Velocity of a point on the swimmer surface
\mathbf{W}_g	Multiplication matrix in swirling flow representation
\mathbf{W}	Skew-symmetric matrix that represents the cross product in Eq. 2.12
$\hat{\mathbf{x}}$	Unit vector in \mathbf{x} - direction
\mathbf{c}_j	Center-of-mass of the spheres in chain-of-spheres approach for $j = 1, 2, \dots, N_{sph}$
\mathbf{e}_i	Orientation vectors of the swimmer for $i = 1, 2, 3$
\mathbf{e}_i^0	Initial orientation vectors of the swimmer for $i = 1, 2, 3$
\mathbf{f}^r	Radial force per unit area on the swimmer
\mathbf{f}^{wall}	Effective normal contact force per area on the swimmer
\mathbf{g}	Gravitational acceleration vector
\mathbf{m}	Magnetization vector of the swimmer
\mathbf{m}^0	Initial magnetization vector of the swimmer
\mathbf{p}	Swimmer position vector
\mathbf{p}_h	Centerline of the helical path of the swimmer
\mathbf{p}_{ref}	Reference swimmer position vector
\mathbf{u}	Velocity field in the fluid
\mathbf{x}	Center-of-mass of the swimmer
\mathbf{x}^0	Initial center-of-mass of the swimmer
\mathbf{x}_l	Position vector of a point on swimmer surface in local coordinate frame
\mathbf{x}_s	Position vector of a point on swimmer surface
μ	Viscosity of the fluid
μ_0	Permeability of the vacuum
ω_a	Angular frequency of the acoustic wave
ω_m	Angular frequency of the magnetic field
ω_x	\mathbf{x} - component of the swimmer's angular velocity vector

ω_y	\mathbf{y} - component of the swimmer's angular velocity vector
ω_z	\mathbf{z} - component of the swimmer's angular velocity vector
$\bar{\theta}_{ax}$	Normalized wobbling angle of the swimmer
ϕ	Rotation angle around \mathbf{z} - axis
ϕ_1	First order potential field
$\phi_{i,tr}$	Incident potential field, travelling wave
$\phi_{s,tr}$	Scattered potential field, travelling wave
ρ	Fluid density
ρ_0	0th order fluid density
ρ_1	1st order fluid density
ρ_2	2nd order fluid density
ρ_s	Solid density
σ_{ij}	Stress tensor elements for $i = 1, 2, 3$ and $j = 1, 2, 3$
$\tau^{v,bulk}$	Viscous torque acting on the swimmer in near-bulk swimming conditions
$\tau^{v,confined}$	Viscous torque acting on the swimmer in confinement
τ^x	Torque in \mathbf{x} - direction
τ^y	Torque in \mathbf{y} - direction
\mathbf{q}	State vector containing radial position error values
θ	Radial orientation angle of the normal of a point on swimmer surface
$\theta_{ax,max}$	Maximum wobbling angle of the swimmer based on geometric constraints
θ_{ax}	Wobbling angle of the swimmer
θ_h	Helix angle
θ_{xy}	Misalignment angle of the swimmer on x-y plane
θ_{xz}	Misalignment angle of the swimmer on x-z plane
a	Sphere radius in chain of spheres approach
a_c	Control gain coefficient that alters tilting in the \mathbf{z} - direction

b_c	Control gain coefficient that alters tilting in the \mathbf{y} - direction
c_0	Speed of sound in the working fluid
c_n	Normal resistive coefficient
c_t	Tangential resistive coefficient
c_{na}	Scattering coefficient
d	Minor radius of the helix
e_y	Position error in \mathbf{y} - direction
e_z	Position error in \mathbf{z} - direction
f_a	Acoustic field frequency
f_m	Magnetic field rotation frequency
f_{rep}	Burst wave repetition frequency
h	Distance of a particle to a velocity node
h_n^2	Hankel function of second kind
j_n	Spherical Bessel function of order n
k	(As a superscript) Current time step
k	Acoustic wave number
k_h	Helix wave number
n	Bessel function order
p	Pressure
p_0	0th order pressure term
p_1	1st order pressure term
p_2	2nd order pressure term
p_a	Pressure amplitude
p_b	Background pressure field
p_i	Incident pressure field
p_{sc}	Scattered pressure field

r	Radial position of the center-of-mass of the swimmer
r_c	Radius of curvature of the swimmer head
r_s	Radial position of a point on the swimmer surface
r_t	Radius of swimmer trajectory
s	Body coordinate index
t	Time
t_a	Swimming period with magnetic and acoustic fields together
t_m	Swimming period with magnetic field only
t_{final}	Final time step
u	Swimming velocity in the axial direction
v_f	Poiseuille flow velocity in the channel
x	Swimmer position vector, \mathbf{x} - component
y	Swimmer position vector, \mathbf{y} - component
y_{ref}	Swimmer reference position vector, \mathbf{y} - component
z	Swimmer position vector, \mathbf{z} - component
$z_{h,max}$	Maximum of the axial coordinate in placement of the spheres in the chain of spheres approach
$z_{h,min}$	Minimum of the axial coordinate in placement of the spheres in the chain of spheres approach
z_{ref}	Swimmer reference position vector, \mathbf{z} - component
F_{tr}^r	Radiation force, travelling wave
Ma	The Mason number

1. INTRODUCTION

Inspired by flagellated natural organisms such as *Escherichia coli*, artificial helical microswimmers hold great potential in becoming the robotic agents for the fluidic environments at low scales. Potential applications include micromanipulation, targeted drug delivery, opening of clogged arteries and micromixing. These swimmers, ranging in size from nanometers to millimeters, are generally actuated by external magnetic fields. The majority of magnetized helical swimmers consists of two main parts: A helical tail which enables propulsion and a head that contains the magnetized material for enabling actuation. Under a rotating magnetic field, the head rotates the whole swimmer as it tries to adjust its magnetization vector with the rotating field. The rotation of the field leads to propulsion through the rotation of the helix.

Magnetic actuation has several benefits: Its external nature means there is no need for on-board actuation mechanisms such as motors. No visual contact is required for swimmer actuation. Magnetic actuation is also bio-compatible which is quite important as many potential use cases are biomedical. These benefits underlie the reason magnetized helical swimmers are popular in the literature both for *in vivo* and *in vitro* applications. On the other hand, the magnetic actuation brings about several modes of instability, resulting in wobbling and stutters in swimmer motion.

The objective of this thesis is to characterize the oscillatory trajectories of magnetized helical swimmers and propose solutions to suppress them to enable controlled navigation which is crucial considering the medical use cases. The modes of instability are investigated and characterized in detail with respect to physical parameters of the system. Next, a control algorithm is introduced that successfully suppresses the oscillatory trajectories. Noting that the feedback control algorithm requires swimmer position information which is not always available at a great accuracy, the dissertation also proposes a passive way to eliminate the oscillatory trajectories through the means of acoustic fields. Acoustic fields are widely adopted in medical applications for their bio-compatible and non-invasive nature, thus, the fields complement the magnetic fields very well. The effects of acoustic radiation

on helical swimmers are investigated both numerically and experimentally. The numeric approach approximates a slender helix as an array of spheres. There are no known analytical formulae for the acoustic radiation force on helices while simple analytical formulae are available for spheres. It is shown that the total acoustic force on the helix can be closely approximated through the sum of the forces acting on the spheres placed along the helical structure. This model is incorporated into a resistive force theory-based model of magnetized helical swimming to derive the trajectories and velocities of swimmers under acoustic actuation. In experiments, helical swimmers made out of thin wires are actuated both magnetically (with a Helmholtz coil setup) and acoustically (with immersed transducers) in viscous liquid. The effects of acoustic field on propulsion velocity is demonstrated and simulations are utilized to confirm the experimental observations.

The findings of this thesis are expected to not only improve the understanding on the stability of helical microswimmers but also provide insight into solutions that do and do not require any feedback for controlled navigation which is a crucial element for biomedical applications. Several novel computational models presented in the thesis simplify the evaluation of trajectories of helical swimmers in magnetic and/or acoustic fields.

1.1 Background

In accordance with the multi-disciplinary nature of the thesis subject, magnetic helical swimmers will be introduced first and then the studies on acoustic radiation and actuation will be discussed through numerical and experimental studies.

1.1.1 Swimming with a Helical Tail

Microswimmer locomotion ensues from the dominance of viscous effects at small scales where inertial effects are negligible. At low Reynolds numbers, forces and torques act instantaneously. This also means that swimming cannot be achieved by time-reciprocal motion (Purcell, 1977). Linear and angular swimming velocities are related to the forces and torques on the swimmer through a resistance matrix whose

elements depend on factors such as the swimmer geometry and boundaries nearby. Man & Lauga (2013) derive the full resistance matrix for helical swimmers in bulk fluid using the resistive force theory, which relates the hydrodynamic force acting on a helix locally through normal and perpendicular drag coefficients and it is widely used in modeling of helical swimmers (Gray & Hancock, 1955). On the other hand, the theory does not take long-range hydrodynamic interactions into account which are crucial especially for thick tails and near-boundary swimming (Lighthill, 1976).

Natural microorganisms swim in viscous media in several different ways: Some organisms deform their body to move which is a slow but simple way (Alt & Hoffmann, 2013). Other organisms have developed specialized structures to move such as the cilia in the paramecium or flagella in bacteria (Lauga, 2016). The bacteria swim by rotating their flagella in both directions, resulting in two modes of rotation: The swimmer is said to be in the pusher-mode if the flagella is pushing the head and it is called the puller-mode if the flagella is pulling the head. Flagellated microorganisms swim in the pusher-mode most of the time and this is one of the reasons why they follow circular trajectories and accumulate around surfaces (Berke et al., 2008; Galajda et al., 2007). On the other hand, confinement is helpful in achieving directed swimmer motion: It was observed that the bacteria have higher velocities in 10 μm channels than in 50 μm channels Berg & Turner (1990).

The major challenge in realizing an artificial micro-swimming structure lies in the method of actuation. There are several methods actively studied in the literature. One of them is chemical actuation by using Janus particles. These particles are composed of two different materials at each side of the particles; this structure can be functionalized such that one side would react with the surrounding fluid and this would generate motion. Such particles often require toxic environments such as hydrogen peroxide and this limits their use in biomedical applications (Xuan et al., 2014). Furthermore, the swimmer is destroyed once it is used. Another method involves the use of light: In a recent study, cylindrical microswimmers made of liquid-crystal elastomers that response to light are manufactured (Palagi et al., 2016). By exposing light to these swimmers periodically as strips, propulsion is achieved through peristaltic motion. This method requires continuous visual contact with the swimmer. In comparison to several different methods of actuation, magnetic fields appear to be the most advantageous: They are bio-compatible and external; they don't require specific fluids and they work without any visual contact with the swimmer (Martel, 2013). Magnetized helical swimmers are best suited for magnetic manipulation through a rotating field as the gradient fields pose health risks beyond a certain strength and controlled navigation is more challenging with field gradients Abbott et al. (2009).

Artificial helical microswimmers are inspired by the flagellated bacteria. Among the initial attempts was Dreyfus et al.'s (2005) bio-hybrid swimmer that was composed of a red blood cell and a linear chain of colloidal magnetic particles. When a time-varying magnetic field is applied, the tail exhibits undulating motion and this results in net propulsion. With the developments in micro fabrication technologies, completely artificial swimmers could be manufactured: Zhang et al. (2009) report a self-scrolling methodology to achieve helical ribbons made from GaAs/Ga bi-layer structure. The helical structure has a diameter of $2.8 \mu\text{m}$ and a length of several tens of μm . The ribbon has a magnetic head at one end which is used for propulsion through rotating magnetic fields. More recent studies utilize advanced technologies such as 3D direct laser writing to manufacture helices (Peters et al., 2016; Tottori et al., 2012).

1.1.2 Modes of Instability

Two distinct cases of instability are reported for magnetically actuated helical swimmers in the literature. The first case is the wobbling of helices at low frequencies as observed experimentally by Peyer et al. (2010) and Ceylan et al. (2019). Man & Lauga (2013) characterize the wobbling of rotating slender helices with Mason number (Ma), which is defined as the ratio of viscous and magnetic torques, and find that the wobbling angle increases as Ma decreases. This points to either high magnetic field strength or low rotation rate of the swimmer as the sources of instability in terms of magnetic actuation parameters. The other form of instability is called step-out, and occurs when the strength of the magnetic field is not sufficient to produce a magnetic torque to overcome the viscous torque (Zhang et al., 2009). Low-frequency wobbling of helical swimmers is observed in bulk swimming, whereas step-out occurs in bulk (Zhang et al., 2009) or confined swimming (Caldag et al., 2017).

Effects of hydrodynamic interactions on swimmers at low Reynolds number have been studied extensively in the literature. Flagellated bacteria are observed to swim in circular trajectories near a surface (Lauga et al., 2006; Liu et al., 2014). The tail and the head rotate in opposite directions in biological swimmers for torque-free swimming and it results in a net hydrodynamic interaction force and torque that push the swimmer to follow a circular trajectory (Lauga et al., 2006). On the other hand, the misalignment of the tail relative to the body is argued to contribute to helical trajectories as well (Hyon et al., 2012). Spagnolie & Lauga (2012) approx-

imate swimming of the flagellated bacteria with a superposition of a force dipole, quadrupole, source dipole and a rotlet dipole. As the term with the leading order, the force dipole is preferred by many authors to represent swimming of the flagellated bacteria, including Berke et al. (2008) who explain the attraction towards surfaces with the dipole interactions. Organisms with longer flagella relative to the cell body redirect the swimming towards the boundaries (Spagnolie & Lauga, 2012). There exists a critical tail length for which the pitching angle changes its sign.

Swimmer stability inside channels is studied for spherical particles. Zöttl & Stark (2012) model the hydrodynamic interactions with the boundaries by a dipole approximation to study the stability of a pointlike swimmer between two parallel plates in a Poiseuille flow and they find that a pusher (which they identify with a positive dipole strength) tends to follow a circular trajectory around the centerline of the channel, close to the boundaries. The pullers are reported to follow a straight path at the center of the channel (Zöttl & Stark, 2012). The pushers are generally characterized with an outward flow with respect to the swimmer while the flow is inwards in the puller-mode (Klindt & Friedrich, 2015). The flow rate determines whether the pusher will cross through the centerline of the channel or oscillate around the channel boundaries. de Graaf et al. (2016) distinguish between the pusher and puller-mode swimming based on the relative placement of the force dipole on the fluid with a fixed direction. If the dipole is in the front of the swimmer, with respect to the swimming direction, the swimmer is a puller and it is a pusher if the dipole is behind. The authors carry out lattice-Boltzmann simulations and far-field calculations for a rod-shaped swimmer between two parallel plates and cylindrical channels and observe helical trajectories for pushers and straight trajectories for pullers. The distinctive trajectories are observable for plate separations up to ten times the length of the swimmer. Dipole and octupole moments are reported to create attraction (repulsion) for pushers (pullers) while quadrupole moments cause pure oscillatory motion.

Low Reynolds locomotion of squirmers, which move in the fluid by the means of surface deformation exhibit pusher and puller modes clearly. Zhu et al. (2013) developed a model for a spherical squirmer inside a circular channel using the boundary element method. Authors report that pushers crash to the walls when the repulsive force that stabilizes the pullers are reversed. Moreover, whether the pullers swim at the center of the channel or closer to the wall is determined by the strength of the force dipole generated by the squirmer (Zhu et al., 2013). Chacón (2013) studied the motion of spherical swimmers in the Poiseuille flow and reported that small finite periodic oscillations in the swimming velocity influence the trajectories depending on the position and orientation of the swimmer in the channel and that efficient

upstream (downstream) swimming takes place at (away from) the center. Ishimoto & Gaffney (2013), on the other hand, add a rotlet dipole to a spherical squirmer to approximate a flagellated bacteria. They find that a positively oriented rotlet dipole results in a counter-clockwise circling when the swimmer is close to a no-slip surface. Interestingly, swimmer orientation and distance from the surface remain unaffected from the introduction of the rotlet.

Experiments on mm-sized artificial helical swimmers are reported in the literature and the effects of confinement, tail length, magnetic field rotation rate and flowrate on the trajectories of swimmers are studied (Acemoglu & Yesilyurt, 2015; Caldag et al., 2017). One of the critical observations was that the pusher-mode swimmers follow helical trajectories while the puller-mode swimmers follow straight trajectories at the centerline of the channel most of the time with the exception of wobbling of the tail at high frequencies before step-out. The results indicate that the hydrodynamic interactions with the wall play an important role in the trajectories of confined swimmers.

1.1.3 Controlled Navigation of Helical Microswimmers

Modes of unstable motion necessitate proper control of these swimmers which has seen a recent interest in the research community. Earlier studies such as Ghosh & Fischer (2009) and Tottori et al. (2012) show accurate in-plane control of helical swimmers in bulk fluid but they depend on open-loop algorithms due to challenges in visual feedback as stated in Xuan et al. (2014). Xuan et al. (2014) are among the first to develop a closed loop control algorithm where they achieve planar path following based on the orientation error. Following this study, Oulmas et al. (2018) realize the closed-loop control by linearizing the swimmer dynamics through a chained formulation for tracking any 3-dimensional path with sub-millimetric accuracy. The control relies on the determination of the ideal swimmer orientation to steer the swimmer towards the desired path. Tilting is achieved by utilizing three pairs of Helmholtz coils which allows rotation of the swimmer towards any direction. The authors demonstrate that the closed-loop control is robust enough to overcome disturbances due to boundary effects down to 2.5 mm for a swimmer with a length of 14 mm and diameter of 1 mm (Oulmas et al., 2018). A recent study by Leclerc et al. (2019) demonstrates controlled navigation both inside and outside of a channel albeit with lower accuracy. Most of these studies rely on accurate information

on swimmer position and orientation at the same time which are hard to obtain especially considering potential *in vivo* applications.

1.1.4 Acoustic Radiation Force

Acoustic radiation force is a time-averaged force in an acoustic field. The evaluation of the force is challenging for intricate structures but analytical results for simple structures exist in the literature. The theoretical framework to evaluate acoustic radiation force on a sphere is established by King (1934). The harmonic nature of the acoustic wave implies zero force on an object in the field due to the time-average of a sinusoidal wave being equal to zero. The radiation force arises from the second-order pressure terms which have a non-zero time-average. Later, the formulation is extended to account for the cases of compressible particles and viscous media (Hasegawa & Yosioka, 1969; Settnes & Bruus, 2012). Hasegawa & Yosioka (1969) solve the radiation force problem under single dimensional travelling waves by expressing the incident and scattered velocity potentials as spherical Bessel and Hankel functions. The scattering coefficient is evaluated from these functions the force is integrated around the surface of the sphere by utilizing the coefficient. However, as the radiation force is time-averaged and the particle is oscillating during that time period, there appears the problem of what surface to take for integration. The authors resolve it by integrating the force around a fixed spherical surface (that is larger than the original spherical surface) and add a secondary momentum flux correction term (Hasegawa & Yosioka, 1969). This approach is shown to work for any spherical surface encompassing the particle. Another approach is the utilization of net loss of steady state linear momentum into the surface of the object (Maidanik & Westervelt, 1957). Both of these approaches are shown to give the same results (Hasegawa, 1977). Similar calculations are carried out for spheres in 1-dimensional standing waves (Hasegawa, 1979) and cylinders in both travelling and standing waves (Hasegawa et al., 1988; Haydock, 2005). The calculations show that the particles migrate to either the velocity nodes or anti-nodes (Doinikov, 2003), depending on their relative positions.

The models discussed above do not take viscous and thermal effects into account. Thermal and viscous effects become significant if the particle size is smaller than the viscous/thermal penetration depths. According to Settnes & Bruus (2012), the inviscid fluid assumption remains valid if the particle size is larger than $3 \mu\text{m}$ for a 1-MHz application in water. In the same study, the authors derive the radiation

force formulae for spherical particles under standing or travelling waves. Wang & Dual (2011) derive the force expressions for cylinders in viscous fluids and they find out that viscous effects increase the acoustic radiation force. The increase in radiation force is much more notable in plane travelling waves than in plane standing waves. The viscosity mainly influences the force due to shear stresses rather than compression.

While the analytical solutions discussed above are only applicable for simple shapes, numerical solutions suitable for obtaining the acoustic force on arbitrary shapes can be classified under two broad categories. In the first one, complete flow fields under acoustic waves are solved by introducing the acoustic wave as a pressure wave in a compressible fluid domain. Wang & Dual (2009)'s 2-D finite volume method-based (FVM) model evaluates the acoustic radiation force for cylindrical objects through the complete solution of Navier-Stokes equations. Their results match very well with the analytical calculations for a wide range of geometric parameters. Since the forces are evaluated from the complete solution of compressible Navier-Stokes equations, a simulation for a structure as simple as a cylinder takes hours to complete. Muller et al. (2012) develop a multi-step finite-element model in which they solve for particles suspended in a microfluidic device excited with acoustic waves. They first solve for first-order acoustic fields which are then used to compute second order fields from which acoustic radiation force is determined. The evaluated forces are then exerted on the particles to compute their trajectories.

On the other hand, the use of Helmholtz equations (which is derived from a first-order time-harmonic extension of Navier Stokes equations), coupled with the perturbation approach, simplifies the solution process significantly, resulting in a dramatic reduction in computational cost. Glynne-Jones et al. (2013) present a 2-D axisymmetric finite element method (FEM) model in which the acoustic radiation force on a spherical object can be calculated in several seconds with a good match in the evaluated radiation forces with the theoretical results in a frequency domain study. The authors derive a density and compressibility ratio map where one can deduce whether a particle will move to a pressure node or antinode. Glynne-Jones et al. (2013)'s approach is extended to 3 dimensions in Garbin et al. (2015) where the acoustic radiation forces and torques are evaluated for spheroid structures and the results are verified with experiments and theory. The authors model an infinite domain by applying perfectly matched layers (PMLs) at the outer boundaries. They hint that acoustic fields can be used to align ellipsoidal shapes such as cells. Wijaya & Lim (2015) study the forces and torques on spheroids and ellipsoids extensively. The alignment of the spheroid is reported to affect the exerted radiation force up to 26%. A prolate (oblate) spheroid will rotate in counterclockwise (clockwise) di-

rection until the stable orientation angles of 0° (90°) is achieved. When a spheroid has an orientation angle of 55° , the force is equal to that of a sphere with the same volume. Baasch et al. (2017) simulate multiple spheres inside a microfluidic channel with collision dynamics taken into account. They report that the cross-interactions between the spheres are negligible if the acoustic contrast factor is low. Another study by Collino et al. (2015) simulates the spacing between columns of microparticles under acoustic actuation by approximating each rod as an array of spheres with the same cross-sectional area as the rod.

1.1.5 Acoustically Actuated Swimmers

Acoustic manipulation of particles (acoustophoresis) is used for biomedical applications such as cell/particle sorting (Petersson et al., 2007). These applications generally utilize acoustic streaming phenomenon. On the other hand, a more recent biomedical application demonstrates the usage of acoustic radiation force to measure blood clot stiffness *in vitro* (Wang et al., 2015). The authors place a focused ultrasonic transducer operating at 10 MHz next to a polystyrene box which contains a mixture of blood plasma and polystyrene beads with a $15 \mu\text{m}$ diameter. The transducer is reported to exert around 2 MPa pressure at maximum and attenuation coefficient inside plasma is evaluated as $0.115 \text{ dB} \cdot \text{cm}^{-1} \cdot \text{MHz}^{-1}$. With this setup, the beads exhibit motion under acoustic waves and the speed of the beads are related to the Stokes drag from which the clot stiffness can be measured. In another study, acoustic fields are used to trap Janus particles made of Platinum (Pt) and polystyrene (PS) (Takatori et al., 2016). Normally, these Janus particles exhibit Brownian motion. With the acoustic tweezer turned on, the particles are confined within the borders of a well in which they can still exhibit Brownian motion but they cannot get outside the boundaries of the well.

The usage of acoustic fields for micro-swimming applications is quite recent. Wang et al. (2012) are among the first to use acoustics for autonomous swimming. They manufactured metallic nanowires (made of Au and Ru) with a length of 1-3 μm and diameter of 300 nm. Placing the rods in a cell with an acoustic transducer glued from the bottom, the rods are observed to be lifted up from the bottom of the cell once the transducer is turned on. Once levitated, the nanowires exhibit motion in random directions. The seemingly random direction of motion is associated with the imperfections on the surface. Swimmer velocity is found to be a function of transducer voltage, frequency and position of the rods. At the resonance frequency

of the setup, 3.776 MHz, the wires at the center of the setup move very fast while the wires away from the center move slowly. Even a 1% change in the frequency results in a sharp drop in the velocity of nanowires that are close to the center but the change in frequency activates the wires in another region of the cell. This enables selective actuation of the wires by only changing the frequency. Different types of single metal wires and bimetallic wires are reported to behave similarly in their respective group.

Wang et al. (2012)'s work was followed with similar studies detailing different aspects of metallic nanowire swimmers. One study investigates the shape and material effects where the authors find that the swimmer moves towards the concave end of the wire due to acoustic streaming effects. (Ahmed et al., 2016). They deduce the swimming is induced by streaming as the swimming speed decreases with length which increases the resisting drag force. In another study, the researchers introduce magnetic fields to Au-Ni-Ru nanowires in order to enable directed motion (Ahmed et al., 2013). The wires are demonstrated to function inside living human cells, allowing for use in biomedical applications (Wang et al., 2014). A disadvantage of metallic swimmers is that they need to be actuated at high frequencies (MHz scale) to observe resonance-based effects. High-frequency waves are known to attenuate fast and this may pose a problem for biomedical applications where highly viscous liquids may dampen the waves. Kaynak et al. (2017) introduce a swimmer made of a polymer mixture *in situ*. The pointed needle shaped swimmers resonate at frequencies as low as 4.6 kHz. The swimmers move by the microstreaming flow generated at the needle-like end of the tail. These swimmers can move only in the direction their tail points to but the authors also demonstrate swimmers with tails perpendicular to the body which continuously rotate in a single direction. With a swimmer length of around 180 μm , the authors achieve velocities more than six body lengths per second.

Another interesting demonstration of acoustic swimmers is bubble-based swimmers. These swimmers are generally coated with hydrophobic material and have a hole inside. When submerged in water, an air bubble forms inside and this bubble can be vibrated with acoustics to enable propulsion. Ahmed et al. (2015) are among the first to manufacture this kind of swimmer. These swimmers operate at acoustic frequencies where the acoustic wavelength is much larger than the bubble diameter, which is generally several μm in the studies reported here. While the swimmer motion is still at low Reynolds number environment due to small scales, the dynamics of the bubble occur at high Re numbers (Ahmed et al., 2015). In fact, if bubble dynamics remain at low Re number, it is shown that the flow fields are highly time-reversible, resulting in no net propulsion (Feng et al., 2015). In water, swim-

ming speeds up to 50 body lengths per second are obtained but in a 50% glycerol mixture the swimming speed radically decreases to 1/100th of the values observed in water. One advantage is that the swimming speed has a quadratic dependence on voltage, so comparable swimming velocities can be achieved at higher voltages. A more recent study reported swimming speeds of up to 17500 body lengths per second for a swimmer with dimensions of 20x20x26 μm (Louf et al., 2018). Even though the swimming is in a certain direction, the authors note that navigation can be achieved by placing multiple transducers and actuating them separately. A more recent example of a bubble-based swimmer is magnetically coated for directed swimming based on the direction of the magnetic field applied (Ren et al., 2019). Since the propulsion velocity changes with respect to the direction of magnetic field, the authors say that it is possible to selectively propel certain swimmers in a swarm by aligning the magnetic layers on the swimmers differently.

Work on acoustic swimmers with flagellum-like tails has been little. Ahmed et al. (2016) report a swimmer with a Ni-Au head and a flexible tail made of polypyrrole. The swimmer is 15-20 μm long and has a diameter of 0.3-0.6 μm . They use structural resonance of the tail to form streaming under acoustic fields which enables propulsion in both standing and travelling acoustic waves. They achieve velocities around 3-4 body lengths per second at 10 V. The authors also test whether the head by itself moves under acoustic field, the velocity ends up less than 10 $\mu\text{m/s}$. The authors explain this with the fact that the resonance frequency of the metallic head is way higher at around MHz range. Li et al. (2015) report a magneto-acoustic hybrid swimmer with a helical tail. This swimmer is made of Au with Ni coating for allowing magnetic actuation. The acoustic and magnetic fields are used separately for motion in opposite directions. Under acoustic field, the swimmer moves in its tail direction (as in the puller-mode swimming) while magnetic field is used to propel the swimmer in its head direction (as in the pusher-mode swimming). The authors also test head-only and tail-only swimmers and find out that the acoustic propulsion is at its highest at the original swimmer with a head and a tail. The swimmers are shown to move effectively in viscous biomedical fluids such as serum and blood. Another interesting aspect of these swimmers is that they are collected to acoustic nodes when ultrasound is turned on in a short time (in 5 seconds). When the acoustics is turned off and the magnetic field is turned on, the collected swimmers come loose and get separated from each other. The process is said to be fully reversible and it allows for easy collection of the swimmers in a single spot.

1.2 Novelties of the Thesis

The stability of helical swimmers is not yet fully understood. Most of the numerical studies that investigate the topic are either independent from the experimental observations or focus on biological swimmers. The kinematic simulation model for helical swimmers in this study helps in understanding the phenomena observed in the experiments with artificial swimmers in Caldag et al. (2017) as the helical swimmer geometry in the model is based on the real-life swimmer in that study. As the inertial effects are negligible in the Stokes regime, the model solves for the snap-shot Stokes equations via a computational fluid dynamics (CFD) model which are then integrated via kinematic relations to obtain complete 3-dimensional swimmer trajectories under confinement with a reasonable computational cost. The kinematic model updates the position and the orientation of the swimmer by using the linear and angular velocities from the CFD model at each instant. In addition to the viscous force, the external magnetic torque, the gravity force and the normal contact force on the swimmer are also considered in the CFD model. The phenomena observed in the experiments are successfully replicated in the kinematic model and some of the phenomena left unexplained in Caldag et al. (2017) are fully explained. An improved resistance force theory formulation of helical swimmers is introduced as well, which incorporates an additional swirling flow field to simulate in-channel swimming of helices and reduce the computational cost even further for complete trajectory simulations.

After the discussion on the stability of helical microswimmers, the dissertation presents a feedback control algorithm to suppress the oscillatory trajectories for controlled navigation which is crucial for biomedical applications. The algorithm is based on magnetic steering of helical swimmers like the state-of-the art. The novelty of this algorithm lies in the fact that it doesn't rely on swimmer orientation information to steer the swimmer towards the desired path whereas other methods in the literature require orientation information. Swimmer position information is shown to be sufficient for wobbling angles below 20° (which, by itself, is a very large value and indicates high degrees of wobbling). For *in vivo* use scenarios such as targeted drug delivery, extracting proper position information is quite challenging and extraction of swimmer orientation is nearly impossible. In that sense, the proposed control algorithm is much better suited for practical use.

The dissertation also explores how acoustic fields can help in improving swimmer stability as a way that does not require feedback from the system. Despite being one

of the highly researched type of artificial swimmers in the literature, the interaction of magnetized helical swimmers with acoustic fields is left unexplored. The computational and experimental studies here aim to fill this gap. The computational approach to evaluate the acoustic radiation force on slender helical structures, called chain-of-spheres, is novel. Normally, the computational cost of calculating acoustic radiation force on 3-dimensional geometries require finite-element simulations that are highly costly. Large computational cost is a barrier for quick modelling of novel acoustic radiation-based devices. The approach presented here is expected to improve the modelling capabilities of the researchers to build more sophisticated radiation-based systems. The model in Collino et al. (2015) is similar to ours but there are several key differences. First is that they don't enforce a volume-matching constraint to achieve accurate radiation force values. The authors are only interested in the spacing between the rods, hence, they don't need high accuracy. Secondly, their model remains application-specific whereas the methodology proposed here can be applied to other slender and complex geometries. Third, the authors only work on standing wave fields while our work covers both the standing and travelling waves and the significant results of the thesis are mostly obtained under travelling waves.

Another major contribution of this dissertation is that it presents the trajectories of magnetically actuated helical swimmers under both the magnetic and acoustic fields for the first time. By coupling the computational model for the calculation of acoustic radiation force with a resistive force theory-based model of magnetized helical swimmers, it is possible to simulate the complete 3-dimensional trajectories. This is a significant step in terms of simulating not only an instant but the whole duration of swimming under acoustic fields as it had not been studied before for intricate structures.

The experiments complement the numerical work by demonstrating the effects of acoustic actuation on an actual magnetized helical swimmer. The novel position control algorithm is used to initialize the acousto-magnetic experiments from the same initial position for improving repeatability of the experiments. The setup presented here uses immersed acoustic transducers that require no acoustic matching. The relationship of viscosity with the propulsion velocity of the swimmer is investigated within the context of the results and a matching between experimental observations and simulation results is achieved.

The findings of this dissertation have resulted in several publications with full citations given below:

- Caldag H. & Yesilyurt S. (2018) Dynamics of artificial helical microswimmers under confinement. *In: International Conference on Nanochannels, Microchannels, and Minichannels, ASME 2018 16th International Conference on Nanochannels, Microchannels, and Minichannels, ASME.*
- Caldag, H. O. & Yesilyurt, S. (2019). Trajectories of magnetically-actuated helical swimmers in cylindrical channels at low Reynolds numbers. *Journal of Fluids and Structures*, 90, 164–176.
- Caldag, H. O. & Yesilyurt, S. (in press). Steering Control of magnetic helical swimmers in swirling flows due to confinement. *In: International Conference on Robotics and Automation (ICRA 2020), Paris, France.*
- Caldag, H. O. & Yesilyurt, S. (in press). A Simple Numerical Tool for the Evaluation of Acoustic Radiation Force on Helices. *In: International Ultrasonics Symposium (IUS 2020), Las Vegas, Nevada*

The following journal article based on the findings in this dissertation is submitted and under review as of August 2020.

- Caldag, H. O. & Yesilyurt, S. Acoustic Radiation Forces on Magnetically Actuated Helical Swimmers.

2. Stability of Magnetically Actuated Helical Swimmers

Helical swimmers exhibit several modes of instability such as wobbling and step-out (Caldag et al., 2017; Man & Lauga, 2013; Zhang et al., 2009). These modes of instability are well-studied in the literature. However, there is another mode of instability, distinct from these two, that is observed in confined environments, called the pusher-mode instability (Caldag et al., 2017). Confined swimming is practically relevant considering *in vivo* environments such as arteries. Understanding this mode of instability is crucial for enabling controlled navigation in such environments. This chapter characterizes the pusher-mode instability with the help of a kinematic model that resorts to snap-shot solutions of Stokes equations. Pusher-mode instability is characterized with respect to key parameters of the system and the distinctive features of the pusher-mode instability are elaborated.

2.1 The Kinematic Model

The geometric setup is shown in Fig. 2.1 where the swimmer with a left-handed helical tail and a cylindrical head with curved edges is placed inside the cylindrical channel of diameter D_{ch} . Length of the swimmer's tail is denoted by L , wavelength by λ_h , amplitude by A_h and the diameter by d . The cylindrical head has a length of L_{head} and a diameter of D_{head} . The radius of curvature of the edges is r_c . The channel length is set to a very low but acceptable value, which is almost twice as long as the length of the swimmer, and helps to reduce the computation time while the end effects on the swimmer remain negligible. The swimmer geometry is representative of the swimmers used in our experiments (Acemoglu & Yesilyurt, 2015; Caldag et al., 2017), and it is also similar to many others used in the literature (Ghosh & Fischer, 2009; Tottori et al., 2012). Swimmers are identified with the letter "L" followed by a number that represents the number of waves on the tail.

Pusher and puller swimming modes, which are defined based on the position of the head with respect to the tail and the swimming direction, are also depicted in Fig. 2.1. For a left-handed helical tail, the pusher-mode swimming occurs when the swimmer rotates in the counter-clockwise direction and the puller-mode in the clockwise direction. Gravity \mathbf{g} acts in the negative \mathbf{y} - direction.

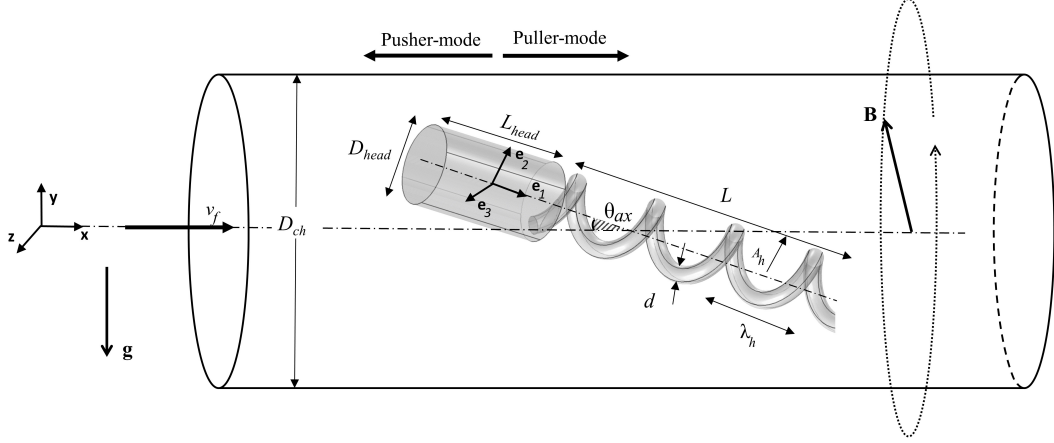


Figure 2.1 Geometric parameters of the swimmer and the channel, representations of rotating magnetic field \mathbf{B} , gravity vector \mathbf{g} and channel inlet flow with a parabolic profile and average velocity, v_f . Forward (head direction, pusher-mode) and backward (tail direction, puller-mode) motion of the swimmer.

Fluid motion is governed by the steady Stokes equations at low Reynolds numbers as the time-dependent effects such as the history and added mass forces are negligible as long as the magnetic rotation frequency, f_m , is not very high (Wang & Ardekani, 2012):

$$(2.1) \quad \nabla^2 \mathbf{u} - \nabla p = 0, \quad \nabla \cdot \mathbf{u} = 0$$

Here, \mathbf{u} and p are the non-dimensional fluid velocity field and the pressure, respectively. The length scale is the wavelength of the tail, λ_h , while the time scale is f_m^{-1} . The pressure is non-dimensionalized with $f_m \mu$.

The swimmer's linear and angular velocities, \mathbf{U} and $\boldsymbol{\omega}$ are calculated from the force and torque balances:

$$(2.2) \quad \mathbf{F}^v + \mathbf{F}^w + \mathbf{F}^c = 0$$

$$(2.3) \quad \boldsymbol{\tau}^v + \boldsymbol{\tau}^m + \boldsymbol{\tau}^w + \boldsymbol{\tau}^c = 0$$

where superscript “ v ” stands for viscous, “ m ” for magnetic, “ w ” for gravity and “ c ” for contact. These forces and torques depend on the radial position and orientation of the swimmer and are updated at each time step in the simulation. Torques are evaluated with respect to the center of mass of the swimmer, which is placed at the center of the head; since the head is made of a heavy magnet whereas the tail is made of plastic.

The viscous force is obtained from the integration of fluid stress on the swimmer:

$$(2.4) \quad F_j^v = \int_S \sigma_{ij} n_i dS$$

where σ_{ij} are the elements of the stress tensor for $i = 1, 2, 3$ and $j = 1, 2, 3$, n_i denotes the i^{th} component of the surface normal, S is the swimmer surface, and summation over repeated indices is implied. The viscous torque exerted by the fluid with respect to the center of mass of the swimmer is:

$$(2.5) \quad \tau_j^v = \int_S (\mathbf{x}_s - \mathbf{x}) \times \sigma_{ij} n_i dS$$

The magnetic field rotates around the \mathbf{x} - axis (Fig. 2.1), which is also the centerline of the channel, and exerts a magnetic torque on the swimmer:

$$(2.6) \quad \boldsymbol{\tau}^m = \mathbf{m} \times \mathbf{B}$$

where \mathbf{m} is the magnetization vector of the swimmer with a magnitude of m_0 .

The rotating field is achieved by out-of-phase sinusoidal fields and given by:

$$(2.7) \quad \mathbf{B} = B_0 \left[0 \quad \cos(\omega_m t) \quad \sin(\omega_m t) \right]'$$

where B_0 is the amplitude of the magnetic field, $\omega_m = 2\pi f_m$ is the rotation rate and its sign implies the rotation direction of the left-handed helical tail that pushes the swimmer when $\omega_m > 0$ and pulls it when $\omega_m < 0$.

Contact conditions are satisfied if any point on the swimmer is closer to the wall than a clearance δ_w . Normal contact force is set to the negative value of the net radial force, if the radial force is outwards, otherwise, it is 0. The local effect of the contact force is represented by an effective normal contact force per area on the swimmer where the local contact conditions are met:

$$(2.8) \quad \mathbf{f}^{wall} = \begin{cases} \frac{-\mathbf{F}^r}{\int_{\{r_s \in S | R_{ch} - r_s < \delta_w\}} dS} & \text{if } \mathbf{F}^r = -\int_S \mathbf{f}^r dS > 0 \quad \text{and} \quad R_{ch} - r_s < \delta_w \\ 0 & \text{otherwise} \end{cases}$$

where $R_{ch} = D_{ch}/2$ and r_s is the radial position of a point on the swimmer surface, S . The fraction represents the average contact force per area in regions on the swimmer where the contact condition is satisfied. \mathbf{F}^r is the net radial force on the swimmer, where the radial force per unit area \mathbf{f}^r is composed of stress components in \mathbf{y} and \mathbf{z} directions:

$$(2.9) \quad \mathbf{f}^r = (\sigma_{iy}n_i \cos(\theta) + \sigma_{iz}n_i \sin(\theta)) \hat{\mathbf{e}}_r$$

where $\theta = \text{atan2}(z_s, y_s)$, z_s and y_s denote \mathbf{z} - and \mathbf{y} - components of \mathbf{x}_s , Or n_i for $i = 1, 2, 3$ are the surface normals; and $\hat{\mathbf{e}}_r$ is the unit vector in the radial direction. Non-dimensional δ_w is set to $d/2 = 0.1$ which does not impose a significant restriction on the range of motion of the swimmer even for the narrowest channel tested here, as normalized clearance is $\delta_w/D_{ch} = 0.0625$.

The channel wall and the surface of the swimmer have no-slip boundary conditions. The swimmer moves with a velocity \mathbf{U} and rotates with an angular velocity $\boldsymbol{\omega} = [\omega_x \quad \omega_y \quad \omega_z]'$. Thus, the velocity of a point on the swimmer surface is given by:

$$(2.10) \quad \mathbf{U}_s = \mathbf{U} + \boldsymbol{\omega} \times (\mathbf{x}_s - \mathbf{x})$$

One end of the channel is the inlet without any inlet velocity, and the other end of the channel is defined as the outlet where the pressure is set to 0.

Trajectories of the swimmer are obtained from the kinematic relations:

$$(2.11) \quad \frac{d\mathbf{x}}{dt} = \mathbf{U}(\mathbf{x}, \mathbf{e}_i)$$

$$(2.12) \quad \frac{d\mathbf{e}_i}{dt} = \boldsymbol{\omega}(\mathbf{x}, \mathbf{e}_i) \times \mathbf{e}_i$$

\mathbf{e}_i for $i = 1, 2, 3$ represent the unit vectors of the local coordinate system placed at the center of mass of the swimmer, as shown in Fig. 2.1, and form the columns of the rotation matrix, which are used to calculate the Euler angles to fully define the swimmer orientation in the global channel coordinates. Since the inertial effects are negligible, acceleration of the swimmer is not considered. Linear and angular velocities are obtained from the solutions of the steady Stokes equation by the CFD model at each position and rotation, hence the velocities only depend on the position and the rotation of the swimmer represented by the unit vectors, \mathbf{e}_i .

Eqs. 2.11 and 2.12 can be used to obtain complete swimmer trajectories in Matlab. The position and orientation of the swimmer for the next time step are used as inputs in the next CFD simulation for the calculation of \mathbf{U} and $\boldsymbol{\omega}$ at that time step. Adams-Bashforth integration is used for the integration in Eq. 2.11. For initial time steps, forward Euler and two-step Adams-Bashforth formulations are employed. For Eq. 2.12, Crank-Nicholson formulation is utilized for the integration of the unit vectors of the body coordinates:

$$(2.13) \quad \mathbf{e}_i^{k+1} = \left(\mathbf{I} - \frac{\Delta t}{2} \mathbf{W}^k \right)^{-1} \left(\frac{\Delta t}{2} \mathbf{W}^k \right) \mathbf{e}_i^k$$

Here, superscript k denotes the current (resolved) time index, Δt is the time step, \mathbf{I} is the identity matrix and \mathbf{W} is the skew-symmetric matrix that represents the cross-product in Eq. 2.12. The proper selection of Δt is important as large Δt results in numerical instabilities. Small Δt , on the other hand, results in excessive computation times. For the simulations discussed in this paper, non-dimensional Δt ranges from 1/200 to 1/40. Depending on the channel size, convergence to a stable trajectory takes between 20 and 90 full rotations of the swimmer, corresponding to a few seconds of swimming in dimensional terms.

Commercial finite-element software Comsol Multiphysics is used to solve the Stokes equations numerically to obtain \mathbf{U} and $\boldsymbol{\omega}$ under the forces and torques given in Eqs. 2.2 and 2.3. Comsol is called within Matlab where the kinematic calculations are carried out, as outlined in Algorithm 1. The swimmer surface is meshed with free triangular elements, while a free tetrahedral mesh is preferred for the fluid domain and a single boundary layer is placed on the channel and swimmer surfaces. P1+P1 type elements with a total of 70000 degrees-of-freedom are used in the simulations with reasonable accuracy and computational time on a workstation with dual 6-core Intel Xeon CPUs clocked at 3.333 GHz and 94 GB of RAM. The results of the mesh convergence test are shown in Table 2.1 for the initial conditions in the base scenario (in pusher-mode), and parameters that are listed in Table 2.2 in bold typeface.

Algorithm 1 Psuedoc-code of the kinematic model

```

1: procedure INITIALIZE
2:    $\mathbf{x}^0$  and  $\mathbf{e}_i^0$ : Initial position and orientation of the swimmer
3:    $\mathbf{m}^0$ : Initial direction of the magnetization vector of the swimmer, which is
   set to  $\mathbf{e}_2^0$ 
4:    $k \leftarrow 0$ : Loop counter
5:   while  $t < t_{final}$  do
6:      $[\mathbf{U}^{k+1}, \boldsymbol{\omega}^{k+1}] = \text{CFD Model}(\mathbf{x}^k, \mathbf{e}_i^k, B_0, \omega_m, \mathbf{m}^k, t, \text{geometry values})$ 
7:     Integrate  $\mathbf{U}$  and  $\boldsymbol{\omega}$  to evaluate  $\mathbf{x}^{k+1}$  and  $\mathbf{e}_i^{k+1}$ 
8:      $k \leftarrow k + 1$ 
9:      $t \leftarrow t + \Delta t$ 
1: procedure CFD MODEL( $\mathbf{x}^k, \mathbf{e}_i^k, B_0, \omega_m, \mathbf{m}^k, t, \text{geometric parameters}$ )
2:   Build geometry for given geometric parameters, position,  $\mathbf{x}^k$ , and orientation
3:   Define physical parameters, boundary conditions
4:   Build the mesh
5:   Check contact
6:   Solve Eqs. 2.2 and 2.3, obtain and return  $\mathbf{U}$  and  $\boldsymbol{\omega}$ 

```

Table 2.1 Convergence test for the CFD model. The line in bold represents the meshing density used for the simulations.

Number of elements	Number of DOF	CPU Time [s]	Error in U_{sw} [%]	Error in V_{sw} [%]	Error in W_{sw} [%]
45830	44996	8	-4.14	-5.2	-13.7
75090	69784	11	-0.07	0.6	-2
172749	147584	21	-0.02	0.1	-0.3
306077	247213	43	-0.02	0.2	-0.1
520218	404733	97	-*	-*	-*
*Error is defined with respect to the results from the densest meshing.					

Table 2.2 Values of the geometric parameters tested. The values in bold typeface refer to base values, which are also used for the validation studies.

Parameter	Value(s)
Channel diameter, D_{ch}	1.6 , 3, 5, 20
Length of the tail, L	2, 4 , 8
Wavelength of the tail, λ_h	1
Wavelength of the tail along the helix centerline, Λ	2.71
Amplitude of the helical wave, A_h	0.4
Diameter of the tail, d	0.15, 0.2 , 0.25
Length of the head, L_{head}	1.5
Diameter of the cylindrical head, D_{head}	0.7, 0.8 , 0.9
Radius of curvature of curved edges, r_c	0.1
Contact condition parameter, δ_w	0.1

2.2 Verification of the CFD Model

The current CFD model was previously validated with experimental results in Aceoglu & Yesilyurt (2015) for a swimmer placed along the axis of the channel at various radial positions. Here, the model is used to calculate the linear and angular velocities of the swimmer subject to forces and torques for each radial position and rotation at each time step in the kinematic model. The axial position of the swimmer is calculated in the kinematic model but not updated in the CFD model assuming that the computational domain follows the swimmer in the axial direction. Dimensionless geometric parameters are listed in Table 2.2 with the values in bold representing the parameters used for the validation studies.

Trajectories from the kinematic model are compared with experimental results from Caldag et al. (2017) based on the non-dimensional radial position β , which is defined as:

$$(2.14) \quad \beta = \frac{r}{R_{ch} - R_{head}}$$

where r is the radial position of the center of mass of the swimmer and $R_{head} = D_{head}/2$. The angle between the axes of the swimmer and the channel is used as the pitching angle:

$$(2.15) \quad \theta_{ax} = \cos^{-1}(\mathbf{e}_1 \cdot \hat{\mathbf{x}})$$

where $\hat{\mathbf{x}}$ is the unit vector in the \mathbf{x} -direction, which also coincides with the axis of the channel and the rotation direction of the magnetic field, and \mathbf{e}_1 is the direction of the helical axis in the body coordinates of the swimmer. Normalized values of the pitching angle, $\bar{\theta}_{ax}$, are obtained by dividing the observed values of θ_{ax} to the maximum possible θ_{ax} for given L , D_{head} and D_{ch} in order to account for geometric restrictions:

$$(2.16) \quad \bar{\theta}_{ax} = \frac{\theta_{ax}}{\theta_{ax,max}(D_{ch}, D_{head}, L)}$$

Heading velocity is used to compare swimmer velocities in the puller and pusher modes and in the case of channel flow against the swimmer:

$$(2.17) \quad \hat{U}_{sw} = \text{sgn}(-\omega_m) U_{sw}$$

\hat{U}_{sw} is positive if the swimmer is moving in its desired swimming direction and it is negative when the swimmer is not able to swim in its desired swimming direction, e.g. if a strong flow in the channel drags the swimmer.

Figs. 2.2a and 2.2e show the trajectories in pusher and puller modes for swimmer L4 in the channel with $D_{head}/D_{ch} = 0.5$ from experiments and simulations at 15 Hz rotation rate. Trajectories from experiments and simulations are in good agreement for both modes of swimming: The pusher follows a helical trajectory close to the channel wall with a circular projection on the y - z plane (Fig. 2.2a), whereas the puller swims along the centerline of the channel (Fig. 2.2e). While there is a good agreement between the trajectories, average values of θ_{ax} and \hat{U}_{sw} are higher in the simulations than the experiments. Small differences between the geometric parameters as shown in Figs. 2.2i-j and irregularities in the shape of experimental swimmers may contribute to those differences. 3D-printed swimmers used in the

experiments have deviations from the idealized geometry due to the resolution of the 3D printing process. The sensitivity of results with respect to slight changes in D_{head} and d values are shown in Table 2.3. A thorough investigation of geometric parameters on swimming velocities is carried out in Acemoglu & Yesilyurt (2014).

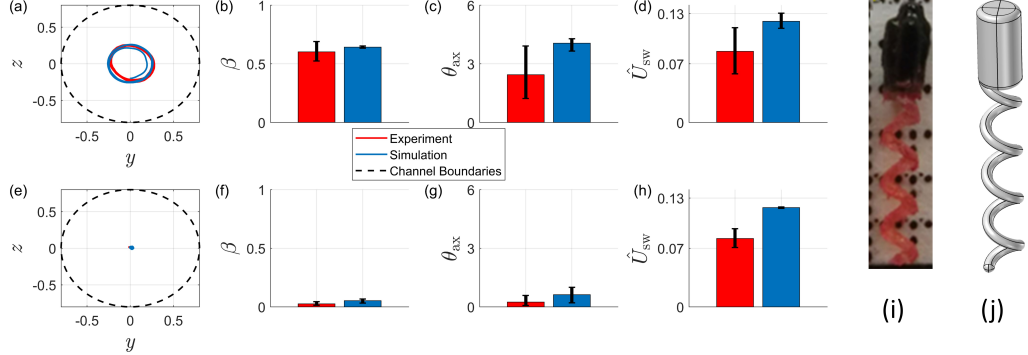


Figure 2.2 Comparison of simulation and experimental results for the pusher-mode ((a)-(d)) and the puller-mode ((e)-(h)) trajectories. (a) and (e) show the trajectories on the radial plane, (b) and (f) show average β with their variations, (c) and (g) show average θ_{ax} with their variations and (d) and (h) show average \hat{U}_{sw} with their variations. (i) shows the swimmer used in experiments and (j) is the idealization of this swimmer used in the simulations.

Table 2.3 The sensitivity of the results to variations in D_{head} and d for swimmer L4 with $D_{ch} = 1.6$ (pusher-mode). Values in bold correspond to the simulation whose results are shown at Fig. 2.2 (a)-(d).

D_{head}	β	θ_{ax} [°]	\hat{U}_{sw}	d	β	θ_{ax} [°]	\hat{U}_{sw}
0.7	0.67	4.77	0.11	0.15	0.70	4.53	0.13
0.8	0.64	4.24	0.12	0.2	0.64	4.24	0.12
0.9	0.61	3.65	0.12	0.25	0.58	3.79	0.10

2.3 Pusher-mode Instability

This section investigates how the pusher-mode instability occurs in the channel and the instability is characterized with respect to several key system parameters. Solution of the steady Stokes equations yields exactly symmetric linear and angular velocities with respect to the direction of the magnetic torque, $\boldsymbol{\tau}_m$, determined by the sign of the magnetic field, \mathbf{B} , i.e. $\mathbf{u}(\boldsymbol{\xi}, \boldsymbol{\chi}_i; \omega_m > 0) = -\mathbf{u}(\boldsymbol{\xi}, \boldsymbol{\chi}_i; \omega_m < 0)$ and $\boldsymbol{\omega}(\boldsymbol{\xi}, \boldsymbol{\chi}_i; \omega_m > 0) = -\boldsymbol{\omega}(\boldsymbol{\xi}, \boldsymbol{\chi}_i; \omega_m < 0)$ for a given position, $\mathbf{x} = \boldsymbol{\xi}$, and orientation, $\mathbf{e}_i = \boldsymbol{\chi}_i$ for ($i = 1, 2, 3$) of the swimmer in the absence of gravity and contact

forces that break the symmetry. Despite the symmetry of the velocities, their time-integration in opposite directions leads to different trajectories in the puller ($\omega_m < 0$) and pusher ($\omega_m > 0$) modes. To illustrate the irreversible nature of the trajectories, the pusher and puller-mode velocities obtained from the simulations with the same initial conditions are plotted in Figs. 2.3a-d where the velocities in the pusher-mode are multiplied with a (-) sign to compare them with the velocities of the puller-mode swimming. The insets in Figs. 2.3a-d show a zoomed-in view of the first few instances of the simulations. Gravity is excluded in these simulations and contact conditions are not met either, since the swimmer does not get too close to the wall. First few values of all velocities, shown in the insets, are very close (reversible), however, after a few steps, the swimmer velocities begin to diverge. Figs. 2.3a and 2.3c show that the simulations, the velocities in the \mathbf{y} - direction, V_{sw} and ω_y , for the pusher (reverted) and the puller are very close magnitude-wise for a while before they diverge completely as the puller converges towards a stable trajectory along the center-line of the channel. On the other hand, velocities in the \mathbf{z} - direction, W_{sw} and ω_z , have the opposite trends in Figs. 2.3b and 2.3d, however since the pusher is reverted their actual values are following each other closely before they diverge following the trajectories. Normalized radial positions of the trajectories are shown in Fig. 2.3e, whereas the projections of the trajectories on the yz -plane are shown in Figs. 2.3f and 2.3g. Since the pusher trajectory is reverted, the growing separation between the trajectories are clearly noticeable in the figures.

Man & Lauga (2013) investigated the wobbling angle of slender helices, the same as the pitching angle θ_{ax} in (2.15), using the resistance coefficients of the helix in bulk fluids, and found that θ_{ax} decreases with increasing Mason number (Ma), defined as:

$$(2.18) \quad \text{Ma} = \frac{\mu \Lambda_h^3 \omega_m}{|\mathbf{m}| B_0}$$

where μ is the fluid viscosity and Λ is the wavelength along the helix centerline ($\Lambda = \lambda_h / \cos(\theta_h)$ and $\theta_h = \tan^{-1}(\pi D / \lambda_h)$). The authors report that rigid slender helices wobble in bulk fluids at low Mason numbers which are realized by low rotation frequencies or strong magnetic fields.

In order to distinguish the pusher-mode instability from the wobbling of helices, simulations are conducted for near-bulk swimming conditions by setting the channel diameter 25 times as much as the diameter of the head, i.e. $D_{head}/D_{ch} = 0.04$. In this case, the pusher-mode swimmer still follows a helical trajectory but with a very small

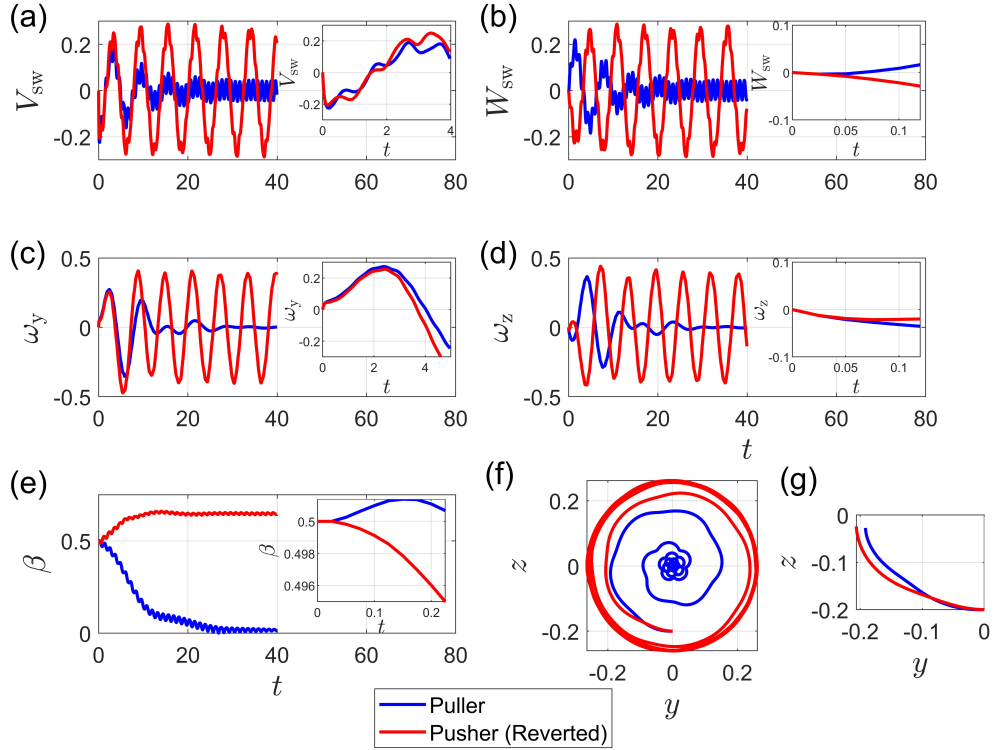


Figure 2.3 Comparisons of the trajectories for the pusher and puller-mode swimming with the same initial conditions. (a) and (b) show the linear velocities in \mathbf{y} - and \mathbf{z} - directions, respectively and (c) and (d) show the angular velocities in these directions. (e) shows the change of β in both modes. The insets in (a)-(e) show the initial part of the simulations to demonstrate the breakdown of the symmetry. (f) shows the radial trajectories of the pusher and puller-mode swimmers where the pusher-mode trajectory is mirrored in the \mathbf{y} -direction to better show the separation of the trajectories. (g) shows a zoomed-in version of the first few instances of (f).

pitching angle, θ_{ax} , which converges to 0.55° . For the swimmer without the head, θ_{ax} increases slightly to 1.9° , indicating that the head improves the alignment of the swimmer with the direction of rotation of the magnetic field. The wobbling angle of the tail-only swimmer is calculated as 0.97° from the model that uses the resistance coefficients developed by Man & Lauga (2013), indicating that the hydrodynamic interactions between the helical turns of the tail increase the wobbling. Moreover, when the confinement ratio is set to $D_{head}/D_{ch} = 0.26$, θ_{ax} increases up to 8.38° for the complete swimmer (values are listed in Table 2.4 for comparison). In principle, θ_{ax} increases with in-creasing viscous resistance in narrower channels, therefore the wobbling angle of helices is expected to decrease according to the model developed by Man & Lauga (2013), however, the trajectories from the simulations show that the pitching angle, θ_{ax} , the angle between the helical axis of the swimmer and the rotation direction of the magnetic field, increases instead. Since the simulations are

based on full numerical solutions of the Stokes equations, hydrodynamic interactions are taken into account completely. Therefore, this is a significant result that shows the hydrodynamic interactions between the helical swimmer and the channel wall does not reduce but increase the pitching or the wobbling angle.

Table 2.4 θ_{ax} values for several different swimmers and swimming conditions.

Simulation Case, $Ma = 0.7$	θ_{ax} [°]
Tail Only (near bulk, $2A_h/D_{ch} = 0.04$)	1.9
Full Swimmer (near bulk, $D_{head}/D_{ch} = 0.04$)	0.55
Full Swimmer (confined, $D_{head}/D_{ch} = 0.26$)	8.38
Slender Tail (bulk) (Man & Lauga 2013)	0.97

In order to improve the understanding of helical swimming in confined environments, the effects of the Ma number are investigated further. First, Ma in Eq. 2.18, which is defined for bulk-swimming conditions, is replaced with a confinement Mason number, Ma_c , to include increasing viscous effects due to confinement:

$$(2.19) \quad Ma_c = \kappa Ma$$

where κ is a scaling factor that addresses increased viscous resistance due to the confinement and calculated from the ratio of average viscous torques (during one complete rotation) in confined and bulk swimming conditions:

$$(2.20) \quad \kappa = \frac{\tau^{v,confined}}{\tau^{v,bulk}}$$

$\tau^{v,confined}$ is the average viscous torque for a confined swimmer at a given radial position β and $\tau^{v,bulk}$ is the viscous torque evaluated from near-bulk swimming conditions ($D_{head}/D_{ch} = 0.04$). $\tau^{v,confined}$ is evaluated at the converged β values of the swimmer trajectories. Overall κ ranges from 1 to 1.4 for swimmer L4.

Fig. 2.4 shows the average trajectory parameters β , θ_{ax} , $\bar{\theta}_{ax}$ and \hat{U}_{sw} with respect to Ma_c ranging between about 0.1 and 1 in channels with different diameters for swimmer L4 in the pusher and puller modes. It is difficult to reduce the Ma_c further (i.e., $Ma_c < 0.01$) as increasing the magnetic torque or decreasing the viscous torque requires very small time-steps, $\Delta t \approx 10^{-3}$, in simulations so that one of them needs to run more than a week on a high-end workstation. The swimmers are placed sufficiently away from the channel wall and aligned with the centerline initially. $\bar{\theta}_{ax}$

values for pullers are not provided as they are very low and do not contribute to the discussion.

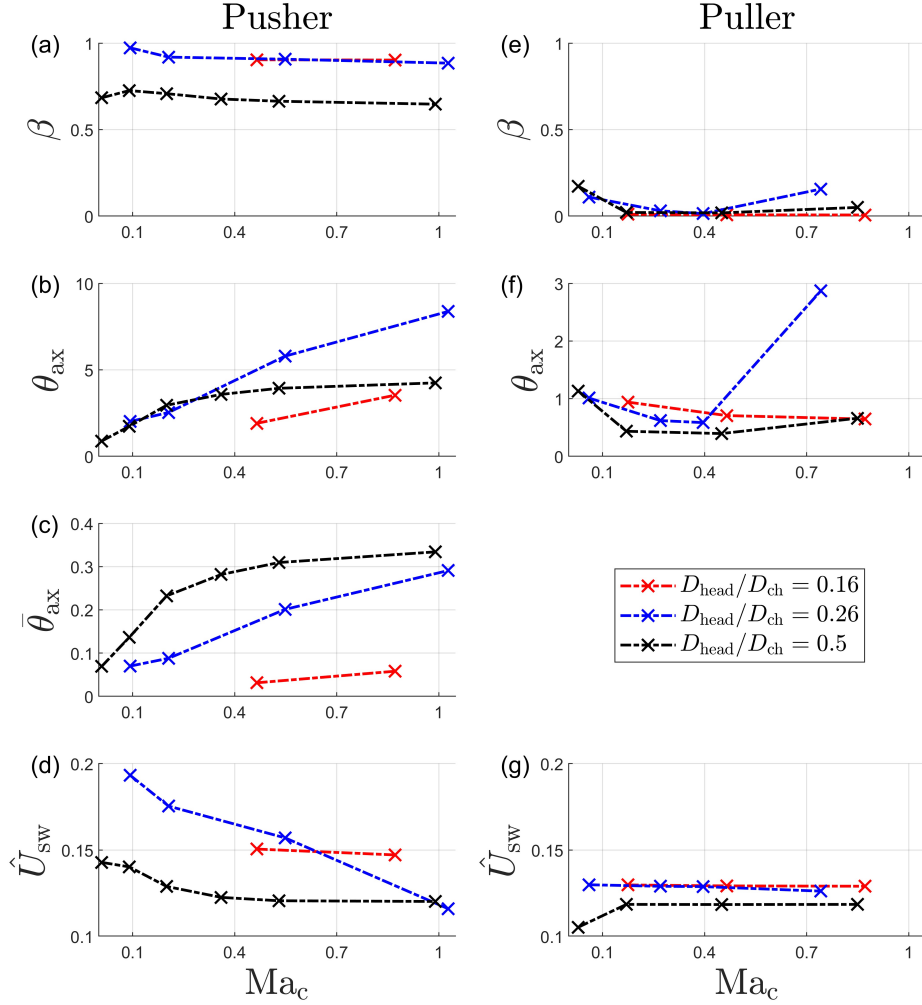


Figure 2.4 The effects of the Ma_c on the stable time-averaged trajectory parameters for (a)-(d) the pusher-mode and (e)-(g) the puller mode.

For pushers, high Ma_c leads to a slight decrease in β and considerable slowdown in the heading velocity, \hat{U}_{sw} (Figs. 2.4a and 2.4d). As the pitching angle of the swimmer increases with increasing Ma_c , \hat{U}_{sw} tends to decrease as well. The dramatic decrease in \hat{U}_{sw} for $D_{head}/D_{ch} = 0.26$ with respect to Ma_c is noticeable in Fig. 2.4d. The decrease in β , which corresponds to a higher absolute change in r , and the increase in θ_{ax} are responsible for the decrease in \hat{U}_{sw} . It is understandable that the swimming velocity decreases as the alignment of the swimmer with the channel axis is impaired.

For pushers, θ_{ax} is very small at low Ma_c and comparable to the values observed in the puller-mode as shown in Fig. 2.4b. Low θ_{ax} values are expected at low Ma_c as the increasing magnetic torque overcomes the viscous torque in all directions and aligns the swimmer with the channel's axis. When the magnetic field is turned on in the experiments, the swimmer is aligned with the axis of the channel immediately, indicating that the magnetic torque helps the alignment of the swimmer. However, as the strength of the magnetic field is increased further, the wobbling is observed at very low Ma numbers ($10^{-4} - 10^{-3}$) according to Man & Lauga (2013). In this study, Ma_c values are larger than 0.01 due to limitations in computational time. Thus, θ_{ax} is expected to increase again at much lower Ma_c values for both the puller and pusher modes, due to the wobbling of the helix at lower frequencies or higher magnetic torques, as evidenced by the slight increase of θ_{ax} values at low Ma_c in the puller-mode swimming. This trend is visible in the puller-mode only as they are close to the center of the channel where the interactions with the boundaries are minimal and θ_{ax} values are already low. The trend implies that there is an optimal Ma_c number for each configuration that minimizes θ_{ax} . In accordance with θ_{ax} values in the puller-mode, β values follow similar trends. The effect of confinement on θ_{ax} is not monotonic as shown in Fig. 2.4b, but when normalized by its geometrically possible maximum value, $\bar{\theta}_{ax}$, which is given by 2.16, increasing the confinement is seen to deteriorate the alignment.

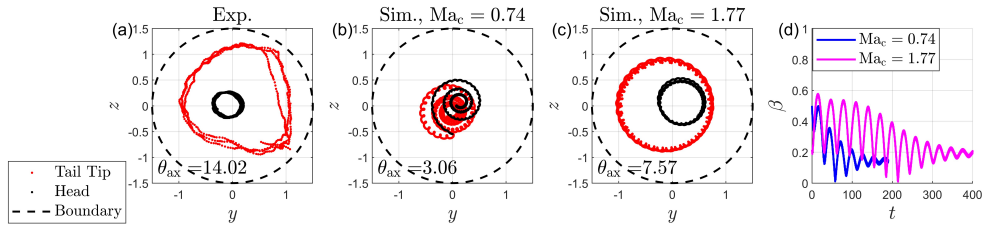


Figure 2.5 Wobbling of a puller at high Ma_c inside a channel with $D_{head}/D_{ch} = 0.26$. a) Positions of the head and tail tip in the experiment from Caldag et al. (2017), b) positions of the head and tail tip in simulations for $\text{Ma}_c = 0.74$ and c) for $\text{Ma}_c = 1.77$. θ_{ax} values at (a)-(c) are the averages for given parts of the trajectories. d) Change of β in extended simulations for $\text{Ma}_c = 0.74$ and $\text{Ma}_c = 1.77$, showing that the swimmer converges towards a stable trajectory but at a longer time compared to the experiments. Note that the trajectories at b) and c) are representative of a few rotations of the swimmer and do not show the complete trajectories at (d).

Lastly, there is a sharp increase in θ_{ax} in the puller-mode swimming $D_{head}/D_{ch} = 0.26$ as shown in Fig. 2.5f. When the Ma_c is increased further to 1.77 for this case, the swimmer exhibits wobbling behavior where the tip of the tail makes a wider circle than the center of mass which is located in the head as shown in Fig. 2.5c, with a θ_{ax} value of 7.57° . This behavior is consistent with experiments reported in our previous work where we observed θ_{ax} going up to 14.02° , with the trajectory shown at Fig.

2.5a. (Caldag et al., 2017). According to simulation results for the full trajectory, this case corresponds to near step-out condition; even though the swimmer's angular velocity is very close to the angular velocity of the rotating magnetic field, it has the largest oscillations compared to other cases, indicating that the magnetic torque barely overcomes the viscous torque. Moreover, the convergence of the trajectory was not clear in the experiments; the trajectory indeed converges to a small β range although it takes very long according to simulations (Fig. 2.5d).

The findings in this chapter give an insight about the oscillatory trajectories of helical trajectories under confinement. Based on the problem characterized in this chapter, the following chapter will present a feedback control law that successfully suppresses the pusher-mode instability and enable controlled navigation.

3. Magnetic Manipulation of Magnetized Helical Swimmers

Pusher-mode instability may pose certain risks in biomedical applications where accurate navigation is crucial. Suppressing the oscillatory trajectories is a critical step in enabling controlled navigation of these swimmers. The oscillatory trajectories can be suppressed by utilizing a magnetic steering algorithm. The novelty of the algorithm presented here is that it does not require swimmer orientation to be known. Considering the biomedical application scenarios, obtaining proper swimmer orientation is not feasible at all. Thus, the approach proposed here has more practical relevance than the state-of-the-art while still providing comparable performance.

3.1 Swimmer Kinematics and Control Law

The swimmer is taken inside a circular channel filled with a viscous fluid. The swimmer has a cylindrical head with a length of L_{head} and diameter D_{head} . The pitch of the helical tail is λ_h , total tail length is L , the major diameter of the tail is D , the number of rotations is N_h , filament thickness is d and the channel diameter is D_{ch} .

Control of helical microswimmers is approached as a path following problem as opposed to a trajectory following problem since the swimming velocity is limited by phenomena such as step-out at high rotation frequencies and wobbling at low rotation frequencies. The problem will be treated as a radial path following problem as the axial position will be adjusted by rotating the swimmer fast or slowly. The

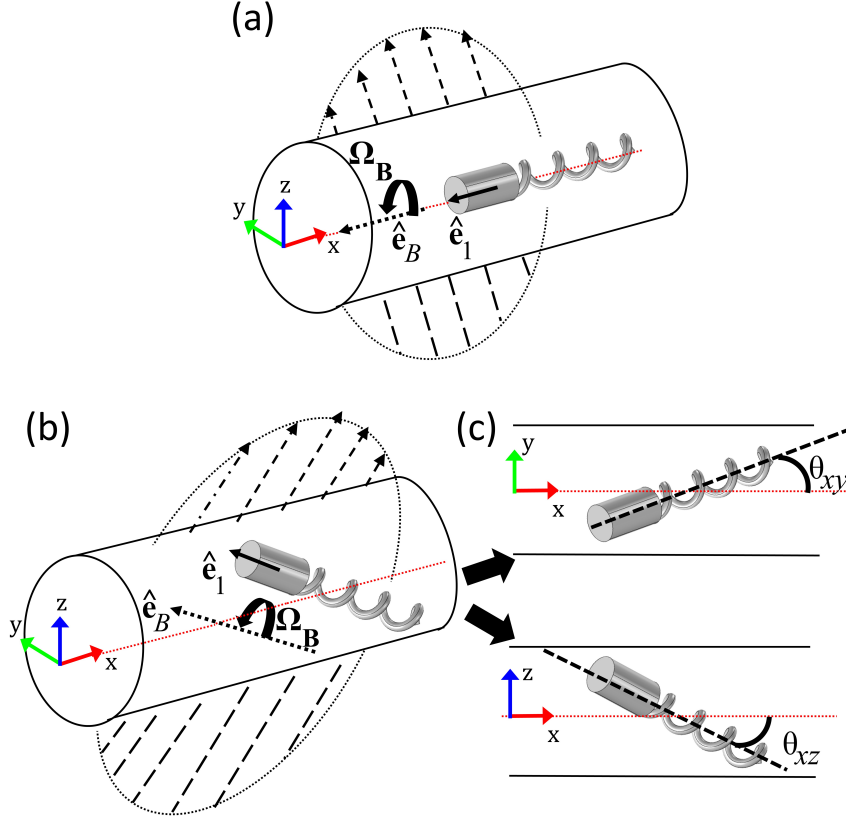


Figure 3.1 (a) The geometric setup, showing the channel, the swimmer, rotating magnetic field, field normal and propulsion direction. (b) Steering of the swimmer through tilting the normal of the magnetic field. (c) Representation of angles θ_{xy} and θ_{xz} .

rotating magnetic field actuates the swimmer by imposing a magnetic torque on the swimmer:

$$(3.1) \quad \tau_{loc}^m = \mathbf{m} \times \mathbf{Q}_l \mathbf{B}$$

where \mathbf{Q}_l is the rotation matrix from the lab frame (shown at Figure 1a) to body frame of the swimmer and \mathbf{B} is the total magnetic field in the lab frame. The subscript *loc* indicates that the term is expressed in the local coordinate frame whose origin is placed at the center-of-mass of the swimmer. The driving magnetic field for propulsion, \mathbf{B}_{drive} , is generally provided by a pair of orthogonal Helmholtz coils and expressed as in Eq. 5.6. According to the resistive force theory (RFT)

(Man & Lauga, 2013), viscous forces and torques (\mathbf{F}^v and $\boldsymbol{\tau}^v$) on the swimmer are proportional to linear and angular velocities (\mathbf{U} and $\boldsymbol{\omega}$) at low Reynolds number:

$$(3.2) \quad \begin{bmatrix} \mathbf{F}^v \\ \boldsymbol{\tau}^v \end{bmatrix} = \begin{bmatrix} \mathbf{R}_L & \mathbf{R}_C \\ \mathbf{R}'_C & \mathbf{R}_R \end{bmatrix} \begin{bmatrix} \mathbf{U} \\ \boldsymbol{\omega} \end{bmatrix}$$

where \mathbf{R}_L , \mathbf{R}_R and \mathbf{R}_C are called the translation, rotation and coupling matrices. The elements of the matrices depend only on the swimmer geometry in bulk swimming conditions and can be evaluated analytically for slender filaments. In the case of hydrodynamic interactions, such as near-wall swimming, the elements of the resistance matrix depend on the relative position and orientation of the swimmer with respect to solid boundaries.

The objective of the control problem is to minimize the distance between the swimmer position $\mathbf{x} = [x \ y \ z]'$ and a reference path $\mathbf{p}_{ref} = [x \ y_{ref} \ z_{ref}]'$, meaning that no control in \mathbf{x} - direction is applied. The reference path is taken constant, i.e. $y_{ref} = z_{ref} = 0$, to prove the stability of the algorithm.

The state vector is defined as $\mathbf{q} = [e_y \ e_z]'$ where $e_y = y - y_{ref}$ and $e_z = z - z_{ref}$, and its time derivatives as:

$$(3.3) \quad \dot{\mathbf{q}} = \begin{bmatrix} \dot{y} - \dot{y}_{ref} \\ \dot{z} - \dot{z}_{ref} \end{bmatrix} = \begin{bmatrix} \dot{y} \\ \dot{z} \end{bmatrix}$$

These velocities depend on the orientation of the swimmer, represented by the angles θ_{xy} and θ_{xz} (refer to Figure 3.1c). The steering directly adjusts these angles and thus changes the propulsion direction. Orientation angles can be manipulated by the magnetic field \mathbf{B} . The unit normal of the rotation plane of the magnetic field, $\hat{\mathbf{e}}_B$, points in $-\mathbf{x}$ direction without steering, as shown at Figure 3.1a. In the ideal case, the swimmer aligns its orientation in the propulsion direction, $\hat{\mathbf{e}}_1$, along $\hat{\mathbf{e}}_B$ and propels in this direction only such that the swimming velocity can be written as $\mathbf{U} = |\mathbf{U}|\hat{\mathbf{e}}_1$. However, helical swimmers wobble both in free and confined swimming conditions (Caldag et al., 2017; Man & Lauga, 2013). The behavior is inherent to the swimmer geometry and it is characterized with the Mason number (Ma), which is the ratio of hydrodynamic to magnetic torques. Due to the periodic nature of

wobbling, it can be said that $\hat{\mathbf{e}}_1$ remains along $\hat{\mathbf{e}}_B$ in average. Thus, we can rewrite Eq. 3.3 in the following form to include the control inputs:

$$(3.4) \quad \dot{\mathbf{q}} = \begin{bmatrix} \dot{y} \\ \dot{z} \end{bmatrix} = \begin{bmatrix} U \tan(\theta_{xy}) \\ U \tan(\theta_{xz}) \end{bmatrix}$$

where U is the velocity in the \mathbf{x} - direction in the lab frame. Apparently, $\tan(\cdot)$ brings non-linearity to the system, but the term can be approximated as θ with error in approximation as low as 5% up to 20° . It was shown in Caldag et al. (2017) that the orientation angles barely reach around 20° when $D_{ch} = 3$ mm, $\lambda_h = 1$ mm and $N_h = 4$ so this approximation is valid for in-channel experiments reported here. This linearization brings:

$$(3.5) \quad \dot{\mathbf{q}} = \begin{bmatrix} \dot{y} \\ \dot{z} \end{bmatrix} = \begin{bmatrix} U\theta_{xy} \\ U\theta_{xz} \end{bmatrix}$$

To drive the error to zero, error dynamics must satisfy:

$$(3.6) \quad \dot{\mathbf{q}} + \begin{bmatrix} K_y & K_z \end{bmatrix} \mathbf{q} = 0$$

for positive gains, $K_{\{y,z\}} > 0$. Then according to Eq. 3.5, we have:

$$(3.7) \quad U\theta_{x\{y,z\}} + K_{\{y,z\}} + e_{\{y,z\}}$$

Thus, the control inputs are:

$$(3.8) \quad \theta_{x\{y,z\}} = \frac{-K_{\{y,z\}} + e_{\{y,z\}}}{U}$$

Steering is realized through an additional magnetic field, $\mathbf{B}_{control}$. Defining $\mathbf{B}(\omega t) = \mathbf{B}_{drive} + \mathbf{B}_{control}$, the control input is as following:

$$(3.9) \quad \mathbf{B}_{control} = B_0 [a_c \cos(\omega_m t) + b_c \sin(\omega_m t) \quad 0 \quad 0]'$$

with coefficients a_c and b_c . $\hat{\mathbf{e}}_B$ for the tilted magnetic field can be evaluated from the cross product of a pair of orthogonal magnetic field vectors:

$$(3.10) \quad \hat{\mathbf{e}}_B = \frac{\mathbf{B}(0) \times \mathbf{B}(\pi/2)}{\|\mathbf{B}(0) \times \mathbf{B}(\pi/2)\|} = \frac{[1 \quad -b_c \quad -a_c]'}{\sqrt{1 + a_c^2 + b_c^2}}$$

If $b_c=0$ and $a_c \neq 0$, $\hat{\mathbf{e}}_B$ is tilted in \mathbf{z} - direction only, as demonstrated at Figure 3.1b. For a non-zero a_c , $\hat{\mathbf{e}}_B$ will be tilted in the \mathbf{y} - direction as well. The magnitudes of the coefficients will adjust the scaling. This mechanism can be combined with a simple feedback controller to move the swimmer towards \mathbf{p}_{ref} :

$$(3.11) \quad \mathbf{B}_{control} = \mathbf{K}_p(\mathbf{x} - \mathbf{p}_{ref})$$

where \mathbf{K} is a 3x3 matrix that contains the proportional gains and time-dependent parts of the magnetic field. In this configuration, matrix \mathbf{K}_p will have the following form:

$$(3.12) \quad \mathbf{K}_p = \begin{bmatrix} 0 & K_{p,y} \cos(\omega_m t) & K_{p,z} \sin(\omega_m t) \\ 0 & 0 & 0 \\ 0 & 0 & 0 \end{bmatrix}$$

Therefore, the coefficients a_c and b_c in Eq. 3.9 can be expressed in terms of the position error and the gains, $K_{p,y}$ and $K_{p,z}$ as follows:

$$(3.13) \quad a_c = K_{p,y} e_y \quad b_c = -K_{p,z} e_z$$

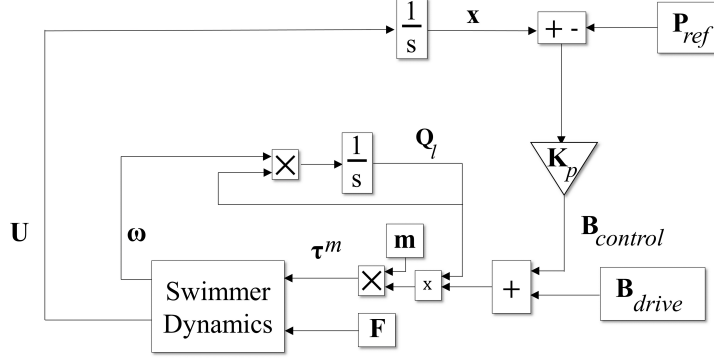


Figure 3.2 Block diagram of the swimmer kinematics and control.

The relation between tilting and the control input is:

$$(3.14) \quad \theta_{xy} = \arctan(-b_c) \quad \theta_{xz} = \arctan(-a_c)$$

Rewriting (12), we obtain:

$$(3.15) \quad \theta_{xy} = \arctan(-K_{p,y}e_y) = \frac{K_y e_y}{U}$$

Based on the $\tan(\theta) \approx \theta$ assumption, the relation between $K_{p\{y,z\}}$ and $K_{\{y,z\}}$ come out as:

$$(3.16) \quad K_{p,y} = \frac{K_y}{U} \quad K_{p,z} = \frac{K_z}{U}$$

Overall dynamics of the swimmer and control mechanism are drawn as a block diagram in Figure 3.2. The swimmer is continually tilted towards the reference path with no knowledge of swimmer orientation. This is advantageous especially considering the potential in vivo applications where even obtaining accurate swimmer position information is challenging.

For stability analysis, we define a Lyapunov function, V , as:

$$(3.17) \quad V = \frac{1}{2} (e_y^2 + e_z^2)$$

It is obvious that $V = 0$ for $\{e_y, e_z\} = \{0, 0\}$ and $V > 0$ for all $\{e_y, e_z\} - \{0, 0\}$. If we take the time derivative, assuming that y_{ref} and z_{ref} are constant in time:

$$(3.18) \quad \dot{V} = e_y \dot{y} + e_z \dot{z}$$

Here, the velocities \dot{y} and \dot{z} are the control inputs set via $\mathbf{B}_{control}$. In order to satisfy $\dot{V} < 0$ for all $\{e_y, e_z\} - \{0, 0\}$, \dot{y} and \dot{z} should have opposite signs with e_y and e_z , respectively. In other words, the swimmer should be tilted upward when it is below the reference path and vice versa. The definitions of a_c and b_c in Eq. 3.13 alongside their effects on $\hat{\mathbf{e}}_1$ show that this is always the case. Since all Lyapunov stability conditions are satisfied, $\{e_y, e_z\} = \{0, 0\}$ is a stable equilibrium point. This control approach is used to bring the swimmer to the center of the channel centerline. With further feedback from horizontal position information, the swimmer can be steered back or forth to exactly reach the desired Cartesian coordinates.

Even though the proportional control is sufficient in most of the cases tested, (refer to Section 3.4), integral and derivative control are incorporated in the experimental setup to see whether there would be any improvement in the performance. Additional terms are introduced to Eq. 3.11 as the following:

$$(3.19) \quad \mathbf{B}_{control} = \mathbf{K}_p (\mathbf{x} - \mathbf{p}_{ref}) + \mathbf{K}_i \int_0^t (\mathbf{x} - \mathbf{p}_{ref}) dt + \mathbf{K}_d \frac{d(\mathbf{x} - \mathbf{p}_{ref})}{dt}$$

Integral evaluation is carried out by trapezoidal method while the derivative of the error is approximated with a Savitzky-Golay filter that uses 10 previous datapoints. Matrices \mathbf{K}_i and \mathbf{K}_d have a form similar to \mathbf{K}_p in Eq. 3.12 with the gains $K_{i\{y,z\}}$ and $K_{d\{y,z\}}$.

3.2 Resistive Force Theory-Based Modelling of Helical Swimming

Magnetized helical swimmers swim in a low Reynolds number environment, meaning that the forces and torques acting on the swimmer act instantaneously as the inertial effects are negligible. For this model, we assume the swimmer as a helical tail only,

without the head, as shown at Fig. 4.1. The swimming is governed by Eq. (2.8), with the resistance matrix relating the velocities to forces and torques exerted to the swimmer. Within the context of magnetically actuated helical swimmers, Eq. 3.2 boils down to:

$$(3.20) \quad \begin{bmatrix} \mathbf{0} \\ \boldsymbol{\tau}^m \end{bmatrix} = \begin{bmatrix} \mathbf{R}_L & \mathbf{R}_C \\ \mathbf{R}'_C & \mathbf{R}_R \end{bmatrix} \begin{bmatrix} \mathbf{U} \\ \boldsymbol{\Omega} \end{bmatrix}$$

where $\boldsymbol{\tau}^m$ is as defined in Eq. 3.1. The resistance matrix of a helix is calculated by Man & Lauga (2013) in non-dimensional terms. Here, an equivalent but simpler form of the matrix is used. First, we define several parameters:

$$(3.21) \quad k_h = \frac{2\pi}{\lambda_h}, \quad C = \frac{c_t N_h}{\sqrt{1 + k_h^2 D^2}}$$

$$(3.22) \quad \begin{aligned} A_1 &= -\frac{C}{\lambda_h}, & A_2 &= 3\pi^2 D^2, & A_3 &= A_2 + \lambda_h^2 \\ A_4 &= k_h^2 D^4 + \frac{2}{3} A_2 N_h^2 - \frac{1}{4} D^2 + \frac{2}{3} \lambda_h^2 N_h^2 \\ A_5 &= k_h^2 D^4 + \frac{2}{3} A_2 N_h^2 - \frac{5}{4} D^2 + \frac{2}{3} \lambda_h^2 + N_h^2 \end{aligned}$$

where c_t , the tangential resistive coefficient is given by:

$$(3.23) \quad c_t = \frac{2\pi\mu}{\log\left(\frac{2\lambda_h}{d}\right) - 0.5}$$

Note that the normal component, $c_n = 2c_t$. The components of the resistance matrix come out as following:

$$(3.24) \quad \mathbf{R}_L = A_1 \begin{bmatrix} 2A_3 & 0 & 0 \\ 0 & 2A_3 & 0 \\ 0 & 0 & \frac{8}{3}A_2 + \lambda_h^2 \end{bmatrix}$$

$$(3.25) \quad \mathbf{R}_C = A_1 \begin{bmatrix} \frac{\lambda_h A_2}{2\pi} & N_h \lambda_h A_3 & 0 \\ -N_h \lambda_h A_3 & \frac{\lambda_h A_2}{6\pi} & 0 \\ 0 & -\lambda_h^2 D & -2\pi \lambda_h D^2 \end{bmatrix}$$

$$(3.26) \quad \mathbf{R}_R = A_1 \lambda_h^2 \begin{bmatrix} A_4 & \frac{N_h A_2}{6} & 0 \\ \frac{N_h A_2}{6} & A_5 & \frac{D}{\pi \lambda_h} (\frac{2}{3} A_2 + \lambda_h^2) \\ 0 & \frac{D}{\pi \lambda_h^2} (\frac{2}{3} A_2 + \lambda_h^2) & \frac{2D}{\lambda_h} (\frac{2}{3} A_2 + \lambda_h^2) \end{bmatrix}$$

The model as is simulates swimming in bulk fluid. When a helical swimmer swims in confined environment, it generates a swirling flow. A forced vortex through a swirl flow with angular velocity Γ can be introduced to mimic the swimming inside a circular channel. The tangential velocity is decomposed into:

$$(3.27) \quad U_{f,y} = -\Gamma z$$

$$(3.28) \quad U_{f,z} = \Gamma y$$

Drag forces due to these additional velocities are added in 3.2. Note that these velocities are in the lab frame, thus the additional drag forces should be evaluated locally and summed up. In order to do that, the velocities have to be expressed in the local coordinate frame. Defining s as the curvilinear coordinate index that represents the tail, \mathbf{U}_f in the body frame at position s is:

$$(3.29) \quad \mathbf{U}_f^b = \mathbf{Q}_l \mathbf{W}_g (\mathbf{Q}'_l \mathbf{x}_l + \mathbf{x})$$

where \mathbf{x}_l represents the coordinates of a local position on the helical tail in body coordinates as a function of s and \mathbf{W}_g represents the multiplications in Eqs. 3.27 and 3.28 with $\mathbf{W}_g(2,3) = -\Gamma$, $\mathbf{W}_g(3,2) = \Gamma$ and the rest are zeroes. The normal

and tangential components of the differential force due to swirl are then evaluated as:

$$(3.30) \quad d\mathbf{F}_{sw,t} = c_t (\mathbf{U}_f^b \cdot \hat{\mathbf{t}}) \hat{\mathbf{t}}$$

$$(3.31) \quad d\mathbf{F}_{sw,n} = c_n (\mathbf{U}_f^b - \mathbf{U}_f^b \cdot \hat{\mathbf{t}}) \hat{\mathbf{t}}$$

where $\hat{\mathbf{t}}$ is the unit vector in tangential direction on the helical tail, the superscript "b" indicates the body frame of the swimmer. The swirling flow model is used in the RFT model at Section 3.4.

Trajectory of the swimmer is obtained from the kinematic relations:

$$(3.32) \quad \frac{d\mathbf{x}}{dt} = \mathbf{U}$$

$$(3.33) \quad \frac{d\mathbf{e}_i}{dt} = \boldsymbol{\omega} \times \mathbf{e}_i$$

for $i = 1, 2, 3$. The \mathbf{e}_i represent the local coordinate axes and form the columns of the rotation matrix, which are used to calculate the Euler angles to fully define the swimmer orientation in the global channel frame. Linear and angular velocities obtained from Eq. 3.20 are incorporated into Eqs. 3.32 and 3.33 to compute the complete trajectory of the swimmer. Adams-Bashforth integration is used for the integration of Eq. 3.32. The integration of unit vectors in Eq. 3.33 are carried out by the Crank-Nicholson formulation.

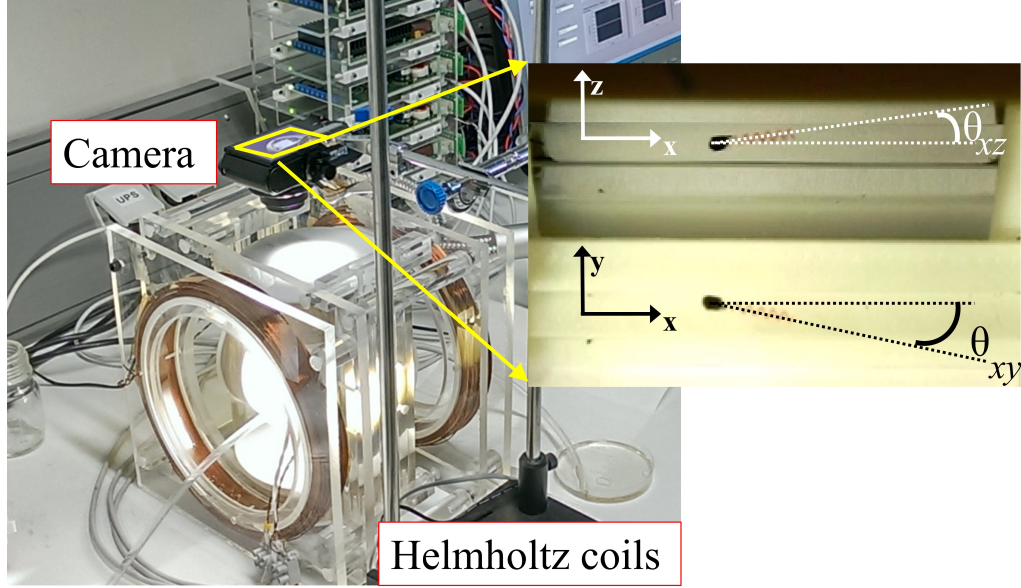


Figure 3.3 Experimental setup showing the Helmholtz coils, digital camera and computer. An image captured from experiment recordings; coordinate axes and angles θ_{xy} and θ_{xz} are shown at the right-hand side.

3.3 Experiment Setup

The experiment setup consists of 3 pairs of orthogonally placed Helmholtz coils, as shown in Fig. 3.3. The magnetic field magnitude B_0 for a coil with N_c number of windings at I Amperes of current is given by:

$$(3.34) \quad B_0 = 0.8^{1.5} \frac{\mu_0 N_c I}{R_{he}}$$

where μ_0 is the permeability of the vacuum and R_{he} is the radius of the Helmholtz coil, which should be equal to the half of the distance between the coil pairs. The coils are driven by Maxon ADS E50/5 drivers which are controlled from a computer via National Instruments SCB-68 data acquisition device. Matlab's Data Acquisition Toolbox is used to send the desired current to the coils.

The helical microswimmer is produced with 3D printing and it is magnetized by attaching a radially magnetized cylindrical magnet to its head. The swimmer is placed inside a glycerol-filled cylindrical channel for low Reynolds number swimming. Geometric properties of the swimmer are listed in Table 3.1. Swimmer position is extracted from the images recorded in real-time with a digital camera placed above

Table 3.1 Geometric parameters of the 3D-printed swimmer used in the experiments.

Geometric Parameter	Value
D_{head} [mm]	0.8
L_{head} [mm]	1.5
L [mm]	4
λ_h [mm]	1
d [mm]	0.2

the setup. A mirror is placed next to the channel with 45-degree inclination and allows the extraction of 3D position information using Matlab’s Image Processing Toolbox (see Fig. 3). Further details of the experiment setup can be found in Caldag et al. (2017).

3.4 Verification of Steering Control Algorithm

Stabilizing the pusher-mode swimming in channels is a challenging and important task as the swimmers follow helical trajectories and crash into the walls occasionally. Steering control is verified by suppressing helical trajectories in the pusher-mode swimming. The algorithm is first tested in the RFT-based model presented in Section 3.2. The swimmer geometry is as defined in Man & Lauga (2013) with $n = 3$ according to their notation. Initial position is set to $\mathbf{x}^0 = [0 \ 1 \ 1]'$ and $\mathbf{p}_{ref} = [x \ 0 \ 0]'$. In accordance with the calculations from our previous simulations for a confined swimmer, the Mason number, Ma , is set to 1 (Caldag & Yesilyurt, 2019); the Mason number is defined as in Eq. 2.18. Swirling flow is the main cause of the helical trajectory of the swimmer. The strength of the forced vortex, Γ , is taken as $\pi/10$ such that it is significantly lower than the non-dimensional rotation rate of the magnetic field, 2π , similar to the observed swirl rate in experiments. Trajectories under different control gains are displayed in Fig. 3.4. Control algorithm significantly suppresses the helical path as the radius of the trajectory falls from around 5 mm to 0.27 mm and to 0.05 mm for the highest gain value tested. Note that this improvement increases propulsion velocity as well, from 0.08 mm/s without control to 0.35 mm/s and to 0.36 mm/s with the control in the loop. The control algorithm performs well in the kinematic model too where the complete Stokes equations are solved. Here, $D_{ch} = 3$ mm and control gains are set to unity. Fig. 3.5a shows that the trajectory radius decreases from around 0.71 mm to 0.05 mm, which is the threshold value for the algorithm to stop steering. As the change

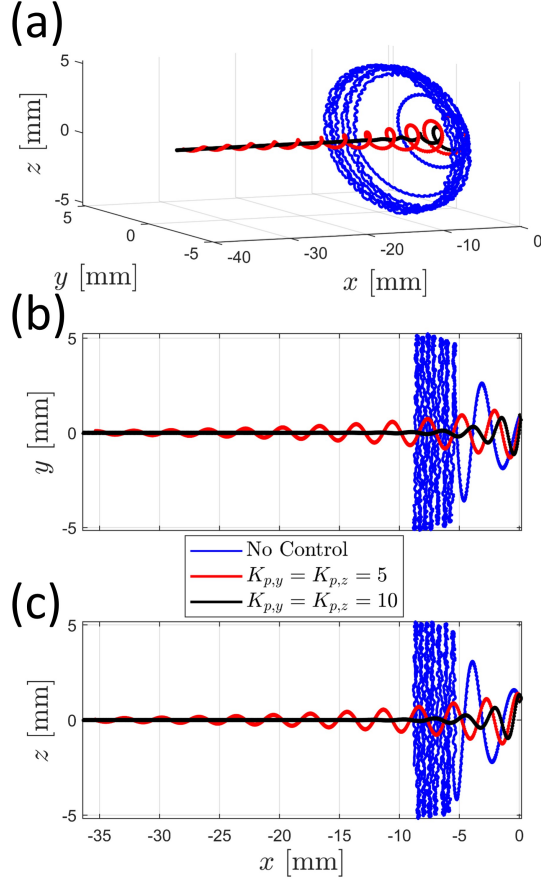


Figure 3.4 Swimmer trajectories in the numerical model with and without control. (a) shows the 3D trajectories while (b) shows y vs. x and (c) shows z vs. x .

in the trajectory radius is much lower compared to the unbounded swimmer in the numerical model, the improvement in the propulsion velocity is negligible here. It is also possible to make the swimmer follow time-varying paths with this algorithm as shown at Figs. 3.5b-c where $\mathbf{p}_{ref} = [x \ 0 \ 0.2\sin(1.5t)]'$. This would hint at potential 3D path following in complex environments.

Next, we test the control algorithm experimentally. $\mathbf{p}_{ref} = [x \ 0 \ 0]'$ for all cases with an error threshold of ± 0.1 mm (this is larger compared to the simulations in order to account for the error in position estimation of the swimmer) and $K_{p,y} = K_{p,z} = 1$ again. This value is concluded by testing different gain values (not shown). f_m is set to 10 Hz, $B_0 \sim 5$ mT and $|\mathbf{m}| \sim 6 \times 10^{-4} A.m^2$. This configuration prevents step-out (Zhang et al., 2009) while providing a strong propulsion to the swimmer. Note that gravitational effects are negligible at these rotation rates as the swirling flow lifts the swimmer, hence, there is no additional compensation for gravity. Figs. 3.6a-c show the non-dimensional radial position (β), defined as in Eq. 2.14. While the helical path is suppressed significantly in both cases, the swimmer reaches to

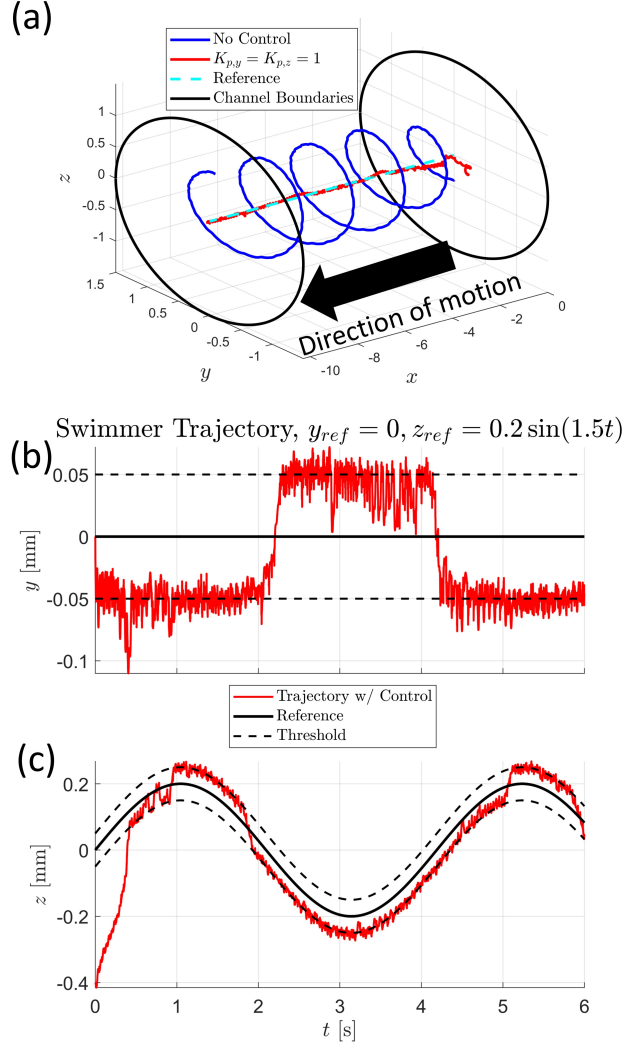


Figure 3.5 (a) 3D swimmer trajectories in the pusher-mode from the kinematic model with and without control. (b) y - coordinates and (c) z - coordinates of the swimmer for $\mathbf{p}_{ref} = [x \ 0 \ 0.2\sin(1.5t)]'$.

the reference path within the threshold for $D_{ch} = 3$ mm but fails in the 5.6-mm channel within the duration of the experiment. The length of the experiment setup alongside the channel axis is too short to show fully converged trajectories inside the wider channel but there is a significant decrease in β compared to the case without control. Noting that the same control gains are applied in both cases, it is natural that the algorithm performs worse for a wider channel where Ma and swirl rates are lower. While the swirling flow causes helical trajectories, it is beneficial in achieving quicker convergence to the reference path. The control input could not be increased further due to hardware limitations. There is also the issue of delayed response due to hardware and image processing. Here, the control input is updated at each rotation of the swimmer, corresponding to a response time of 0.1 s. The

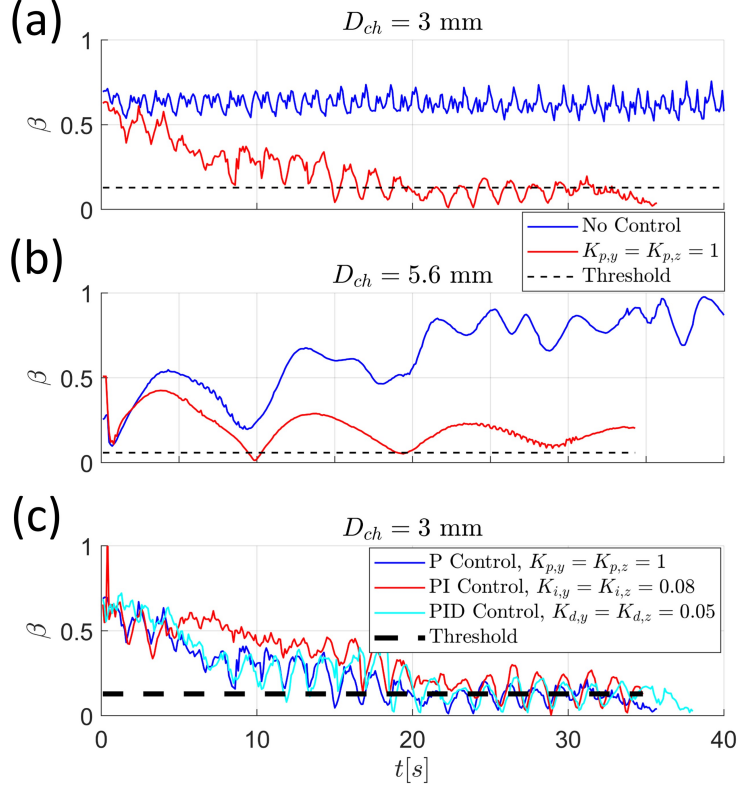


Figure 3.6 Non-dimensional trajectory radii with and without control in the channels where (a) $D_{ch} = 3$ mm, (b) $D_{ch} = 5.6$ mm. (c) shows the performance of different control strategies under $D_{ch} = 3$ mm. Note that $K_{i,\{y,z\}}$ for PID control are the same as in PI control.

algorithm should perform better if these problems are resolved, as the numerical results indicate.

We conduct additional experiments for $D_{ch} = 3$ mm. P, PD, PI and PID control are tested as defined in Eq. 3.19. The change of β under these scenarios are shown in Fig. 3.6c (the trajectory with PD control is omitted as it is very similar to the trajectory with PID control). PI control increases the oscillations in the system while P, PD and PID control result in similar paths under optimal gain values. The reason for similar performance can be attributed to the limitations in suppression of the helical paths. P control appears to be sufficient in suppression to a degree while these additional inputs cannot contribute any further. Wobbling cannot be suppressed completely either, as shown in the simulation results in Figs. 3.4 and 3.5. As Ma number is finite, some wobbling will remain even if Ma is very high. Higher integral or derivative gains quickly destabilize the system because of the oscillatory nature of the trajectories. Higher P-gain could improve the control performance but the increase in magnetic torque may trigger more wobbling, so it cannot be increased indefinitely.

The control algorithm presented here assumes that there is some information on swimmer position. However, as stated in Martel (2013), this information may not be highly accurate, delayed or not available at all. The following chapters will investigate acoustic fields as another way of stabilizing oscillatory trajectories and improving swimming performance without any need for accurate swimmer position information.

4. Modelling Acoustic Radiation Force on Helices

Magnetic manipulation of helical swimmers is possible through a feedback control algorithm which may not be reliable at all times as maintaining visual contact in *in vivo* applications or obtaining proper swimmer position information despite the availability of visual contact is not possible at all times. Realizing a passive way of manipulating the swimmers would be a more robust solution to the oscillatory swimming problem. This dissertation proposes acoustic fields as a way of improving controlled navigation and improving swimming performance. Acoustic fields' bio-compatible nature and penetration into human body make them ideal complements to the magnetic actuation. Acoustic radiation force is one of the two major ways one can manipulate objects in an acoustic field. The calculation of the force for intricate mm-scale objects at MHz-scale acoustic frequencies is only possible through finite-element models which are computationally very expensive. This chapter presents a very efficient approach, called chain-of-spheres, to evaluate the radiation force acting on helices. The comparisons with FEM results show a satisfactory level of accuracy.

4.1 Acoustic Radiation Force

The acoustic radiation force on an object is calculated from the pressure field on the object surface. Helmholtz equations are resolved to evaluate the pressure field. For a 1-dimensional wave, the equation is:

$$(4.1) \quad \frac{\partial^2 p}{\partial z^2} - \frac{1}{c_0^2} \frac{\partial^2 p}{\partial t^2} = 0$$

where p is the acoustic pressure, z is the Cartesian coordinate component, c_0 is the speed of sound in the medium and t is time. The solution to this equation comes out as:

$$(4.2) \quad p = p_a \sin(\omega_a t \pm kz)$$

where p_a is the amplitude of the pressure wave, $\omega_a = 2\pi f_a$ is the angular frequency and $k = 2\pi/(c_0/f_a)$ is the wave number. Placing a tiny object in this acoustic field will disturb it and the total pressure will have a background and scattered component:

$$(4.3) \quad p = p_b + p_{sc}$$

In calculation of the acoustic radiation force, the perturbation approach is preferred by many authors (Garbin et al., 2015; Glynne-Jones et al., 2013; Settnes & Bruus, 2012; Wang & Dual, 2009). In this approach, pressure and density are decomposed into two components: The component without any acoustic contribution (identified with subscript 0) and the variation component due to acoustic wave (first and second order terms, identified with subscripts 1 and 2, respectively):

$$(4.4) \quad \begin{aligned} p &= p_0 + p_1 + p_2 \\ \rho &= \rho_0 + \rho_1 + \rho_2 \end{aligned}$$

Note that the first order pressure term is $p_1 = c_0^2 \rho_1$. For an inviscid fluid, Navier-Stokes equations will only have the convective terms:

$$(4.5) \quad \begin{aligned} \frac{\partial \rho_1}{\partial t} &= -\rho_0 \nabla \cdot \mathbf{v}_1 \\ \rho_0 \frac{\partial \mathbf{v}_1}{\partial t} &= -c_0^2 \nabla \rho_1 \end{aligned}$$

Assuming time-harmonic fields due to the nature of the acoustic wave:

$$(4.6) \quad \begin{aligned} \rho_1 &= \rho_1(\mathbf{r})e^{-i\omega_a t} \\ p_1 &= p_1(\mathbf{r})e^{-i\omega_a t} \\ v_1 &= v_1(\mathbf{r})e^{-i\omega_a t} \end{aligned}$$

Here r is the spherical coordinate component. The reason spherical coordinates are used in the literature is related to most of the calculations being specific to spherical particles. The velocity potential ϕ_1 has the following relationships with velocity, pressure and density:

$$(4.7) \quad \begin{aligned} \mathbf{v}_1(\mathbf{r}) &= \nabla\phi_1(\mathbf{r}) \\ p_1(\mathbf{r}) &= i\rho_0\omega_a\phi_1(\mathbf{r}) \\ \rho_1(\mathbf{r}) &= i\frac{\rho_0\omega_a}{c_0^2}\phi_1(\mathbf{r}) \end{aligned}$$

The potential satisfies the wave equation given as:

$$(4.8) \quad \nabla^2\phi_1 = \frac{1}{c_0^2}\frac{\partial^2\phi_1}{\partial t^2} = -\frac{\omega_a^2}{c_0^2}\phi_1$$

The acoustic radiation force appears over a full period of the acoustic wave through the second order term as the first order terms are harmonic and their time-average results in zero. The time-averaged second order pressure term is shown in Bruus (2012) to be:

$$(4.9) \quad \langle p_2 \rangle = \frac{1}{2\rho_0 c_0^2} \langle p_1^2 \rangle - \frac{1}{2} \rho_0 \langle v_1^2 \rangle$$

For a fixed particle, the acoustic radiation force on an object is evaluated from:

$$(4.10) \quad -\mathbf{F}_{fixed}^{rad} = \left\langle \int_S p_2 \mathbf{n} dS \right\rangle$$

where S is the object surface and \mathbf{n} is the surface normal. If the object is free to move, this integration has to be taken over a time varying surface $S(t)$ as the particle exhibits small oscillations as the wave passes through. This integration is challenging to compute in a frequency-domain study. Yosioka and Kawasima (1969) propose computing the integral over an equilibrium position surface S_0 and adding a convective correction term:

$$(4.11) \quad -\mathbf{F}_{free}^{rad} = \left\langle \int_{S(t)} p_2 \mathbf{n} dS \right\rangle = \left\langle \int_{S_0} p_2 \mathbf{n} dS \right\rangle + \left\langle \int_{S_0} \rho_0 (\mathbf{n} \cdot \mathbf{u}_1) \mathbf{u}_1 dS \right\rangle$$

Note that this S_0 is taken at a boundary outside the object in order to calculate the momentum flux term. Even though this formulation assumes the body is free to move, applying the formulation to an already moving object such as the magnetized helix causes an ambiguity over the surface of integration and the momentum flux correction. It is assumed that the oscillations on the helix surface (which leads to the addition of the momentum correction term) is negligible compared to the swimming velocity of the helix.

In the presence of an object, the pressure term can be decomposed into incident and scattered terms:

$$(4.12) \quad p^2 = p_i^2 + 2p_i p_{sc} + p_{sc}^2$$

For small objects, p_{sc}^2 term will be negligible and the analytical calculations for spheres mostly neglect this term (Bruus, 2012; Hasegawa, 1977; Hasegawa & Yosioka, 1969).

4.2 Analytical Modeling and Chain-of-Spheres Approach

Acoustic radiation force on the helical swimmer is calculated by approximating the swimmer as an array of spheres placed along the centerline of the helix. The centerline is as given as:

$$(4.13) \quad \mathbf{p}_h = \begin{bmatrix} A_h \cos(k_h z_h) \\ A_h \sin(k_h z_h) \\ z_h \end{bmatrix}$$

where z_h is the z -coordinate and k_h is the wave number of the helix. Sphere radius a is first set equal to $d/2$ and the spheres are placed along the centerline of the helix with equal distance between each other. As the acoustic radiation force is a volumetric force, a is adjusted to match the volume of the sphere array and the helix. As a result of this volume matching, the spheres end up intersecting with each other as shown at Fig. 4.1. However, as each sphere is treated separately, there is no intersection or cross-interaction in the physical sense. The sensitivity of the chain-of-spheres approach with respect to the number of spheres used in the representation will be discussed at Section 4.4.

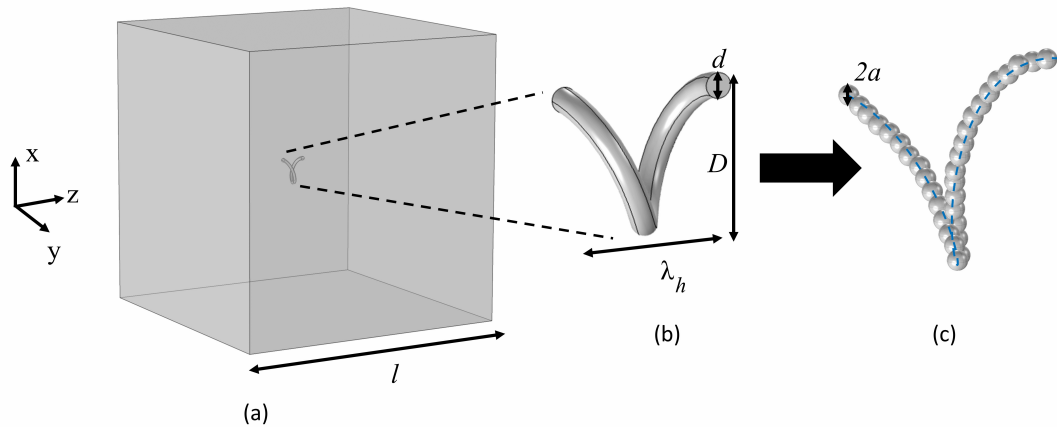


Figure 4.1 (a) Placement of a single turn helix with respect to global coordinates. (b) Close-up view of the helix and its geometric parameters. (c) Representation of the helix as a chain of spheres. The spheres are placed along the centerline of the helix, shown with blue dashes.

The acoustic radiation force on a rigid sphere was first evaluated analytically by King (1934). This study was followed by Hasegawa & Yosioka (1969) where com-

compressible spheres were studied. These studies evaluated the acoustic radiation force by including second order pressure terms in the calculations. The resultant expressions are in the form of sum of Bessel functions. On the other hand, there is a second approach which was first devised by Maidanik & Westervelt (1957) where the authors calculate the acoustic radiation force through the net loss of linear momentum. This approach is used in the FEM models (Garbin et al., 2015; Glynne-Jones et al., 2013). This section describes the analytical models developed by Hasegawa (1977).

The incident velocity potential due to a plane traveling wave can be represented as:

$$(4.14) \quad \phi_{i,tr} = A \sum_{n=0}^{\infty} (2n+1) (-i)^n j_n(kr) P_n(\cos(\theta)) e^{i\omega t}$$

where A is the complex amplitude of the incident velocity potential, n is the Bessel function order and j_n is the spherical Bessel function of order n . r and θ are the components of the spherical coordinate frame and $P_n(\cos(\theta))$ is the Legendre polynomial. There is also a scattered component if one places a spherical object in the field. The scattered field is expressed as:

$$(4.15) \quad \phi_{s,tr} = A \sum_{n=0}^{\infty} (2n+1) (-i)^n c_{na} h_n^2(kr) P_n(\cos(\theta)) e^{i\omega t}$$

where c_{na} is the scattering coefficient and h_n^2 is the Hankel function of second kind. The scattering coefficient is determined by appropriate boundary conditions. In this scenario, there are three boundary conditions to apply (Hasegawa & Yosioka, 1969):

- 1.1 Sum of the pressure in the fluid and the normal component of the stress on the sphere is zero.
- 1.2 The normal component of the displacement of the fluid is equal to the solid's.
- 1.3 The tangential components of the shear stress are zero.

Hasegawa & Yosioka (1969) calculate $c_{na} = \alpha_n + i\beta_n$ based on these conditions. The reader is referred to the cited work for the complete form of c_{na} . The authors define

a radiation force function, Y_p as a measure of the radiation force in non-dimensional form. Hasegawa simplifies the expression at Hasegawa & Yosioka (1969) to:

$$(4.16) \quad Y_p = -\frac{4}{x^2} \sum_{n=0}^{\infty} (n+1)(\alpha_n + \alpha_{n+1} + 2\alpha_n\alpha_{n+1} + 2\beta_n\beta_{n+1})$$

in his 1977 study (Hasegawa, 1977). Here $x = ka$. The model is built in Matlab and the values come out exactly the same as in Hasegawa (1977) for $n = 20$.

Hasegawa (1979) also derives the radiation force function in a similar fashion for a stationary wave:

$$(4.17) \quad Y_{st} = \frac{8}{x^2} \sum_{n=0}^{\infty} (n+1)(-1)^{n+1}(\beta_n(1+2\alpha_{n+1}) - \beta_{n+1}(1+2\alpha_n))$$

Note that the expression does not contain the extra x^2 term in the sum (the term exists in the original manuscript) as this is a typographical error pointed out by Mitri (2005).

Acoustic radiation forces in the propagation direction of the waves are given as functions of the force function terms in Eqs. 4.16 and 4.17:

$$(4.18) \quad F_{tr}^r = \pi a^2 E Y_p$$

$$(4.19) \quad F_{st}^r = \pi a^2 E Y_{st} \sin(2kh)$$

where $E = 0.5\rho_0 k^2 |A|^2$ is the acoustic energy density and h is the distance of sphere to a velocity node. For stationary waves, the spatial variation is reflected through h in Eq. 4.19. For travelling waves, there is no need for such a distinction as the time scale of the wave ($f_a = 1$ MHz) and the helix ($f_m = 20$ Hz) and also the velocity of the wave ($c_0 = 1480$ m/s for water) and the helix (several cm/s at most when the acoustic field is applied) are vastly different, meaning that the force can be assumed to have constant amplitude in average. Using the chain-of-spheres representation

of the helix (in Fig. 4.1), the total acoustic radiation force on a slender helix is obtained by the summation of the acoustic radiation force on each sphere:

$$(4.20) \quad F_{\{tr,st\}}^{rad} = \sum_{j=1}^{N_{sph}} F_{j,\{tr,st\}}^r$$

In this notation, $j = 1, 2, \dots, N_{sph}$ corresponds to the sphere number in the sphere array that represents the helix. N_{sph} is the total number of spheres in this array.

In the current study, the plane waves are in the z - direction. Hence, the acoustic radiation force vector will have the form:

$$(4.21) \quad \mathbf{F}^{rad} = \left[0 \quad 0 \quad F_{\{tr,st\}}^{rad} \right]'$$

where $'$ sign indicates the transpose. For a swimmer with its center-of-mass placed at the coordinates \mathbf{p} , the acoustic radiation torque is evaluated from:

$$(4.22) \quad \boldsymbol{\tau}^{rad} = \sum_{j=1}^{N_{sph}} (\mathbf{c}_j - \mathbf{x}) \times \mathbf{F}_j^{rad}$$

where \mathbf{c}_j for $j = 1, 2, \dots, N_{sph}$ corresponds to the center-of-mass of the sphere j . The coordinates of the array of spheres range from $z_{h,min} = -N_h \lambda_h / 2$ to $z_{h,max} = N_h \lambda_h / 2$ such that the center-of-mass of the swimmer is at $\mathbf{x} = \left[0 \quad 0 \quad 0 \right]'$. The verification of the model is provided in Section 4.4.

4.3 Finite Element Modelling

Finite-element models are built based on the models in the literature. One of the models is the one by Glynn-Jones et al. (2013) which is an axisymmetric model for the evaluation of acoustic radiation force on a sphere. As shown at Fig. 4.2, a half-circle is placed at the symmetry axis of the cylindrical fluid domain. The sides

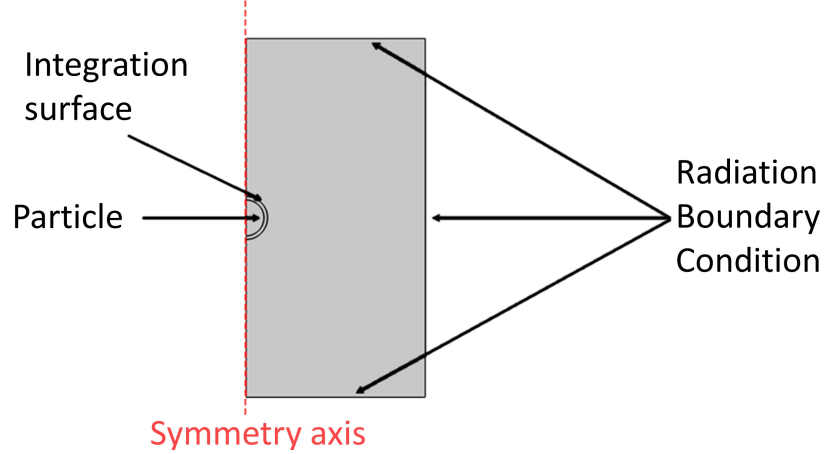


Figure 4.2 Geometric setup of the model in Glynne-Jones et al. (2013).

of the cylindrical domain have cylindrical wave radiation condition, meaning that the incident wave does not reflect back into the domain. A background pressure field (standing wave in z - direction) is applied to the whole fluid domain:

$$(4.23) \quad p_b = p_a \cos(kz)$$

The object is treated as a solid with its own solid mechanics physics. The solid mechanics physics and pressure acoustics are coupled with force and acceleration boundary conditions: The solid object boundary receives the force from the pressure acoustics model while the pressure acoustics model receives the acceleration of the surface through the solid mechanics physics.

This model can only account for 3-dimensional axisymmetric structures whereas a helix is a 3-dimensional structure that cannot be represented in such a model. Garbin et al. (2015) present a 3-dimensional pressure acoustics model for the evaluation of acoustic radiation force on spheroid and ellipsoid objects. The domain simulated is cubic and the sides are covered with perfectly matched layers (PMLs). This model is taken as the basis to build the reference model to evaluate the acoustic radiation force on helical structures. In order to reduce the computational load, PMLs are replaced with plane wave radiation conditions. The domain size, originally, $60 \times 60 \times 60 \mu\text{m}$ is increased to $5 \times 5 \times 5 \text{ mm}$ to account for larger structures (Refer to Fig. 4.1a). Since there is no way to validate the acoustic radiation force on helices, the model is verified with the results for spherical particles in Glynne-Jones et al. (2013). The results are given at Table 4.1.

Material\Study	Glynne-Jones et al. (2013) [N]	Yosioka & Kawasima (1969, Analytical) [N]	3D FEM Model [N]
Glass	1.31E-10	1.33E-10	1.32E-10
Nylon	5.93E-11	6.67E-11	3.67E-11
Polystyrene	4.27E-11	5.57E-11	3.96E-11
Steel	1.8E-10	1.81E-10	1.79E-10
Aluminum	1.43E-10	1.44E-10	1.43E-10

Table 4.1 Comparison of 3-dimensional FEM model results with those from the literature for spheres made of several different materials.

The helical geometry simulated in the FEM model is as given in Eq. 4.13. The simulation setup and the helix geometry are shown at Figs. 4.1a and 4.1b, respectively. Properties of the materials used in the thesis is provided at Table 4.2. Initial tests with the model for a nickel helix exhibited non-converging results despite the refinements such that the solver requires more than 300 GB RAM. Further investigation revealed that the meshing on the object and the domain should be significantly different: The model is insensitive to meshing in the fluid domain beyond the element size of $\lambda/3$ but the elements on the object should be as small as several microns for an acoustic frequency of 1 MHz, giving an element size to λ ratio close to 1/200. The convergence plot provided at Fig. 4.3 shows that the convergence is achieved at around 2-3 million degrees-of-freedom (DOF) for the geometry with the parameters given at 4.3.

Property\Material	Water (Liquid)	Nickel (Swimmer)	Nylon (Swimmer)
Density [kg/m³]	1000	8900	1110
Compressibility [Pa⁻¹]	4.54E-10	5.55E-12	3.33E-10
Viscosity [Pa·s]	1E-3	-	-
Speed of sound [m/s]	1480	-	-
Longitudinal-wave speed [m/s]	-	5639	2620
Shear-wave speed [m/s]	-	2970	1070

Table 4.2 Properties of the materials used in the simulations.

Geometric parameter	Value
$\lambda_h [\mu\text{m}]$	1000
$D [\mu\text{m}]$	800
$d [\mu\text{m}]$	40
N_h	1

Table 4.3 Geometric parameters of the helix used for the convergence studies of the 3D FEM model for simulating the acoustic radiation force on helices.

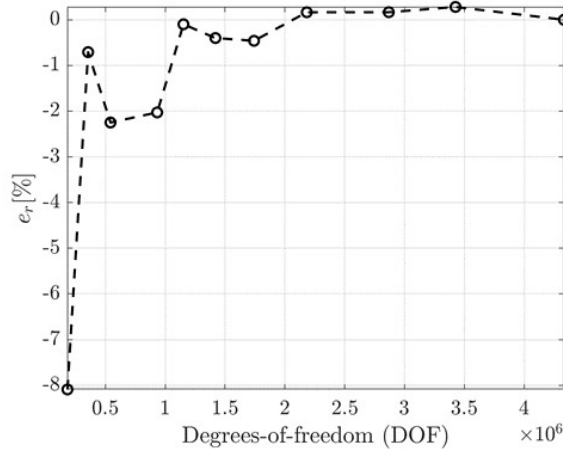


Figure 4.3 Mesh convergence plot of the FEM model.

4.4 Chain-of-Spheres Simulations: Verification

The chain-of-spheres approach is validated through geometric and physical parametric sweeps. A helical tail made of nickel and another one made of nylon (properties given at Table 4.2), with the base dimensions given at Table 4.4 are simulated in the FEM model. The geometric scale of the swimmer used for the validation is smaller than the ones used in trajectory simulations and mesh convergence studies for computational efficiency. A typical FEM simulation for this geometry requires about 23 GB of RAM and 114 seconds of CPU time on a high end workstation. Also note that $z_{h,min} = -N_h \lambda_h$ and $z_{h,max} = 0$ for the studies reported in this subsection. For $p_a = 100$ kPa, $f_a = 1$ MHz, the radiation force on the helix made of nickel in water (properties listed at Table 4.2) is computed as -78.09 pN. Using the chain-of-spheres approach, with $N_{sph} = 21$ and $a = 11.508 \mu\text{m}$, the force comes out as

Geometric parameter	Value
$\lambda_h[\mu\text{m}]$	100
N_h	1
$d[\mu\text{m}]$	10
$D[\mu\text{m}]$	60

Table 4.4 Geometric parameters of the helix used in the validation studies.

-72.94 pN, corresponding to an error of -6.58%. For the nylon helix, the FEM result is -23.78 pN while the chain-of-spheres approach (with the same N_{sph} and a used for the nickel helix) gives -23.77 pN, corresponding to an error rate of -0.04%. The chain-of-spheres approach evaluates the radiation force in 9 seconds and the code requires negligible computer memory. Different p_a (from 1 kPa to 1 MPa) and f_a (from 0.1 to 5 MHz) values are tested and error rates remain the same (not shown). The approach fares much better with nylon than nickel, as evidenced further by the geometric parameter sweeps whose results are plotted at Fig. 4.4. The highest maximum absolute error is 12% for the nickel helix whereas the absolute error remains below 2% for the nylon helix. This is due to the difference in the acoustophoretic contrast factors of nickel and nylon. The factor, denoted with Φ , is defined as:

$$(4.24) \quad \Phi = \frac{1}{3} \left(1 - \frac{\kappa_s}{\kappa_0} \right) + \frac{1}{2} \left(\frac{2 \left(\frac{\rho_s}{\rho_0} - 1 \right)}{2 \left(\frac{\rho_s}{\rho_0} \right) + 1} \right)$$

where κ_s is the compressibility of the solid, κ_0 is the compressibility of the liquid and ρ_s is the solid density (Bruus, 2012). Based on the data from Table 4.2, Φ comes out as 0.7495 for nickel and 0.1231 for nylon. The lower contrast factor for nylon results in lower scattered field magnitude. The unique scattered field of the helix cannot be replicated with the chain-of-spheres approach as each sphere is treated separately, resulting in a different scattered field. That is why the lower contrast factor, which reduces the scattered field effects, helps in evaluating a closer radiation force value. In this study we focus on the nickel one in accordance with the aim of simulating acousto-magnetic helical swimmers, for which the error is still reasonable for practical applications such as design and control.

In addition to the helix material, the chain-of-spheres model is validated with a sensitivity analysis with respect to the following geometric parameters: the number of helical turns, N_h , minor, d , and major, D , diameters of the helix and λ_h , in Fig. 4.4. In the sensitivity of the model against N_h , a lower λ_h value (50 μm) is used rather than the reference value in Table 4.4, i.e. 100 μm to efficiently simulate cases

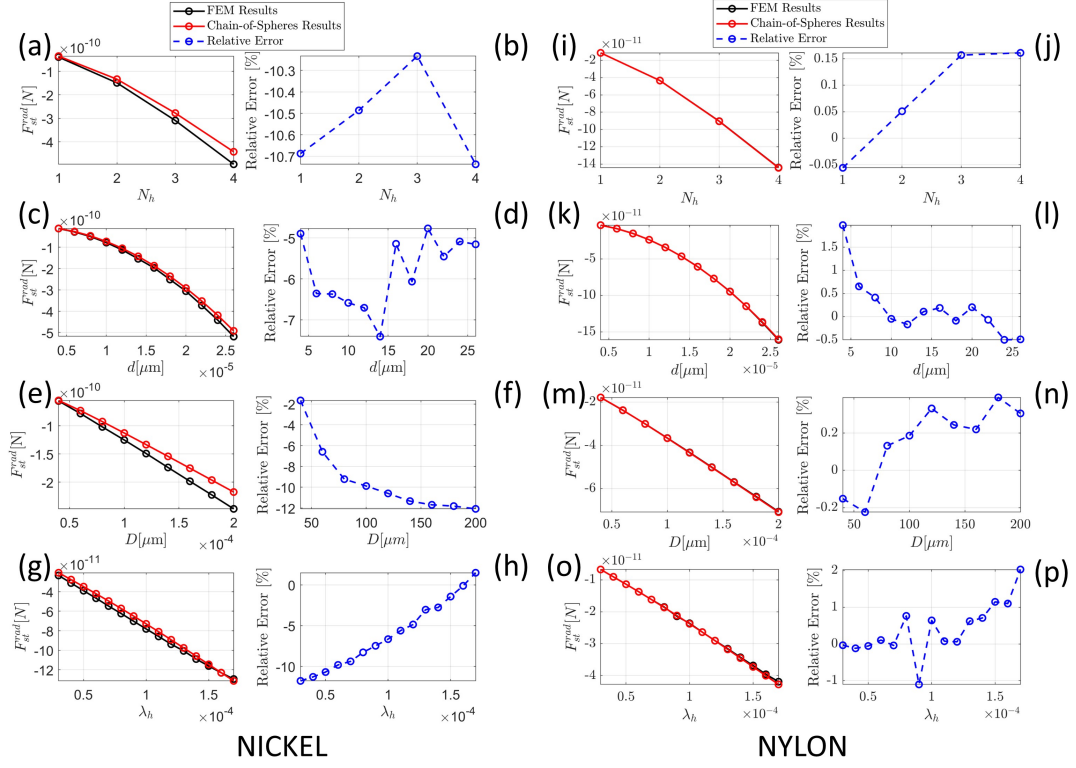


Figure 4.4 Validation of the chain-of-spheres approach with respect to different geometric parameters. (a) to (h) show the results for nickel, (i) to (p) show the results for nylon. (a) and (b) ((i) and (j) for nylon) show the radiation forces and relative error with respect to N_h , (c) and (d) ((k) and (l) for nylon) show the forces and relative errors with respect to d , (e) and (f) ((m) and (n) for nylon) show the forces and relative errors with respect to D and (g) and (h) ((o) and (p)) show the forces and relative errors with respect to λ_h .

with larger N_h , because of large computational cost and memory requirement of simulating helices with a large number of turns with the finite-element method for validation. Both the FEM and chain-of-spheres models show that the magnitude of the acoustic force increases with N_h non-linearly for both nickel and nylon helices with an order of magnitude higher value for the nickel than the nylon helix (Figs. 4.4a and 4.4i). The absolute error between the two models remains almost constant for the nickel helix, 10%, (Fig. 4.4b), indicating that the chain-of-spheres model results are fairly insensitive to the number of helical turns in this parameter range for a typical helical microswimmer made of nickel, thus a single turn helix is used throughout the simulations for other parameters. Whereas for nylon, the absolute error between FEM results and chain-of-spheres approximation is less than 0.15%.

For both materials, the magnitude of the acoustic radiation force increases with the minor diameter almost quadratically (Figs. 4.4c and 4.4k), with curve fitting for the nickel helix values resulting in the equation $F_{st}^{rad} = -2.915d^2$ where F_{st}^{rad} is in

pN and d is in μm . For the nickel helix, the magnitude of the error varies between 5% and 7% (Figs. 4.4c and 4.4d), whereas for the nylon helix the maximum error is about 2% for the smallest d . This quadratic increase with the minor diameter of the helix because the acoustic radiation force increases with the volume as long as the span of the helix remains fixed with respect to the acoustic wave.

The acoustic radiation force, F_{st}^{rad} , increases almost linearly with the major diameter for both helices in Figs. 4.4e and 4.4m (Curve fitting for the nickel helix values gives the equation $F_{st}^{rad} = -2.046D - 11.66$ where F_{st}^{rad} is in pN and D is in μm). This linear increase with D is the indicative of the volumetric effect of the radiation force: since the volume of the helix increases linearly with D and the span of the helix remains the same with respect to the incident pressure wave. The maximum error between the FEM and chain-of-spheres models is about 12% for the largest D for nickel helices, and about 0.2% for nylon helices.

The sensitivity over λ_h is demonstrated at Figs. 4.4g-h. The acoustic force increases linearly with the wavelength of the helix (The force values for the nickel helix are fit to the equation $F_{st}^{rad} = -0.82\lambda_h + 4.984$ where F_{st}^{rad} is in pN and λ_h is in μm). The linear dependence of F_{st}^{rad} on λ_h vs. the quadratic dependence on N_h is demonstrated in Fig. 4, which shows the scattered fields for two helices with a total length of $150\ \mu\text{m}$ but one has $N_h = 3$ (meaning $\lambda_h = 50\ \mu\text{m}$) whereas the other one has $N_h = 1$. The maxima of the scattered field are the same at both cases (as they span the same region along the acoustic wave) but the helix at $N_h = 3$ has a significantly larger scattered field distribution overall. Furthermore, both the volume and the side area of the helix (the area directly exposed to the acoustic wave) are larger when $N_h = 3$, thereby the radiation force grows faster as N_h increases.

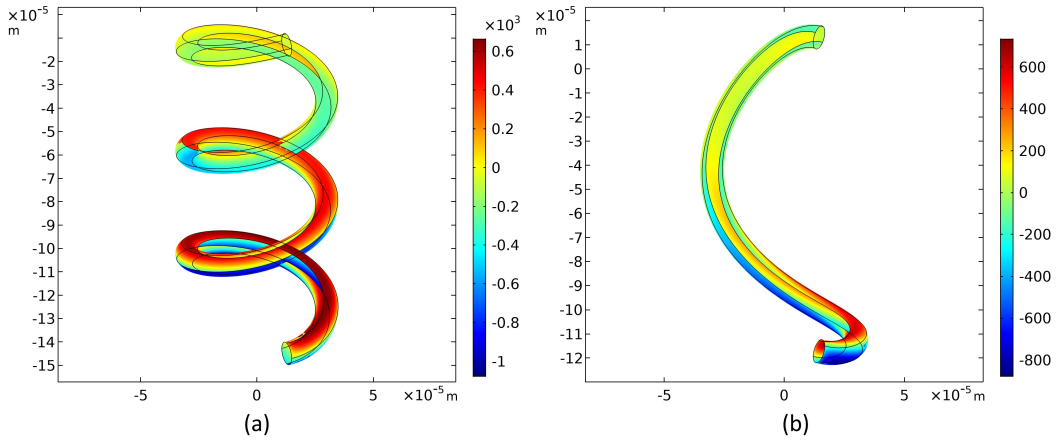


Figure 4.5 The distribution of scattered pressure field for helices with (a) $\lambda_h = 50\ \mu\text{m}$ and $N_h = 3$ and (b) $\lambda_h = 150\ \mu\text{m}$ and $N_h = 1$. Other parameters are as given in Table 4.4

The chain-of-spheres approach underestimates the radiation force at lower λ_h and the error decreases steadily as λ_h increases. As λ_h increases further, the chain-of-spheres approach starts to overestimate the force on the helix. One can infer that the overestimation occurs due to the increase in N_{sph} for large λ_h . As the results in Fig. 4.6 will show, however, the radiation force for a fixed geometry converges to a steady value at large N_{sph} values as long as the volume matching is realized. F_{st}^{rad} is overestimated here as the helix geometry extends towards the regions with high background pressure while the force is underestimated when the helix geometry spans the regions with low background pressure.

Next, a parametric sweep over N_{sph} is carried out to observe the sensitivity of the approach on N_{sph} . Both the radiation forces and torques are investigated as the acoustic torques have relevance in RFT simulations discussed in Section 5.2 and 5.3. In order to keep the results relevant to the helical geometry in Section 5.3, the geometric parameters at Table 4.5 are used in this study. Furthermore, the swimmer is rotated around \mathbf{x} - axis by 20° and rotated around \mathbf{z} - axis by 100° to obtain larger torques in multiple directions. The spheres are still placed according to the placement rule described in Section 4.2, with larger or smaller distances between each sphere depending on N_{sph} . Fig. 4.6 shows the force and torque values with respect to N_{sph} , alongside with the values calculated from the FEM model. The radiation force estimation is very accurate down to $N_{sph} = 6$. However, acoustic torque calculation converges to steady values only when $N_{sph} > 20$. A further increase in N_{sph} does not contribute to a better estimation of the forces. The results show that it is always better to use a large number of spheres for a better estimation of the forces and torques.

The torque values at Fig. 4.6b exhibit a discrepancy in comparison to the FEM results. We investigate the torque estimation further by evaluating the torques during a complete rotation of the swimmer around the \mathbf{z} - axis. (The rotation angle is denoted with ϕ). The swimmer remains rotated around \mathbf{x} - axis by 20° in this study as well. Torque in the z - direction is kept out of discussion as it is much lower in magnitude and negligible with respect to the magnetic torque in the same direction.

Geometric Parameter	Value
λ_h [μm]	370
N_h	3
d [μm]	80
D [μm]	500

Table 4.5 Base geometric dimensions of the swimmer used for the trajectory simulations.

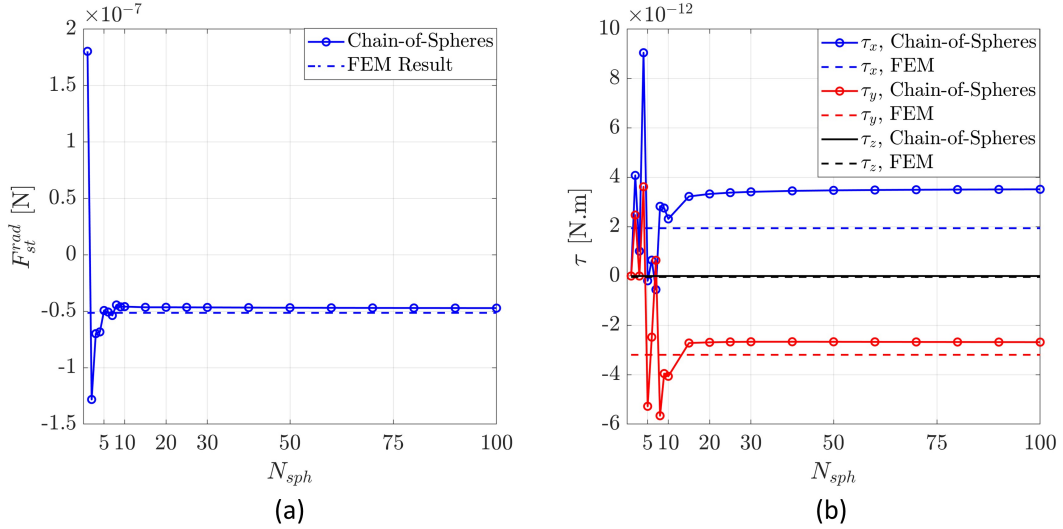


Figure 4.6 (a) Convergence of F_{st}^{rad} with respect to N_{sph} . (b) Convergence of radiation torques with respect to N_{sph} . Dashed lines indicate the values obtained from the FEM simulation.

Fig. 4.7 shows the torque values obtained from the FEM simulations and the chain-of-spheres approach from $\phi = 0$ to $\phi = 340^\circ$. The torques evaluated from FEM simulations are decomposed into its components based on the Cartesian forces that exert the torques. The values for τ_x (noting that this is the direction the swimmer is tilted) show that the chain-of-spheres approach generally overestimates the total τ_x from the FEM model while it approximates τ_x component from F_{st}^{rad} closely around $\phi = 150^\circ$. While τ_x 's component due to radiation force in the \mathbf{y} - direction (denoted with $F_{st,y}^{rad}$) remains lower in amplitude during the rotation of the helical swimmer, averaging over the rotation (values tabulated at Table 4.6) imparts that \mathbf{y} - direction forces end up more dominant. τ_y values at Fig. 4.7b show that the chain-of-spheres approach follows the trend in the FEM results but the estimated torque remains lower in magnitude. Averaging over swimmer rotation again, (results at Table 4.6) it is found that τ_y is 10^3 times lower than τ_x , indicating a very low value. The chain-of-spheres approach evaluates an even smaller average that is practically zero. While the chain-of-spheres approach can approximate the torques to some degree of accuracy, replacing the spheres with spheroids there is room for improvement. Silva & Drinkwater (2018)'s work that deals with the radiation forces for spheroids placed arbitrarily with respect to the wavefront can be utilized for improved accuracy in torque estimation.

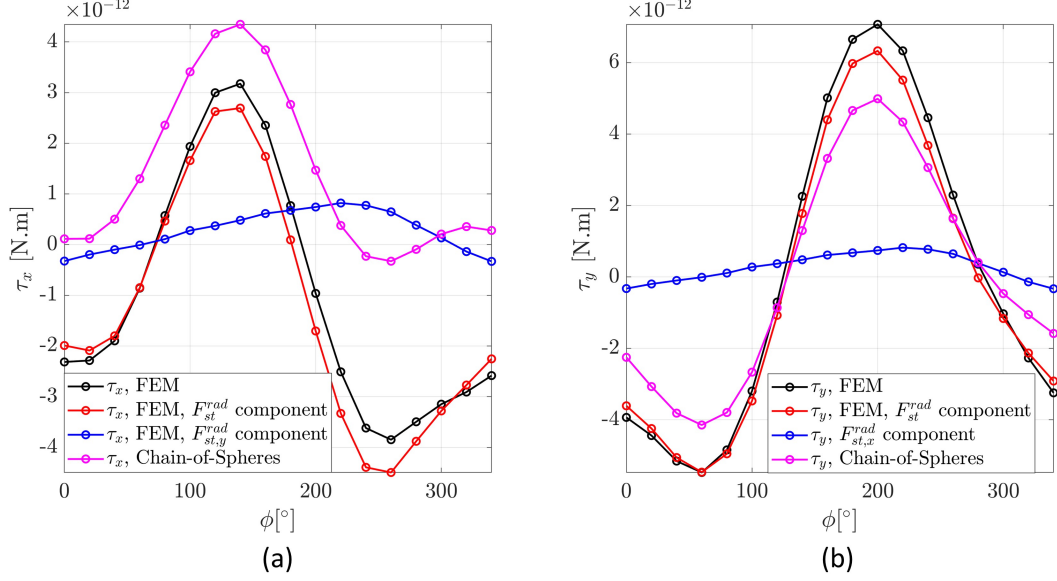


Figure 4.7 (a) Components of τ_x in FEM simulations and τ_x evaluated from the chain-of-spheres approach during a complete rotation of the swimmer. (b) Components of τ_y in FEM simulations and τ_y evaluated from the chain-of-spheres approach during a complete rotation of the swimmer.

Evaluated Term	τ_x [N · m]	τ_y [N · m]
FEM, total torque	-1.03E-12	-8.55E-15
FEM, F_{st}^{rad} component	0.58E-12	-2.65E-13
FEM, lateral force component	-1.62E-12	2.74E-13
Chain-of-spheres	1.38E-12	2.24E-28

Table 4.6 Rotation-averaged torques acting on the tilted helical swimmer.

Now that the formulation for acoustic radiation for helices is established, the approach will be combined with a resistive force theory-based model of helical swimming and effects on the trajectories and propulsion in the forthcoming chapter. The simulation results will be compared with the results from experiments as well.

5. Acoustic Manipulation of Magnetically Actuated Helices

This chapter investigates helical swimmers under acousto-magnetic actuation both numerically and experimentally. In numerical studies, chain-of-spheres approach, described and validated in Chapter 4, will be coupled into the resistive-force-theory based model of helical swimming presented in Chapter 3 to evaluate helical swimmer trajectories under acoustic and magnetic fields. Effects of geometric and physical parameters on trajectories and propulsion velocity are demonstrated. In experimental section, the setup for acousto-magnetic actuation is described and effects of acoustic fields on propulsion velocity are reported.

5.1 Modelling

Acoustic radiation will bring both a force and torque component to Eq. 3.20:

$$(5.1) \quad \begin{bmatrix} \mathbf{F}_{loc}^{rad} \\ \boldsymbol{\tau}_{loc}^m + \boldsymbol{\tau}_{loc}^{rad} \end{bmatrix} = \begin{bmatrix} \mathbf{R}_L & \mathbf{R}_C \\ \mathbf{R}'_C & \mathbf{R}_R \end{bmatrix} \begin{bmatrix} \mathbf{U} \\ \boldsymbol{\omega} \end{bmatrix}$$

where the subscript *loc* indicates "local", referring to the local coordinate frame attached to center-of-mass of the helix. Given that \mathbf{Q}_l is the rotation matrix from the global to local frame, the radiation force and torque in the local coordinate frame is evaluated by:

$$(5.2) \quad \begin{aligned} \mathbf{F}_{loc}^{rad} &= \mathbf{Q}_l \mathbf{F}^{rad} \\ \boldsymbol{\tau}_{loc}^{rad} &= \mathbf{Q}_l \boldsymbol{\tau}^{rad} \end{aligned}$$

Alternative representation of Eq. 5.1 can be given by the mobility matrix, \mathbf{M} , which gives linear and angular velocities of the swimmer due to external forces and torques:

$$(5.3) \quad \begin{bmatrix} \mathbf{U} \\ \boldsymbol{\omega} \end{bmatrix} = \mathbf{M} \begin{bmatrix} \mathbf{F}_{loc}^{rad} \\ \boldsymbol{\tau}_{loc}^m + \boldsymbol{\tau}_{loc}^{rad} \end{bmatrix}$$

5.2 Acousto-Magnetic Propulsion

Acoustic radiation results in a direct improvement in swimmer propulsion under travelling waves. The model described in Section 5.1 is utilized to compute magnetized helical swimmer trajectories under magnetic and acoustic fields. Acoustic field is turned on after steady swimming is achieved. An initial magnetic-only swimming period of $t_m = 6$ s is simulated first to ensure steady swimming. The results show that the acoustic field affects the swimmer almost instantaneously and the effects remain steady, so the simulation duration with magnetic and acoustic fields turned on is set to $t_a = 0.1$ s. Geometric parameters for the basic swimmer design are as given at Table 4.5. Note that the system is solved in non-dimensional terms to prevent numerical instabilities. Man & Lauga (2013)'s approach is followed where the mass scale is μ , the viscosity of the fluid, the time scale is $\omega_m = 2\pi f_m$ and the length scale is Λ . For further details on RFT modelling, the reader is referred to Man & Lauga (2013). As a side note, this reference design is simulated in the FEM model and the relative error in force with the chain-of-spheres approach comes out as -9.23%.

The initial case tested has $p_a = 200$ kPa, $f_a = 1$ MHz and $dz = 0$. Under this configuration, acoustic wavelength is $\lambda_a = 1480\mu\text{m}$. λ_h is first set to 1/4th of λ_a , $370\mu\text{m}$. It is observed that the swimming velocity increases by more than 6 times compared to swimming velocity without acoustics (denoted as $W_{ac}/W_{no,ac}$). Note that $W_{no,ac}$ is around several mm/s at most of the cases reported here. Keeping the swimmer geometry the same, we test a parametric sweep over p_a and f_a . As shown at Fig. 5.1a, $W_{ac}/W_{no,ac}$ has a nearly quadratic relationship with p_a . $W_{ac}/W_{no,ac}$ increases with increasing f_a (shown at Fig. 5.1b) and settles after around $f_a = 2$ MHz. There is a peculiar dip at $f_a = 4.25$ MHz after which $W_{ac}/W_{no,ac}$ once again increases to values at lower f_a .

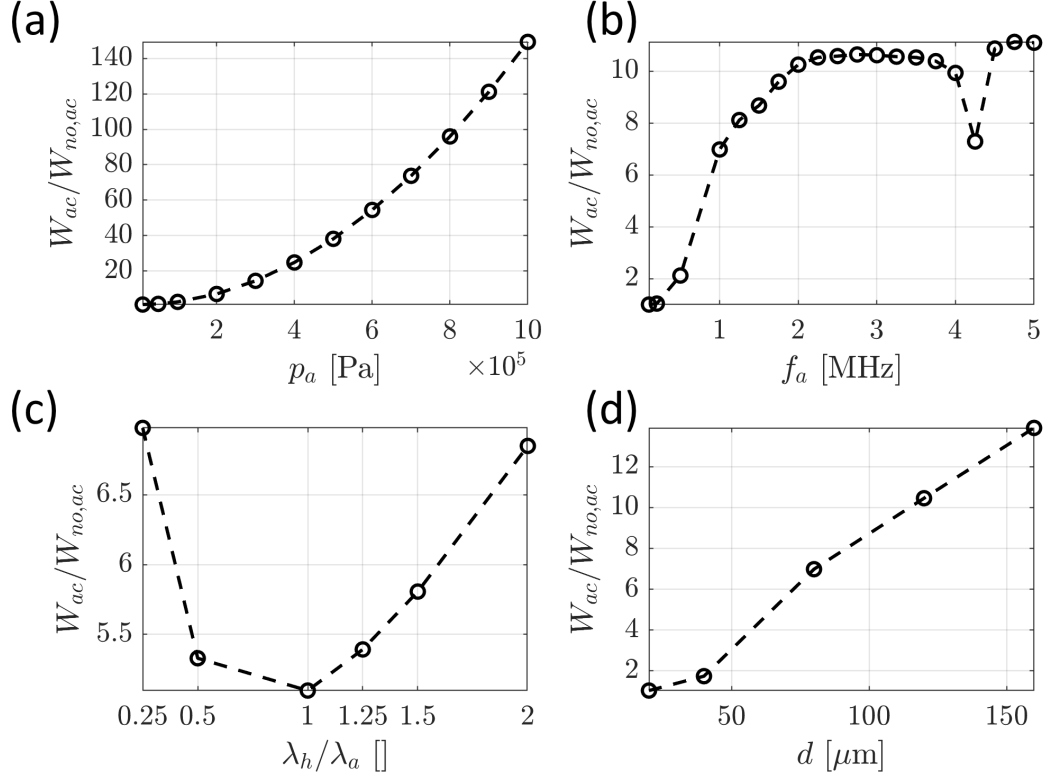


Figure 5.1 Change of the velocity gain, $W_{ac}/W_{no,ac}$, due to the acoustic field with respect to (a) p_a , (b) f_a , (c) λ_h/λ_a and (d) d .

As the acoustic radiation force depends on the volume of the object, it is important to investigate the sensitivity of the acoustic propulsion to geometric parameters. The parametric sweep over λ_h (characterized with λ_h/λ_a at Fig. 5.1c) reveals that $W_{ac}/W_{no,ac}$ is lower when $\lambda_h = \lambda_a$ despite the larger $W_{no,ac}$ than the swimmers with smaller λ_h . For $\lambda_h > \lambda_a$, we see the gain increasing again. Different d values are tested as well, with the results shown at Fig. 5.1d. $W_{ac}/W_{no,ac}$ reaches beyond 10 for $d = 160 \mu\text{m}$. However, it should be noted that this case represents a very thick helix for which the resistive force theory could be inaccurate. The acoustic field has nearly no effect on the swimmer for $d < 40 \mu\text{m}$. This example clearly demonstrates the volume-dependence of the radiation force. This result implies that swimmers with large d in a swarm can be selectively actuated with acoustic fields. The final parameter tested is D where the propulsion gain remains nearly stationary (not shown). This may be due to swimmer geometry not changing along the propagation direction of the acoustic wave.

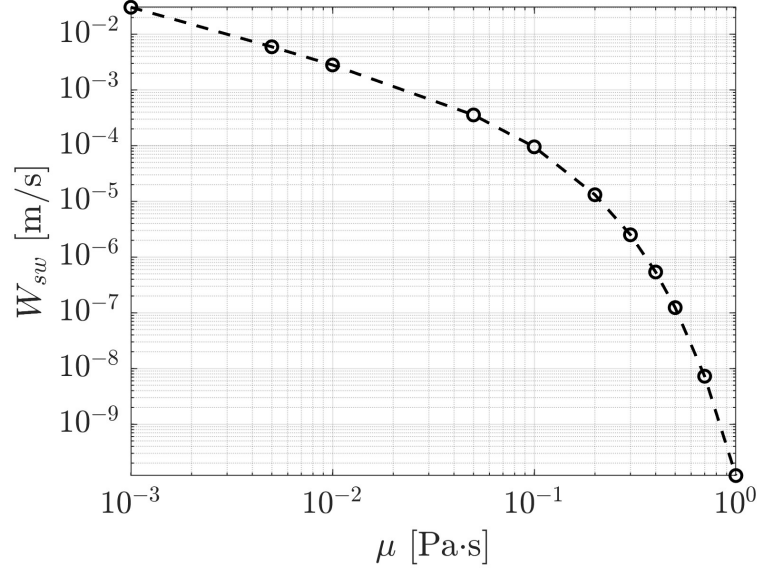


Figure 5.2 Change in W_{sw} with respect to μ .

Another important parameter to investigate in this system is the viscosity of the fluid, μ . The pressure wave attenuates in the fluid that depends on multiple physical parameters:

$$(5.4) \quad \alpha_t = \frac{2\mu\omega_a^2}{3\rho_0 c_0^3}$$

The attenuation modifies the pressure amplitude as following:

$$(5.5) \quad p_b(z) = p_a e^{-\alpha_t z}$$

Fig. 5.2 shows the change of W_{sw} for a helix that is assumed to be stationary (i.e., without magnetic actuation). The viscosity affects both the pressure amplitude and modifies the resistance matrix, leading to a non-linear decrease in W_{sw} as μ increases. The rate of decrease is even faster for $\mu > 0.1$ Pa·s as the velocity decreases 10^4 times for a 10-fold increase in the viscosity.

5.3 Trajectories of Magnetized Helical Swimmers Under Acoustic Fields

The acoustic field is observed to improve swimming trajectories as well. Wobbling is characterized with Mason number (Ma), defined in Eq. 2.18. In order to demonstrate the effects of acoustic field on wobbling, we test the same acoustic field with different Ma numbers for which the trajectory parameters are plotted at Figs. 5.3a-b. At all cases, the acoustic field reduces wobbling significantly, with wobbling angle θ_{ax} larger than 20° reducing down to 5° and helical trajectory radius r_t decreasing from 0.2 mm to 0.05 mm. $W_{ac}/W_{no,ac}$ ratio (not shown) is expected to remain the same as neither the swimmer geometry nor the acoustic field are changed but low Ma number swimmers appear to have a slightly larger gain as the decrease in wobbling improves directed swimming.

The trajectories of the swimmers for the geometric parameter sweeps in Section 5.2 is reported here. The sweep over λ_h reveals that r_t values exhibit similar trends overall while θ_{ax} is already very low at large λ_h without acoustics so the contribution of the field is not much (Refer to Figs. 5.3c-d). We see stronger wobbling at small d values and acoustic field is not able to compensate for it, as shown at Figs. 5.3e-f. At large d values, however, the wobbling is significantly reduced with acoustic field. Larger D values result in larger r_t and θ_{ax} without acoustics but the acoustic field is once again able to compensate for wobbling (Figs. 5.3g-h).

Swimming under standing acoustic fields is tested as well. When acoustics is turned on, time stepping is reduced to $\Delta t_a = 1/(10f_a)$ for a refined solution of propagation under acoustic field. For $f_a = 1$ MHz, this corresponds to $\Delta t_a = 10^{-7}$ s. Standing wave fields are useful for positioning small particles in the nodes or anti-nodes in the field. Here, for a helical swimmer, it is observed that the swimmer reaches a unique position depending on its geometry. A number of swimmers with different λ_h are initiated motion from the same position and the converged positions are displayed at Fig. 5.4. Note that the converged axial positions (Fig. 5.4b) are vastly different from each other. The swimmers are still able to rotate at the converged positions, but they do not move forward or backward due to the acoustic trapping. This may be useful for micro-mixing applications where the swimmer as the mixing agent can be held stationary at a certain position as it rotates in a microfluidic channel with the rotating magnetic field.

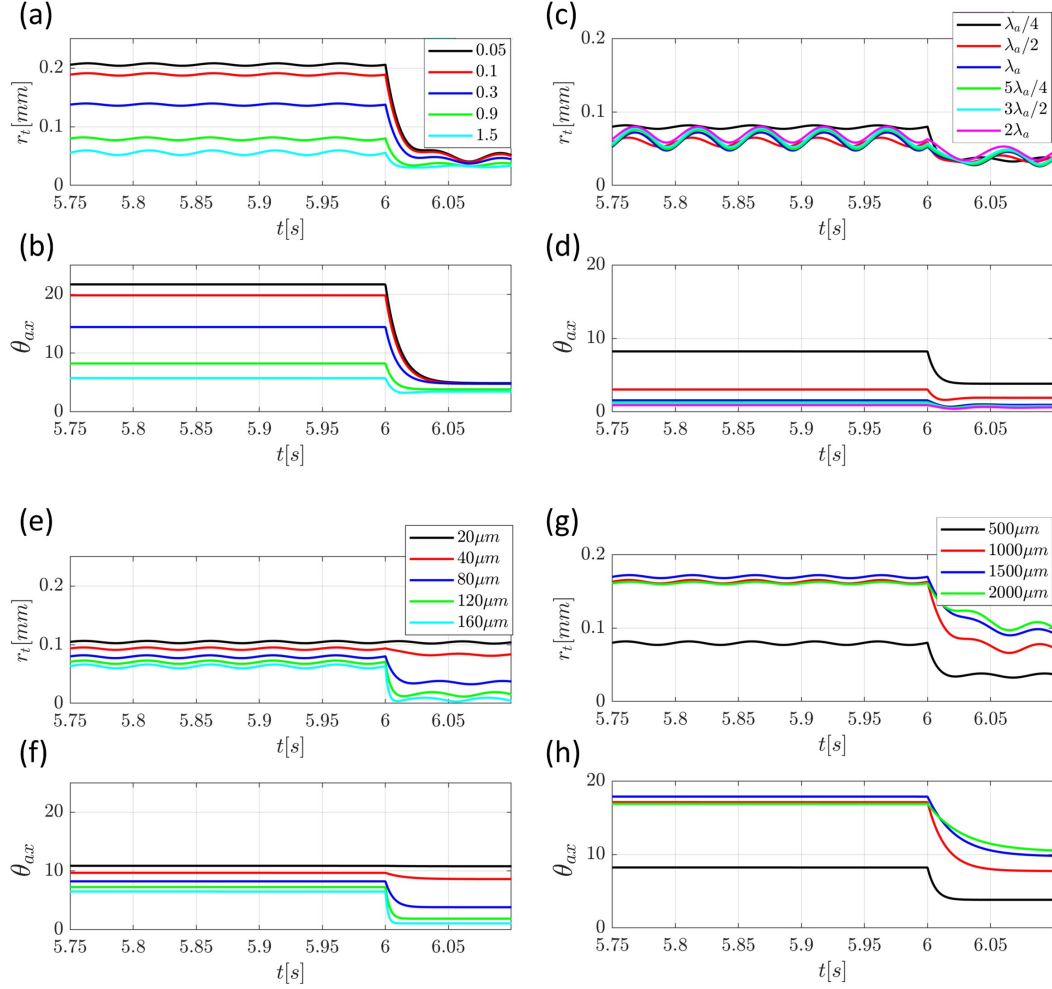


Figure 5.3 Trajectory parameters of magnetized helical swimmers under travelling acoustic field. (a)-(b) show the parameters for different Ma , (c)-(d) show for different λ_h , (e)-(f) show for different d and (g)-(h) show for different D . (a), (c), (e) and (g) show trajectory radii r_t . (b), (d), (f) and (h) show the wobbling angle θ_{ax} . The acoustic field is turned on at $t = 6$ s and magnetic swimming is initiated at $t = 0$ s.

5.4 Acousto-magnetic Experiment Setup

The microswimmers used in the experiments are made out of AWG 40 NiCr wires (corresponding to wire diameter of $56 \mu\text{m}$, respectively). The wire is first wound on a drill tip with 0.5 mm diameter and then a 0.4 mm -diameter neodymium-iron-boron (NdFeB) magnet is attached at one end. Then a small layer of glue is applied to stick the magnet to the swimmer. After the glue dries out, the swimmer is pulled from its other end to form the helical tail. Several images of swimmers manufactured this way are shown at Fig. 5.5 and the geometric dimensions of the swimmers used

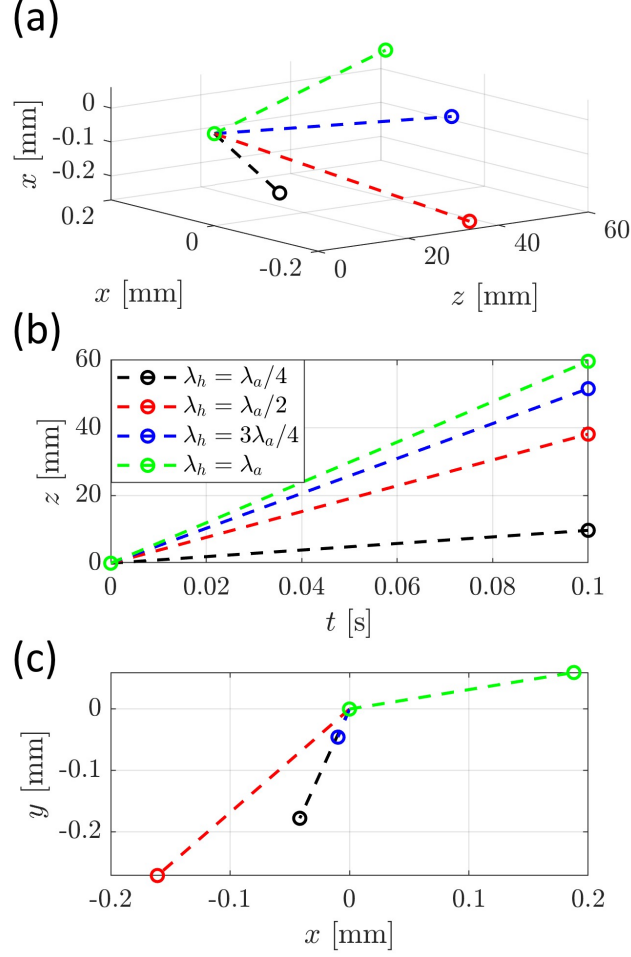


Figure 5.4 (a) Initial ($\mathbf{p} = [0 \ 0 \ 0]'$) and the final positions of helices with different wavelengths in 3-dimensional space under standing acoustic field. (b) Initial ($t = 0$ s) and final ($t = 0.1$ s) \mathbf{z} - coordinates of the same conditions. (c) Initial (0,0) and final radial coordinates of the same swimmers on x-y plane.

in experiments are given at Table 5.1. Note that this way of manufacturing causes variations in tail wavelength and other geometric dimensions but the variation is found to be around 10% at most.

The experiment setup is shown at Fig. 5.6a alongside with a schematic at Fig. 5.6b. The setup can be divided into three major parts: The first part is the magnetic actuation setup which consists of three orthogonally placed Helmholtz coils. The setup is described in detail in Section 3.3 and Caldag et al. (2017). For acoustomagnetic experiments, the driving field should be rotating around \mathbf{x} - axis (Refer to Fig. 5.7 for axes placement.). The rotating field is expressed as:

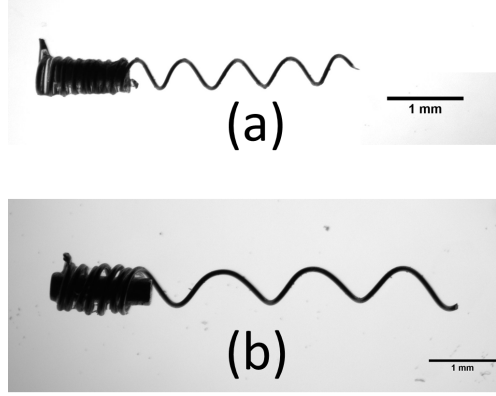


Figure 5.5 Two of the swimmers used in the experiments. Refer to Table 5.1 for geometric dimensions.

Property\Swimmer	(a)	(b)
Total length [mm]	5.73	5.94
Number of rotations (N_h)	4	3
Average wavelength [mm]	0.86	1.36
Average wave amplitude [mm]	0.55	0.5

Table 5.1 The geometric parameters of the swimmers in Fig. 5.5

$$(5.6) \quad \mathbf{B}_{drive} = B_0 \begin{bmatrix} 0 & \sin(\omega_m t) & \cos(\omega_m t) \end{bmatrix}'$$

The second major part of the setup is for acoustic actuation. The acoustic actuation setup consists of a signal generator (Agilent 33220a), a power amplifier (ENI A-150) and acoustic transducer (Olympus-branded, multiple models tested). The signal generator is connected to the computer and it is controlled from Matlab with Instrument Control Toolbox to send desired signal and turn on/off the output. The power amplifier is necessary as these transducers are generally driven at high voltages. The main mode of operation for these transducers is burst mode operation (where the signal is sent several times during a fixed period). There are certain limitations on excitation voltages and pulse duration to prevent transducer burnout. According to the manufacturer (Olympus, 2015), the power consumption should not exceed 125 mW. The maximum voltage that can be applied across the terminals is 300 V for a 10 MHz transducer. In order to calculate the necessary duty cycle, root mean square voltage is calculated from:

$$(5.7) \quad V_{rms} = (0.5)(0.707)V_{pp}$$

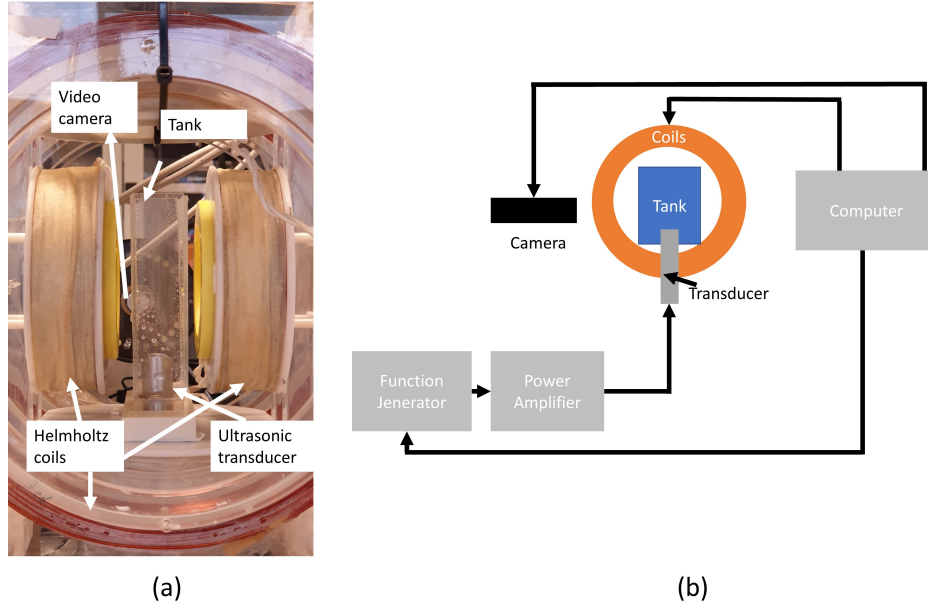


Figure 5.6 (a) A capture from the experiment setup. (b) Schematic of the setup.

where V_{pp} is the peak-to-peak voltage. Assuming a phase angle of 0 degrees (that all impedance is ohmic, which happens to be the worst case scenario in terms of power consumption), the duty cycle D_c is evaluated from:

$$(5.8) \quad D_c = \frac{Z P_{tot}}{V_{rms}^2}$$

where Z is the impedance and $P_{tot} = 125$ mW as recommended by the manufacturer. Assuming a 50Ω impedance, for 300 V excitation, the duty cycle comes out as 0.005 seconds. In burst mode, we should find the number of cycles (N) during a period. For a burst repetition rate of $f_{rep} = 5$ kHz N is found as:

$$(5.9) \quad N = f_a D_c f_{rep}$$

Here, f_a is the acoustic transducer operation frequency. The values of N for several different transducers used in the experiments are listed in Table 5.2. One also needs to determine the proper input voltage to the power amplifier to achieve the desired voltage. ENI A-150 amplifies the input signal by 55 dB, which corresponds to a 500-fold increase in voltage. According to the guidelines in Olympus (2015), the maximum applicable voltages and corresponding input voltages to the signal generator

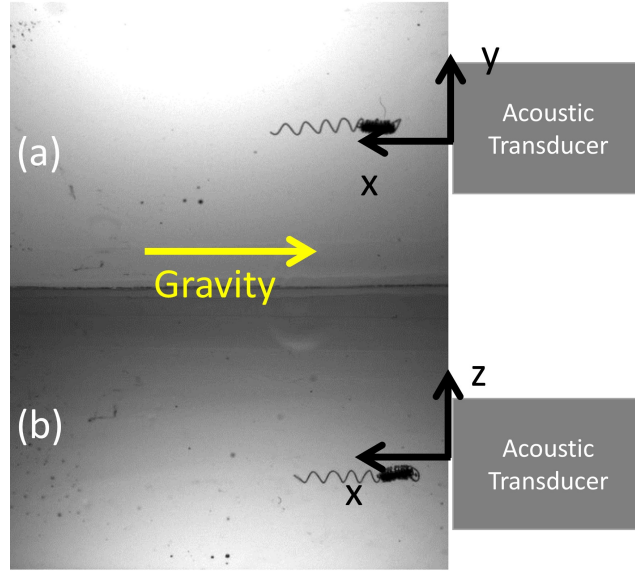


Figure 5.7 A capture from the experiment recordings. Camera directly captures (a) x-y plane image while a mirror placed with a 45-degree inclination captures (b) x-z plane image. Gravity is acting in -x direction.

Parameter\Transducer	V384-N-SU	A327-SU
Operating Frequency (f_a) [Hz]	3.5	10
Peak-to-peak Voltage (V_{pp}) [V]	200	300
Duty Cycle (D_c) [s]	0.005	0.005
Number of Cycles (N) []	5	3

Table 5.2 Operation parameters of the transducers.

are provided at Table 5.2. Two types of transducers are tested throughout the thesis research. The first transducer is a 3.5 MHz, Videoscan type unfocused transducer (Model V384-N-SU). Videoscan type transducers have highly damped response at a wide range of frequencies (Olympus, 2015). Wide-range frequency response was thought to be advantageous for testing the transducer at multiple frequencies but the results (shared at Section 5.5) show that the acoustic pressure remains low. In order to improve the applied pressure, the next transducer is selected as a 10-MHz Accuscan transducer with a cylindrical focus at 1-inch (2.54 cm) distance (Model A327-SU). Accuscan transducers give high response at its center frequency (Olympus, 2015). Higher frequency value and cylindrical focus are anticipated to result in higher acoustic forces.

The transducers are inserted from the bottom of a transparent tank made of plexiglass, as shown at Fig. 5.6. A cylindrical channel is inserted from the top that contains the transducer at the bottom. A mirror with a 45-degree inclination is placed next to the cylindrical channel in order to track position in 3 dimensions

(Refer to Fig. 5.7 for a capture from the recordings). The tank is placed vertically inside the setup such that the swimmer can be kept in a fixed (vertical) position relative to the transducer by balancing the swimmer thrust force (that propels the swimmer upwards) and gravitational force (that pulls the swimmer downwards). This setup also allows us to manipulate the setup much more easily, as the vertical setup has an opening along the tube's and the transducer's main axis. One disadvantage of this vertical setup is the linear dependence of swimming velocity with respect to position. As the swimmer gets out of the central region of Helmholtz coil setup, it slows down (discussed further below), albeit at a fixed rate. This will become much less of a problem considering that the experiments are carried out at narrow regions.

The third major component of the setup is the camera setup for recording the experiments. Initially, an off-brand USB camera was used to record the experiments. Later it is decided to improve the recording quality for reducing noise in data extraction. Basler ac-244075um camera is used in later experiments. The use of this camera brings multiple benefits: The camera can record at frame rates larger than 100 fps (compared to 30 fps of the previous camera). This camera can be controlled via Matlab as well, which allows for complete control of the experiments from a single interface. Refer to Section 5.4.1 for details on the custom interface and post-processing of experiment recordings.

5.4.1 Visual Interface and Image Processing

The experiment routine is carried out with a custom Matlab graphical user interface (GUI) for improving the repeatability of experiments and data processing. The GUI has the following features:

- **Helmholtz Coil Control:** The user can enter desired current amplitudes and profile of currents (sine or cosine waves) to the system. The signal can be amplified or shifted if necessary. The user needs to define frequencies in which the swimmer propels upwards, falls down and remains stationary (Required for position initialization process). The coils are controlled via Data Acquisition Toolbox of Matlab. Coil control is carried out before running the program or during START mode of the program (details below).
- **Position Initialization:** The position of the swimmer needs to be initialized properly in order to produce repeatable results in the experiments. Swim-

mer control through steering in Chapter 3 is incorporated here to move the swimmer to any initial position. The process from the user side is as following: The user inputs the desired 3D position into the interface and presses the INITIALIZE button on the GUI shown at Fig. 5.8. The algorithm then captures images subsequently with the camera used for recording the experiments and calculates the position error. According to the position error, the swimmer is tilted and/or sped up/slowed down to reach the desired position. When the swimmer reaches the desired position within a certain threshold, the algorithm waits for 5 iterations to check whether the swimmer remains stationary. If so, the INITIALIZE mode is halted and the software transitions into START mode in which the swimmer is rotated at a rate such that it is nearly stationary, ready for the experiment. Recording starts as soon as INITIALIZE mode is completed. After START mode is enabled, the user can activate ACOUSTIC mode from the interface.

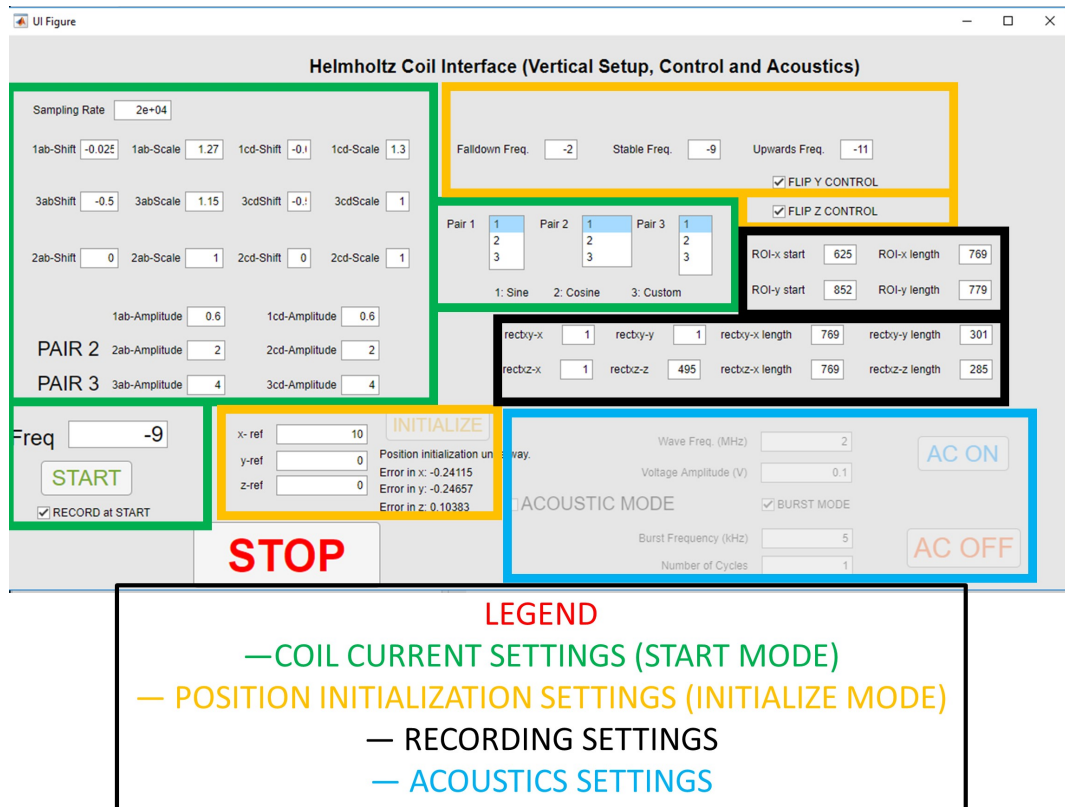


Figure 5.8 Graphical user interface developed in Matlab. The coils, the camera and the signal generator are all controlled from this interface. The caption was taken during INITIALIZE mode in which the swimmer is moved to reference position automatically. Refer to Fig. 5.7 for an example image from experiment recordings.

- **Position Estimation:** The position estimation through image processing relied on dark points on the image. The method was mostly satisfactory but it

was also susceptible to high noise from the surrounding objects and shadows. To improve image quality, the background of the recording environment is covered with a white plexiglass plate. The image processing is improved by introducing edge detection algorithms. Canny detection algorithm built in Matlab is used for edge detection. The resultant image is further processed by vertical and horizontal dilatations, bridging unconnected pixels, removing spur pixels (to reduce noisy pixels). The algorithm then filters out connected components based on major and minor axis lengths and total occupied area (the values are determined manually for each swimmer). The centroid of the rectangle that encapsulates the swimmer region is taken as the position of the swimmer at that instant. Several steps in image processing are demonstrated in Fig. 5.9 and the code for processing is given in the Appendix A.

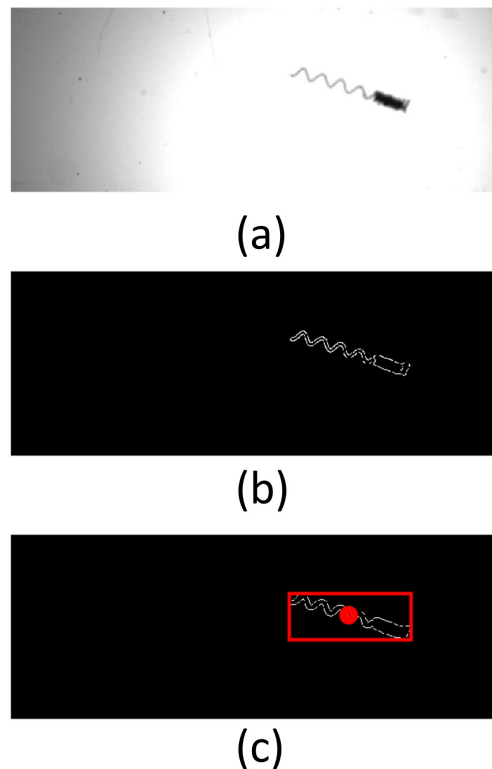


Figure 5.9 A caption from image processing. (a) The original image. (b) Image after edge detection and smoothing operations are applied. (c) Detected swimmer region (red rectangle) and its centroid (red circle).

- **Transducer Control:** The Agilent 33220a signal generator is connected to PC and controlled from the custom Matlab GUI via Instrument Control Toolbox. As shown at Fig. 5.8, the user can define the acoustic wave frequency, amplitude (to be multiplied by 50 at the power amplifier), whether the signal is a burst signal or not and the properties of the burst signal. By pressing

AC ON button, the transducer will start operating instantaneously. Control of each element on Matlab allows us to track the time of every change to the experiment setup (details are in the next item).

- **Experiment Recording:** Video recording is incorporated into Matlab as well through Image Acquisition Toolbox. This toolbox enables to preview and also record images from the camera. Furthermore, this setup allows us to save the instant the important events (such as acoustics turning on) occur with respect to the exact frame number of the video during recording. This log file is saved automatically after each experiment is concluded.

5.5 Acoustic Radiation Experiments

5.5.1 Experiments With the Unfocused Transducer

This subsection presents some of the experiment results with the unfocused transducer. A frame from the recorded images is shown at Fig. 5.7. The results here either show dimensional axial position (in \mathbf{x} - direction) or non-dimensional axial position (in \mathbf{x} - direction) (non-dimensionalized with the acoustic wavelength, λ_a) and velocity in the axial direction, u . Note that the origin is located at the tip of the transducer, so the axial position values imply the distances from the transducer tip. Note that the gravity is acting in $-\mathbf{x}$ direction in this configuration. Swimmer position is extracted with the image processing algorithm discussed in Section 5.4.1.

First, the repeatability of the results will be discussed. Fig. 5.10 shows the swimmer trajectory for a fixed $f_m = 10$ Hz without ultrasonic actuation. The experiments shown are carried out with 30-minute intervals in between each other. The results show that the swimmer is slowing down over time. The main contributor to this discrepancy is the variation in glycerol viscosity. There are two major factors that affects the viscosity, one being the temperature and the other being the humidity. According to Cheng (2008), a temperature change from 23 °C to 24 °C results in a 8.2% decrease in viscosity. Furthermore, when glycerine has 5% water in it, the viscosity drops more than 45% compared to a 100% glycerine fluid. Normally, the decrease in viscosity should not slow down the swimmer but the swimming

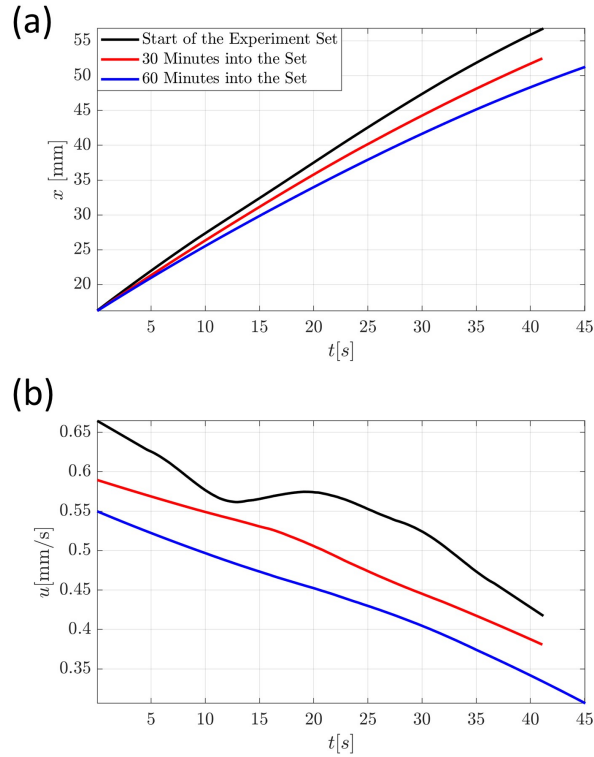


Figure 5.10 Swimmer trajectory without acoustic field and at a fixed $f_m = 10$ Hz at different times. (a) shows the axial position, (b) shows the velocity.

is not force-free due to gravity that's acting against the propulsion direction. As the gravitational force is a body force that does not depend on fluid viscosity, the decrease in viscosity increases the relative impact of the gravitational force, thus the swimmer experiences a slowdown. The FEM model in Chapter 2 is utilized with gravity added in the direction of propulsion to see the effect of viscosity on propulsion velocity for a swimmer similar to the one in experiments and the results are shown at Fig. 5.11. The decrease in swimming velocity with decreasing viscosity is apparent. Also note the decrease in velocity in Fig. 5.10 at all cases over time as the swimmer moves further away from the transducer. This occurs due to the decreasing magnetic field strength as the swimmer moves away from the center of the Helmholtz setup. Another key issue in the repeatability of the experiments is the initial swimmer position. While steering control is applied to start the swimmer from the same initial position, the swimmer in pusher-mode follows helical trajectories, so it was not possible to carry out experiments in the pusher-mode with repeatable results.

Fig. 5.12 shows the position of the swimmer in the puller mode under different acoustic actuation modes. The experiments are recorded one after another, so the change in viscosity is a non-issue. The operation frequency of the acoustic wave is

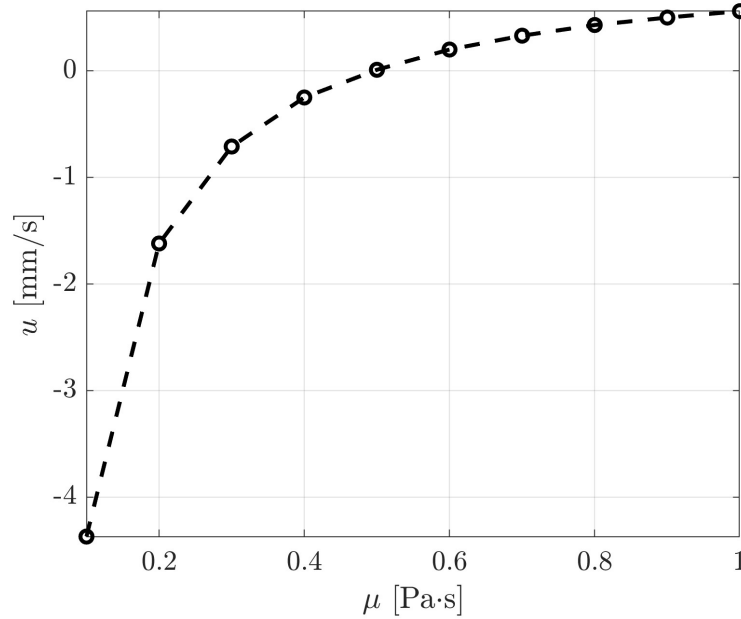


Figure 5.11 The change in u with respect to μ without acoustic field. Results are obtained from the FEM model in Chapter 2 with the gravity acting against the propulsion direction as in experiment setup (Corresponding to $+x$ direction in Fig. 2.1 and $-x$ direction in Fig. 5.7).

$f_a = 3.5$ MHz, the frequency with the maximum response. f_m is set to 18 Hz such that the swimmer is nearly stationary despite the fact that it is rotating when there is no acoustic actuation. When the swimmer is excited with a burst wave with an amplitude of 200 V, the swimmer starts falling down. On the other hand, when continuous acoustic waves with amplitudes of 20 and 40 V are applied, the swimmer is able to propel against the gravity, albeit at very low velocities. This test shows that the acoustic contribution to propulsion from the unfocused transducer is quite low.

This experiment configuration is tested with the simulation model described in Section 5.1 to understand why there is so little contribution. The hydrophone measurements reveal a p_a value of 130 kPa. 20 and 40 V of continuous acoustic actuation is assumed to result in a travelling field even though the actual field would not be a perfect travelling wave due to scattering and reflections inside the tank and the tube. Simulations are carried out at multiple μ values over a wide range of p_a values, with the results displayed at Fig. 5.13. The viscosity of 90% pure glycerine falls down as low as 0.2 Pa·s at 25 °C (Cheng, 2008), so the μ values selected here represent slightly humid glycerine. The values from the simulations come in close proximity of the experiment results and verify the experimental observations. Taken together with the results in Chapter 4, it appears that the viscosity significantly dampens

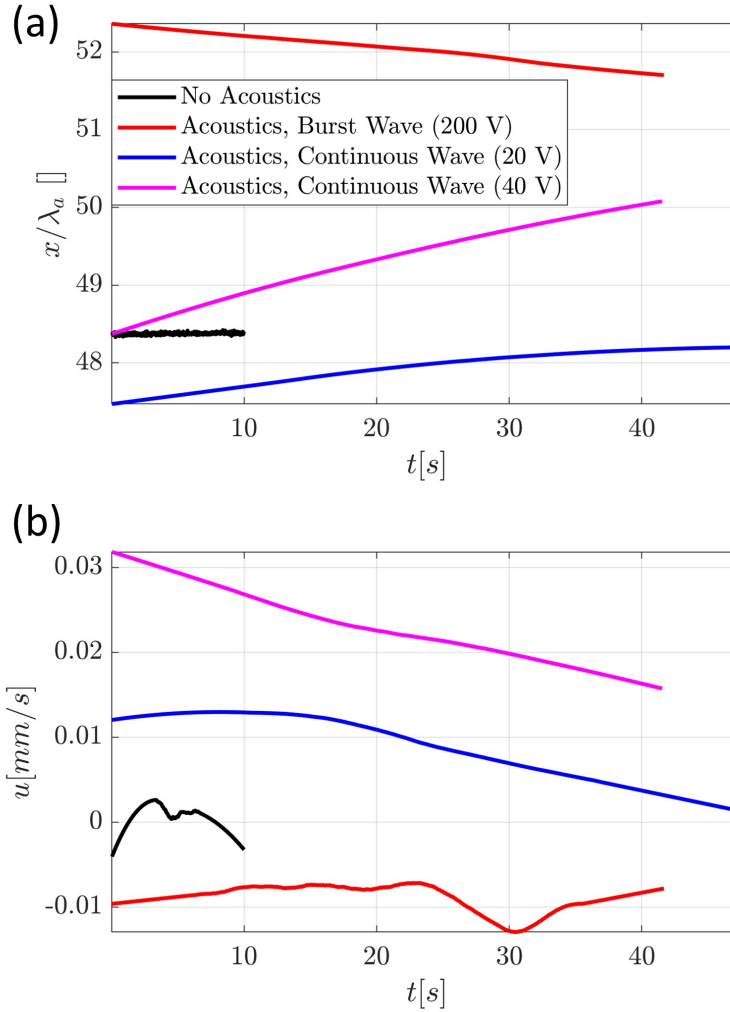


Figure 5.12 Swimmer (a) position and (b) velocity at $f_m = 18$ Hz under different modes of acoustic actuation.

the pressure wave and prevents us to see any notable improvement in propulsion velocity.

The main mode of operation for the transducer is burst mode, so further experiments are carried out with this waveform. Fig. 5.14 shows the swimmer trajectories and velocities under different acoustic wave frequencies, ranging from 2 MHz to 5 MHz at 50 V and 200 V of transducer voltages, corresponding to $p_a = 162.5$ and 650 kPa. The propulsion is hindered at all frequency values at both 50 and 200 V. The velocity values when the voltage is 50 V are quite close to each other. When the voltage is 200 V, the rates of slowdown at different f_a remain distinct. The slowdown when the voltage is 200 V is the lowest at $f_a = 3.5$ MHz. These results are in stark contrast with the observations in the simulations where the travelling waves always contribute to the propulsion velocity, so the results here remain inconclusive.

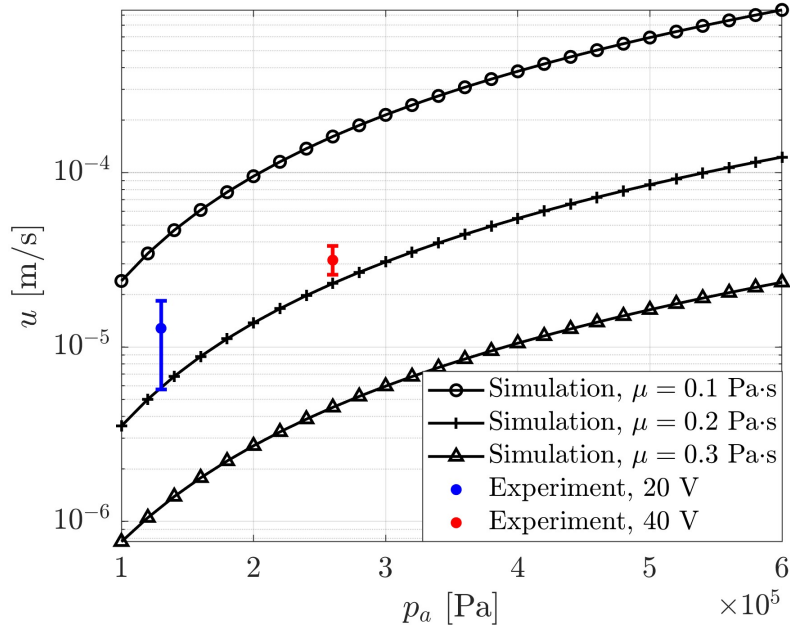


Figure 5.13 Comparison of experiment results in Fig. 5.12 with the simulation results obtained with the model in Section 5.1. The error bars represent the variation in the results in Fig. 5.12.

5.5.2 Experiments with the Focused Transducer

A focused transducer helps in focusing a significant amount of acoustic pressure to a narrow region, thereby helping to observe the effects of acoustic radiation much more clearly. The focus of the transducer is 2.54 cm away from the surface. This focal distance is represented with a black line in the following velocity plot.

One of the initial tests consists of rotating the swimmer slowly such that it is not able to overcome the gravity and fall down. The test is repeated with acoustic field on and off. $f_a = 10$ MHz and the voltage amplitude is 300 V. Fig. 5.15 shows that the swimmer in both cases start out with similar velocities. However, as the swimmer under acoustic field gets closer to the focal region, it starts slowing down. This plot also shows the extent of the region that the transducer is effective, around 1.5 times the focal distance.

Several other experiments are carried out with the focused transducer with no significant results observed in the propulsion velocity. It is understood that both the high operating frequency and the viscosity of the liquid lead to very low radiation force that is basically not observable when the propulsion velocity is significantly large.

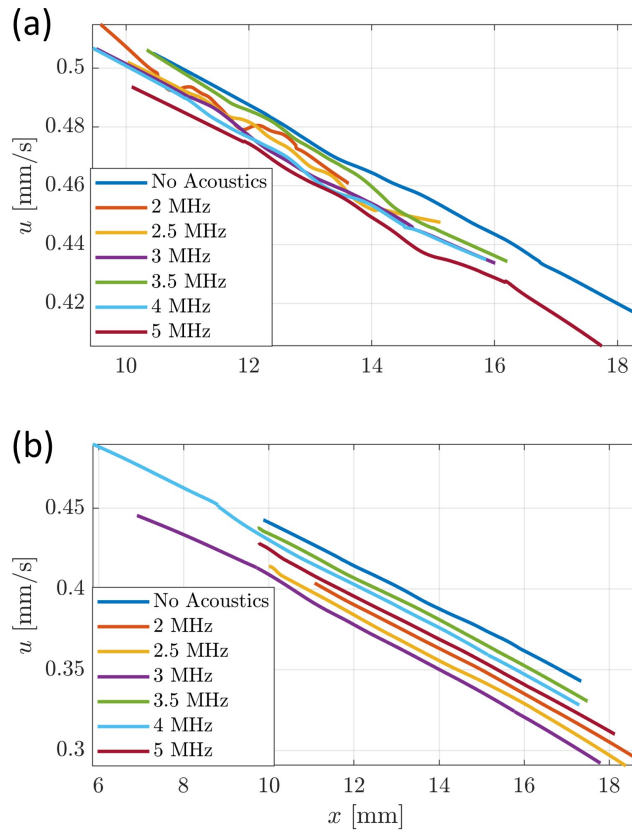


Figure 5.14 u of the swimmer with respect to axial position at (a) 50 V and (b) 200 V.

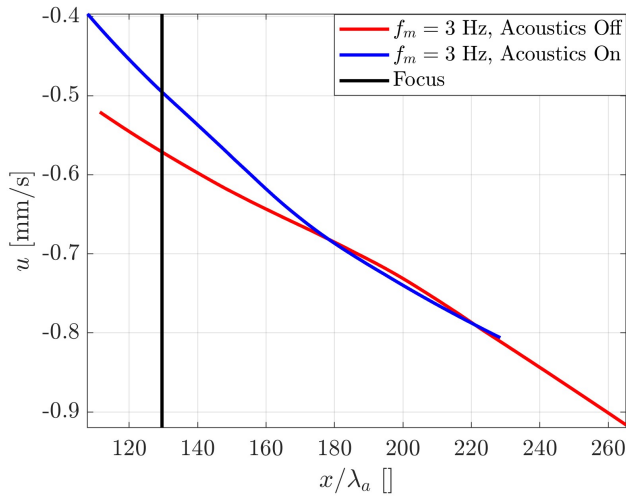


Figure 5.15 Swimmer velocity during falldown at $f_m = 3$ Hz with and without acoustic excitation. The transducer is the focused one and operates at its maximum response frequency, $f_a = 10$ MHz.

6. Conclusion

Artificial helical microswimmers are hugely prospective agents for the manipulation in fluid environments at small scales. Most of the potential application areas are within a biomedical context where accurate swimmer control and navigation are critical. This dissertation takes magnetized helical swimmers, one of the most commonly used type in the literature, in its focus and attempts to characterize and resolve the oscillatory nature of swimming trajectories. The dissertation first presents an extensive discussion on oscillatory trajectories of magnetized helical swimmers in confined environments. Pusher-mode instability, which is different from other modes of instability such as wobbling and step-out, is reported and characterized in detail with the help of a novel simulation methodology in which snap-shot FEM solutions of Stokes equations are integrated using kinematic equations to obtain complete 3-dimensional trajectories. Distinctive pusher-mode and puller-mode trajectories, observed previously in experiments, are replicated with high accuracy in the simulations. Despite the time-reversible nature of any instant of the pusher-mode and the puller-mode swimming for a certain position and orientation, as the swimmers move in opposite directions, the trajectories change. As the Mason number increases, the pitching angle of the pushers increases whereas the wobbling angle of helical swimmer decreases in bulk swimming. This result indicates that the hydrodynamic interactions with the wall play an important role in the trajectories of confined swimmers at high Mason numbers. Moreover, a further increase in the Mason number leads to a gradual transition to step-out as the pitching angle increases further, especially for pullers, as the tip of the tail makes a wider circle than the head, which remains close to the center-line. The effects of the confinement can be characterized by the ratio of diameters of the head and the channel.

Helical pusher-mode trajectories prevent controlled navigation of the swimmers. A novel proportional control algorithm based on magnetic steering is utilized to suppress oscillatory trajectories. State-of-the art methods rely on both swimmer position and orientation to successfully steer the swimmer to the desired path. However, considering the medical applications in which no visual contact with the swimmer is

possible, even obtaining accurate swimmer position information is challenging, thus, these approaches are not feasible in future use cases. A feedback control algorithm that is solely based on swimmer position is introduced here and Lyapunov stability is demonstrated for a constant reference path for low wobbling angles. The control law is demonstrated both experimentally and with the kinematic model used for investigating the pusher-mode instability. In addition to these, the resistance matrix for helical swimming in bulk fluid available in the literature is simplified and a swirling flow representation is added on top to simulate in-channel swimming. In all studies, oscillatory pusher-mode trajectories are suppressed significantly. In simulations, it is shown that the algorithm is capable of making the swimmer follow a time-varying path as well. As the confinement increases the viscous effects, the proposed method is particularly useful in highly viscous environments. The extension of the framework to 3D path following and reduction in the response time of the control algorithm in experiments constitute the future work. This approach is expected to be adoptable for practical applications.

Suppressing the oscillatory trajectories is also possible by introducing passive mechanisms to the system without a need for any kind of feedback. The dissertation proposes acoustic fields on top of magnetic actuation for improving swimmer stability as acoustic fields are biocompatible and widely adopted in medical applications. A novel and computationally efficient way of calculating the radiation force on helices, called chain-of-spheres approach, is verified with a finite-element model that is computationally very expensive. A slender helical tail is treated as a chain of spheres for which analytical expressions for the acoustic radiation force are well-known. By summing up the forces on each sphere, the total radiation force and torque on the helix can be found with reasonable accuracy in comparison to finite-element results. The method achieves very high accuracy if the acoustophoretic contrast factor remains low. The chain-of-spheres approach dramatically reduces the computational cost compared to the FEM model, especially for swimmers with dimensions on the order of an acoustic wavelength.

The chain-of-spheres approach is incorporated in the resistive force theory-based model to evaluate the trajectories of magnetically actuated helical swimmers in acoustic fields. First, it is shown that swimmer wobbling is reduced under traveling acoustic waves with a significant increase in the propulsion velocity. Secondly, standing fields are found to stabilize the swimmers in unique fixed positions based on their geometric parameters. This can be utilized for keeping the swimmer stationary in micro-mixing applications. The relation between the swimmer geometry and acoustic field is investigated with several parametric studies. An experiment setup for acousto-magnetic propulsion of magnetized helical swimmers is realized

with a magnetic coil setup and multiple acoustic transducers. The acoustic contribution to swimmer propulsion remains low and the simulations show that this is due to high viscosity of the glycerine. It appears that one has to go to slightly smaller scales (in terms of swimmer geometry) and significantly less viscous fluids to fully benefit from the acoustic radiation. Overall, the findings of this thesis are expected to improve the understanding on the oscillatory trajectories of magnetized helical swimmers and help in suppressing the oscillatory trajectories to enable controlled navigation in biomedical applications.

6.1 Future Work

Characterizing the pusher-mode instability requires further studies. A more rigorous analysis on the flow fields caused by the pusher-mode and the puller-mode swimmer would enlighten why the trajectories evolve differently over time. Based on the studies in the literature, the key point to demonstrate in explaining the pusher-mode instability lies in the motion of the fluid that surrounds the swimmer. It was found in this dissertation that the solutions for a certain position and orientation of the swimmer are exactly reversible in the pusher and the puller-mode swimming but the flow fields over time should be followed to demonstrate how the pusher-mode instability occurs. Additionally, it is very important to distinguish the wobbling dynamics from the pusher-mode instability, as discussed in the dissertation. At this point, straight trajectories in the puller-mode swimming imply that the wobbling should be minimal. Here, one should identify the role of the head carefully. The head is the source of the oscillatory trajectories in the pusher-mode while it is demonstrated here that it slightly suppresses the oscillations due to wobbling in bulk swimming conditions. In other words, the head suppresses the wobbling that is solely caused by the helical geometry of the tail in bulk swimming conditions but it also leads to the pusher-mode instability in confinement. Characterization of the trajectories both in terms of the wobbling and the pusher-mode instability is critical to be able to understand and distinguish the underlying reasons behind each mode of instability. This may require additional experiments and simulations with swimmers without a head and in bulk swimming conditions. The experiments used in verifying the simulation results lack some details about the setup such as the Mason number. The knowledge of these details would allow a direct comparison between the experiments and the simulations.

The scope of the experiments and the simulations for the pusher-mode instability can be expanded with additional tests such as testing multiple swimmers, swimming in immiscible fluids and non-Newtonian fluids. The interactions of the swirling flow fields generated by a swarm of the swimmers can lead to swimmers not only oscillating around their major rotation axis due to the wobbling, but also lead them to trace a larger oscillatory path at the same time. Immiscible fluids with different material properties will directly affect the Ma and that will lead to trajectories with varying amplitudes. The effect of changing density will manifest itself in the buoyancy force acting on the swimmer, this will be particularly important at low rotation rates of the swimmer where the gravity becomes non-negligible. Swimming in non-Newtonian fluids is another complicated problem in which the swimming dynamics will change based on the rotation frequency of the swimmer. For shear-thickening fluids, the trajectories may start out very oscillatory at low rotation rates and then become very stable at large rotation rates whereas for shear-thinning fluids it will be vice versa. For shear-thinning fluids, the Mason number will decrease as the rotation rate increases, implying that the trajectories will be oscillatory at larger rotation rates. On the other hand, low rotation rates is another source of instability for the swimmers so the swimmer trajectories may be oscillatory for all rotation rates of the swimmer.

Magnetic steering control can be tested experimentally in more advanced scenarios. The swimmer could be navigated in complex 3-dimensional environments such as a phantom vascular network. Furthermore, the methodology is open to incorporate navigation in 3-dimensional space where the coils that drive the swimmer could be altered altogether to enable motion in any direction. The effects of large proportional control gains on the swimmer trajectories are not studied experimentally, this should be investigated further as well. Controlling a swarm of the swimmers is also an important and practically relevant task that can be tested with the approach proposed in the model. The additional studies mentioned above for investigating the pusher-mode instability constitute additional case studies for the control law. It would be quite significant to achieve controlled navigation in non-Newtonian fluids with this methodology as non-Newtonian fluids bring physical instability to the system.

The numerical models on helical swimmers presented here, both the resistive force theory model and the kinematic model, can be utilized in developing a predictive tool for the swimmer trajectories. Running simulations over a wide range of geometric and physical parameters can be fed to a machine learning algorithm that may help in predicting the exact swimmer position and orientation at a certain time. That would enable realizing an offline control algorithm that can predict the swimmer position

and provide the necessary input to suppress the oscillatory trajectories or steer the swimmer to the desired path. Considering that the image processing duration is one of the biggest restrictions in supplying timely control input to the system, such a predictive model could demonstrate the true performance of the control law.

The chain-of-spheres approach to predict the radiation force can be improved further. One aspect is verifying the algorithm in terms of the travelling waves, as the verification in the dissertation only covers standing wave results. One big omission in comparison to the experiments is that the approach doesn't take a head structure into the account that exists in the swimmers used in the experiments. Considering that the head size is very large, it is going to affect the distribution of the force acting on the swimmer significantly. Looking from a volumetric perspective, the existence of the head should increase the radiation force acting on the swimmer. However, the head, purely due to its size, will significantly affect the scattered field distribution. The scattered field magnitude may become so high that the chain-of-spheres approach may not be valid any more. Different effects may arise depending on whether the tail is shadowed by the head or not. While the helix is a symmetric structure, the addition of the head brings asymmetry. Furthermore, the addition of the head results in the head being the dominant structure that determines the radiation force acting on the swimmer. That may lead to a simplification in the modelling by only accounting for the head in the calculation of the radiation force.

The usage of acoustic fields by itself bring about some other possible problems. The first issue to consider is the practical possibility of realizing travelling or standing waves in *in vivo* environments. Living organisms consist of layers of tissues, arteries and organs, each with a different acoustic impedance. That would significantly affect the wave profile and cause a significant amount of scattering. Usage of other kinds of acoustic fields may be required to successfully achieve acoustic manipulation. Another issue to consider is the heating due to the acoustic waves. The acoustic waves are known to cause heat dissipation and the change in the temperature of the system can change a majority of the physical parameters of the medium such as the viscosity and speed of sound. Lastly, studying the acoustic waves under non-Newtonian fluids is practically relevant as some of the body tissues exhibit non-Newtonian behavior. The viscosity affects the acoustic manipulation in two ways. One is the attenuation of the wave amplitude while the other one is on-body due to viscous boundary layer formation. Non-Newtonian fluids would cause an irregular pressure profile and dynamic viscous boundary layer thickness that need specialized modelling tools to observe how the dynamic nature of the system affects the swimming trajectories under acousto-magnetic actuation.

The dissertation covers the acoustic radiation force effects on helical swimmers. The results show that the radiation force effects are negligibly low as the swimmer scale goes in μm range. That means different means of acoustic manipulation may be necessary at lower scales. Examples include focused beams, surface acoustic waves and bulk acoustic waves. It is noted in the literature that the viscous boundary layer thicknesses are quite low for the range of parameters tested in the dissertation, but going to the lower scales mean that the viscous boundary layer becomes significant. These different ways of acoustic manipulation may be practically more relevant in medical scenarios.

BIBLIOGRAPHY

- Abbott, J. J., Peyer, K. E., Lagomarsino, M. C., Zhang, L., Dong, L., Kaliakatsos, I. K., & Nelson, B. J. (2009). How should microrobots swim? *The International Journal of Robotics Research*, 28(11-12), 1434–1447.
- Acemoglu, A. & Yesilyurt, S. (2014). Effects of geometric parameters on swimming of micro organisms with single helical flagellum in circular channels. *Biophysical Journal*, 106(7), 1537–1547.
- Acemoglu, A. & Yesilyurt, S. (2015). Effects of poiseuille flows on swimming of magnetic helical robots in circular channels. *Microfluidics and Nanofluidics*, 19(5), 1109–1122.
- Ahmed, D., Baasch, T., Jang, B., Pane, S., Dual, J., & Nelson, B. J. (2016). Artificial swimmers propelled by acoustically activated flagella. *Nano Letters*, 16(8), 4968–4974.
- Ahmed, D., Lu, M., Nourhani, A., Lammert, P. E., Stratton, Z., Muddana, H. S., Crespi, V. H., & Huang, T. J. (2015). Selectively manipulable acoustic-powered microswimmers. *Scientific Reports*, 5, 9744.
- Ahmed, S., Wang, W., Bai, L., Gentekos, D. T., Hoyos, M., & Mallouk, T. E. (2016). Density and shape effects in the acoustic propulsion of bimetallic nanorod motors. *ACS Nano*, 10(4), 4763–4769.
- Ahmed, S., Wang, W., Mair, L. O., Fraleigh, R. D., Li, S., Castro, L. A., Hoyos, M., Huang, T. J., & Mallouk, T. E. (2013). Steering acoustically propelled nanowire motors toward cells in a biologically compatible environment using magnetic fields. *Langmuir*, 29(52), 16113–16118.
- Alt, W. & Hoffmann, G. (2013). *Biological Motion: Proceedings of a Workshop Held in Königswinter, Germany, March 16–19, 1989*, volume 89. Springer Science & Business Media.
- Baasch, T., Leibacher, I., & Dual, J. (2017). Multibody dynamics in acoustophoresis. *The Journal of the Acoustical Society of America*, 141(3), 1664–1674.
- Berg, H. C. & Turner, L. (1990). Chemotaxis of bacteria in glass capillary arrays. escherichia coli, motility, microchannel plate, and light scattering. *Biophysical Journal*, 58(4), 919–930.
- Berke, A. P., Turner, L., Berg, H. C., & Lauga, E. (2008). Hydrodynamic attraction of swimming microorganisms by surfaces. *Physical Review Letters*, 101(3), 038102.
- Bruus, H. (2012). Acoustofluidics 7: The acoustic radiation force on small particles. *Lab on a Chip*, 12(6), 1014–1021.
- Caldag, H. O., Acemoglu, A., & Yesilyurt, S. (2017). Experimental characterization of helical swimming trajectories in circular channels. *Microfluidics and Nanofluidics*, 21(8), 136.
- Caldag, H. O. & Yesilyurt, S. (2019). Trajectories of magnetically-actuated helical swimmers in cylindrical channels at low reynolds numbers. *Journal of Fluids and Structures*, 90, 164–176.
- Ceylan, H., Yasa, I. C., Yasa, O., Tabak, A. F., Giltinan, J., & Sitti, M. (2019). 3d-printed biodegradable microswimmer for theranostic cargo delivery and release. *ACS Nano*, 13(3), 3353–3362.

- Chacón, R. (2013). Chaotic dynamics of a microswimmer in poiseuille flow. *Physical Review E*, 88(5), 052905.
- Cheng, N.-S. (2008). Formula for the viscosity of a glycerol- water mixture. *Industrial & Engineering Chemistry Research*, 47(9), 3285–3288.
- Collino, R. R., Ray, T. R., Fleming, R. C., Sasaki, C. H., Haj-Hariri, H., & Begley, M. R. (2015). Acoustic field controlled patterning and assembly of anisotropic particles. *Extreme Mechanics Letters*, 5, 37–46.
- de Graaf, J., Mathijssen, A. J., Fabritius, M., Menke, H., Holm, C., & Shendruk, T. N. (2016). Understanding the onset of oscillatory swimming in microchannels. *Soft Matter*, 12(21), 4704–4708.
- Doinikov, A. A. (2003). Acoustic radiation forces: Classical theory and recent advances. *Recent Research Developments in Acoustics*, 1, 39–67.
- Dreyfus, R., Baudry, J., Roper, M. L., Fermigier, M., Stone, H. A., & Bibette, J. (2005). Microscopic artificial swimmers. *Nature*, 437(7060), 862–865.
- Feng, J., Yuan, J., & Cho, S. K. (2015). Micropropulsion by an acoustic bubble for navigating microfluidic spaces. *Lab on a Chip*, 15(6), 1554–1562.
- Galajda, P., Keymer, J., Chaikin, P., & Austin, R. (2007). A wall of funnels concentrates swimming bacteria. *Journal of Bacteriology*, 189(23), 8704–8707.
- Garbin, A., Leibacher, I., Hahn, P., Le Ferrand, H., Studart, A., & Dual, J. (2015). Acoustophoresis of disk-shaped microparticles: A numerical and experimental study of acoustic radiation forces and torques. *The Journal of the Acoustical Society of America*, 138(5), 2759–2769.
- Ghosh, A. & Fischer, P. (2009). Controlled propulsion of artificial magnetic nanostructured propellers. *Nano Letters*, 9(6), 2243–2245.
- Glynne-Jones, P., Mishra, P. P., Boltryk, R. J., & Hill, M. (2013). Efficient finite element modeling of radiation forces on elastic particles of arbitrary size and geometry. *The Journal of the Acoustical Society of America*, 133(4), 1885–1893.
- Gray, J. & Hancock, G. (1955). The propulsion of sea-urchin spermatozoa. *Journal of Experimental Biology*, 32(4), 802–814.
- Hasegawa, T. (1977). Comparison of two solutions for acoustic radiation pressure on a sphere. *The Journal of the Acoustical Society of America*, 61(6), 1445–1448.
- Hasegawa, T. (1979). Acoustic radiation force on a sphere in a quasistationary wave field—theory. *The Journal of the Acoustical Society of America*, 65(1), 32–40.
- Hasegawa, T., Saka, K., Inoue, N., & Matsuzawa, K. (1988). Acoustic radiation force experienced by a solid cylinder in a plane progressive sound field. *The Journal of the Acoustical Society of America*, 83(5), 1770–1775.
- Hasegawa, T. & Yosioka, K. (1969). Acoustic-radiation force on a solid elastic sphere. *The Journal of the Acoustical Society of America*, 46(5B), 1139–1143.
- Haydock, D. (2005). Calculation of the radiation force on a cylinder in a standing wave acoustic field. *Journal of Physics A: Mathematical and General*, 38(15), 3279.
- Hyon, Y., Powers, T. R., Stocker, R., Fu, H. C., et al. (2012). The wiggling trajectories of bacteria. *Journal of Fluid Mechanics*, 705, 58—76.
- Ishimoto, K. & Gaffney, E. A. (2013). Squirmer dynamics near a boundary. *Physical Review E*, 88(6), 062702.
- Kaynak, M., Ozcelik, A., Nourhani, A., Lammert, P. E., Crespi, V. H., & Huang, T. J. (2017). Acoustic actuation of bioinspired microswimmers. *Lab on a Chip*,

- 17(3), 395–400.
- King, L. V. (1934). On the acoustic radiation pressure on spheres. *Proceedings of the Royal Society of London. Series A-Mathematical and Physical Sciences*, 147(861), 212–240.
- Klindt, G. S. & Friedrich, B. M. (2015). Flagellar swimmers oscillate between pusher-and puller-type swimming. *Physical Review E*, 92(6), 063019.
- Lauga, E. (2016). Bacterial hydrodynamics. *Annual Review of Fluid Mechanics*, 48, 105–130.
- Lauga, E., DiLuzio, W. R., Whitesides, G. M., & Stone, H. A. (2006). Swimming in circles: motion of bacteria near solid boundaries. *Biophysical Journal*, 90(2), 400–412.
- Leclerc, J., Zhao, H., & Becker, A. T. (2019). 3d control of rotating millimeter-scale swimmers through obstacles. In *2019 International Conference on Robotics and Automation (ICRA)*, (pp. 8890–8896). IEEE.
- Li, J., Li, T., Xu, T., Kiristi, M., Liu, W., Wu, Z., & Wang, J. (2015). Magneto-acoustic hybrid nanomotor. *Nano Letters*, 15(7), 4814–4821.
- Lighthill, J. (1976). Flagellar hydrodynamics. *SIAM Review*, 18(2), 161–230.
- Liu, B., Breuer, K. S., & Powers, T. R. (2014). Propulsion by a helical flagellum in a capillary tube. *Physics of Fluids*, 26(1), 011701.
- Louf, J.-F., Bertin, N., Dollet, B., Stephan, O., & Marmottant, P. (2018). Hovering microswimmers exhibit ultrafast motion to navigate under acoustic forces. *Advanced Materials Interfaces*, 5(16), 1800425.
- Maidanik, G. & Westervelt, P. (1957). Acoustical radiation pressure due to incident plane progressive waves on spherical objects. *The Journal of the Acoustical Society of America*, 29(8), 936–940.
- Man, Y. & Lauga, E. (2013). The wobbling-to-swimming transition of rotated helices. *Physics of Fluids*, 25(7), 071904.
- Martel, S. (2013). Microrobotics in the vascular network: present status and next challenges. *Journal of Micro-Bio Robotics*, 8(1), 41–52.
- Mitri, F. (2005). Theoretical calculation of the modulated acoustic radiation force on spheres and cylinders in a standing plane wave-field. *Physica D: Nonlinear Phenomena*, 212(1-2), 66–81.
- Muller, P. B., Barnkob, R., Jensen, M. J. H., & Bruus, H. (2012). A numerical study of microparticle acoustophoresis driven by acoustic radiation forces and streaming-induced drag forces. *Lab on a Chip*, 12(22), 4617–4627.
- Olympus (2015). Conventional ultrasonic transducers.
- Oulmas, A., Andreff, N., & Régnier, S. (2018). 3d closed-loop swimming at low reynolds numbers. *The International Journal of Robotics Research*, 37(11), 1359–1375.
- Palagi, S., Mark, A. G., Reigh, S. Y., Melde, K., Qiu, T., Zeng, H., Parmeggiani, C., Martella, D., Sanchez-Castillo, A., Kapernaum, N., et al. (2016). Structured light enables biomimetic swimming and versatile locomotion of photoresponsive soft microrobots. *Nature Materials*, 15(6), 647–653.
- Peters, C., Hoop, M., Pané, S., Nelson, B. J., & Hierold, C. (2016). Degradable magnetic composites for minimally invasive interventions: Device fabrication, targeted drug delivery, and cytotoxicity tests. *Advanced Materials*, 28(3), 533–538.

- Petersson, F., Åberg, L., Swård-Nilsson, A.-M., & Laurell, T. (2007). Free flow acoustophoresis: microfluidic-based mode of particle and cell separation. *Analytical Chemistry*, *79*(14), 5117–5123.
- Peyer, K. E., Zhang, L., Kratochvil, B. E., & Nelson, B. J. (2010). Non-ideal swimming of artificial bacterial flagella near a surface. In *2010 IEEE International Conference on Robotics and Automation*, (pp. 96–101). IEEE.
- Purcell, E. M. (1977). Life at low reynolds number. *American Journal of Physics*, *45*(1), 3–11.
- Ren, L., Nama, N., McNeill, J. M., Soto, F., Yan, Z., Liu, W., Wang, W., Wang, J., & Mallouk, T. E. (2019). 3d steerable, acoustically powered microswimmers for single-particle manipulation. *Science Advances*, *5*(10), eaax3084.
- Settnes, M. & Bruus, H. (2012). Forces acting on a small particle in an acoustical field in a viscous fluid. *Physical Review E*, *85*(1), 016327.
- Silva, G. T. & Drinkwater, B. W. (2018). Acoustic radiation force exerted on a small spheroidal rigid particle by a beam of arbitrary wavefront: Examples of traveling and standing plane waves. *The Journal of the Acoustical Society of America*, *144*(5), EL453–EL459.
- Spagnolie, S. E. & Lauga, E. (2012). Hydrodynamics of self-propulsion near a boundary: predictions and accuracy of far-field approximations. *arXiv preprint arXiv:1211.6996*.
- Takatori, S. C., De Dier, R., Vermant, J., & Brady, J. F. (2016). Acoustic trapping of active matter. *Nature Communications*, *7*(1), 1–7.
- Tottori, S., Zhang, L., Qiu, F., Krawczyk, K. K., Franco-Obregón, A., & Nelson, B. J. (2012). Magnetic helical micromachines: fabrication, controlled swimming, and cargo transport. *Advanced Materials*, *24*(6), 811–816.
- Wang, C. W., Perez, M. J., Helmke, B. P., Viola, F., & Lawrence, M. B. (2015). Integration of acoustic radiation force and optical imaging for blood plasma clot stiffness measurement. *PloS One*, *10*(6).
- Wang, J. & Dual, J. (2009). Numerical simulations for the time-averaged acoustic forces acting on rigid cylinders in ideal and viscous fluids. *Journal of Physics A: Mathematical and Theoretical*, *42*(28), 285502.
- Wang, J. & Dual, J. (2011). Theoretical and numerical calculations for the time-averaged acoustic force and torque acting on a rigid cylinder of arbitrary size in a low viscosity fluid. *The Journal of the Acoustical Society of America*, *129*(6), 3490–3501.
- Wang, S. & Ardekani, A. (2012). Unsteady swimming of small organisms. *Journal of Fluid Mechanics*, *702*, 286.
- Wang, W., Castro, L. A., Hoyos, M., & Mallouk, T. E. (2012). Autonomous motion of metallic microrods propelled by ultrasound. *ACS Nano*, *6*(7), 6122–6132.
- Wang, W., Li, S., Mair, L., Ahmed, S., Huang, T. J., & Mallouk, T. E. (2014). Acoustic propulsion of nanorod motors inside living cells. *Angewandte Chemie International Edition*, *53*(12), 3201–3204.
- Wijaya, F. B. & Lim, K.-M. (2015). Numerical calculation of acoustic radiation force and torque acting on rigid non-spherical particles. *Acta Acustica united with Acustica*, *101*(3), 531–542.
- Xuan, M., Shao, J., Lin, X., Dai, L., & He, Q. (2014). Self-propelled janus mesoporous silica nanomotors with sub-100 nm diameters for drug encapsulation and delivery. *ChemPhysChem*, *15*(11), 2255–2260.

- Zhang, L., Abbott, J. J., Dong, L., Kratochvil, B. E., Bell, D., & Nelson, B. J. (2009). Artificial bacterial flagella: Fabrication and magnetic control. *Applied Physics Letters*, *94*(6), 064107.
- Zhu, L., Lauga, E., & Brandt, L. (2013). Low-reynolds number swimming in a capillary tube. *arXiv preprint arXiv:1304.7671*.
- Zöttl, A. & Stark, H. (2012). Nonlinear dynamics of a microswimmer in poiseuille flow. *Physical Review Letters*, *108*(21), 218104.

APPENDIX A

Matlab Code for Image Processing

The code below shows the image processing routine on x-y plane image of an experiment video. For image processing in x-z plane, it is sufficient to change line 34 in the code to "rect=rectxz;".

```
1 clearvars;close all;clc;
2
3 rectxy=[1 1 575 284]+[0 0 0 0]; %Image region for data ...
   extraction in x-y plane
4 rectxz=[1 476 575 264]+[0 0 0 0]; %Image region for data ...
   extraction in x-z plane
5
6 orlimitxy=0.4; %Canny edge detection threshold parameter, x-y plane
7 orlimitxz=0.4; %Canny edge detection threshold parameter, x-z plane
8 upl=0.0317; %Unit pixel length, determined manually from the images
9
10 minorax_min=15;
11 minorax_max=50;
12 majorax_min=150;
13 majorax_max=250; %The range of side lengths of the rectangle ...
   that encompasses the swimmer
14 refarea=7200; %Reference value for the rectangle area
15
16 gd=dir('C:\Users\hakancaldag\Desktop\Image Processing\Videos\'); ...
   %Obtain names of the video files in the directory
17
18 for ii=1:length(gd)
19     fn=gd(ii).name %Obtain the name
20     videonames{ii}=fn; %Attach the name to a cell array
21 end
22 address='C:\Users\hakancaldag\Desktop\Image Processing\Videos\'; ...
   %The address the video file is stored in
23
24 for ii=1:length(videonames) %Processing all the videos in the loop
25
26     videoname=videonames{ii};
27
28     swimmerObj = VideoReader(strcat([address videoname])); % ...
   Video name
```

```

29     frames = read(swimmerObj); %Read video and save the frames ...
        in variable "frames"
30     k1 = 1; % Starting frame
31     a=size(frames);
32     k2 = a(4); %Ending frame
33
34     rect = rectxy; % The channel boundaries
35     H = rect(4); % Height of the channel in pixels
36
37     WRITE = 1; %Boolean to write extracted position and ...
        orientation data as .dat file
38
39     clear cent cent2 theta dir xsw ysw
40     xsw = 0; % Space allocation for x-, y- (or z-) position and ...
        orientation data
41     posy = 0;
42
43     j = 0; % Loop counter
44     [width, height, rgb, nof]=size(frames); %Obtain frame ...
        information
45
46     for k=k1:k2 %Processing loop for one video
47         j=j+1; %Increase counter
48         a = frames(:,:,k); %Take the next frame
49         a = imcrop(a,rect); % Crop the image down to channel ...
            boundaries
50
51         b1 = rgb2gray(a); % Obtain grayscale image
52         c2=edge(b1,'canny',orlimitxy); %Run edge detection.
53         se90 = strel('line',3,90);
54         se0 = strel('line',3,0); %Morphological structuring ...
            elements perpendicular to each other
55         c2 = imdilate(c2,[se90 se0]); %Apply dilatation
56         c2=imfill(c2,'holes'); %Fill the holes in the extracted ...
            edges
57         c2=imclearborder(c2); %Clear the borders
58         c2=bwpropfilt(c2,'MinorAxisLength',[minorax_min ...
            minorax_max]);
59         c2=bwpropfilt(c2,'MajorAxisLength',[majorax_min ...
            majorax_max]); %Find the region(s) with properties ...
            close to the swimmer image
60         stats = [regionprops(c2); regionprops(not(c2))]; %Obtain ...
            properties of all extracted regions
61
62         for ii=1:length(stats)
63             areas(ii)=stats(ii).Area; %Collect area information ...
                for each rectangle

```

```

64     end
65
66     [~,s_ind]=min(abs(areas-refarea)); %Find the rectangle ...
        with the area closest to that of the swimmer
67     cent(:) = stats(s_ind).Centroid; %Obtain the centroid of ...
        that rectangle
68
69     xswp(j)=cent(:,1);yswp(j)=cent(:,2); %Extracted positions
70     xsw(j) = cent(:,1)*upl;
71     posy(j) = (cent(:,2)-(H+1)/2)*upl; % y- axis is along ...
        the center of the bounding box, define Cartesian ...
        coordinates accordingly
72
73     clear cent s_ind areas
74     end
75     tmp=[xsw; posy];
76     save(strcat([videoname '.dat']),'tmp','-ascii');
77 end

```